MONTE CARLO MODELING OF DIFFUSE REFLECTANCE AND RAMAN SPECTROSCOPY IN BIOMEDICAL DIAGNOSTICS

A Dissertation
Submitted to
the Temple University Graduate Board

In Partial Fulfillment
of the Requirements for the Degree
DOCTOR OF PHILOSOPHY
Bioengineering

---

by
Alexander P. Dumont
Diploma Date May 2020

Examining Committee Members:

Dr. Chetan Patil, Advisory Chair, Bioengineering
Dr. Nancy Pleshko, Bioengineering
Dr. Erkan Tuzel, Bioengineering
Dr. Qianqian Fang, External Member, Northeastern University
Dr. W. Geoffrey Wright, External Reader, Health & Rehabilitation Sciences

TABLE OF CONTENTS

LIST OF FIGURES

ABSTRACT

Computational modeling of light-matter interactions is a valuable approach for simulating photon paths in highly scattering media such as biological tissues. Monte Carlo (MC) models are considered to be the gold standard of implementation and can offer insights into light flux, absorption, and emission through tissues. Monte Carlo modeling is a computationally intensive approach, but this burden has been alleviated in recent years due to the parallelizable nature of the algorithm and the recent implementation of graphics processing unit (GPU) acceleration.

Despite impressive translational applications, the relatively recent emergence of GPU-based acceleration of MC models can still be utilized to address some pressing challenges in biomedical optics beyond DOT and PDT. The overarching goal of the current dissertation is to advance the applications and abilities of GPU accelerated MC models to include low-cost devices and model Raman scattering phenomena as they relate to clinical diagnoses. The massive increase in computational capacity afforded by GPU acceleration dramatically reduces the time necessary to model and optimize optical detection systems over a wide range of real-world scenarios. Specifically, the development of simplified optical devices to meet diagnostic challenges in low-resource settings is an emerging area of interest in which the use of MC modeling to better inform device design has not yet been widely reported. In this dissertation, GPU accelerated MC modeling is utilized to guide the development of a mobile phone-based approach for diagnosing neonatal jaundice. Increased computational capacity makes the incorporation of less common optical phenomena such as Raman scattering feasible in realistic time

frames. Previous Raman scattering MC models were simplistic by necessity. As a result, it was either challenging or impractical to adequately include model parameters relevant to guiding clinical translation. This dissertation develops a Raman scattering MC model and validates it in biological tissues. The high computational capacity of a GPU-accelerated model can be used to dramatically decrease the model's grid size and potentially provide an understanding of measured signals in Raman spectroscopy that span multiple orders of magnitude in spatial scale. In this dissertation, a GPU-accelerated Raman scattering MC model is used to inform clinical measurements of millimeter-scale bulk tissue specimens based on Raman microscopy images. The current study further develops the MC model as a tool for designing diffuse detection systems and expands the ability to use the MC model in Raman scattering in biological tissues.

CHAPTER 1

INTRODUCTION

Light-matter interactions form the basis of biophotonics, which has a broad field of applications, ranging from the ballistic trajectories of photons, which form such technologies as optical coherence tomography (OCT), and the diffuse regimes, which incorporates technologies such as diffuse reflectance spectroscopy (DRS), Raman spectroscopy and Fluorescence spectroscopy. Simple DRS techniques have been developed and are now commonplace, with applications being readily available at the doctor's office in the form of pulse oximetry, which launches light above 650 nm to get a non-invasive measurement of oxygen saturation, or on a FitBit™, where green and red LEDs are used to capture heart rate and intensity. However, these technologies barely scratch the surface of the potential for light-matter based technologies, which could in the future be woven into clothes to provide real-time accurate measurements of a particular feature in the body, or to query for a particular disease just using the flash and camera built on-top a portable tablet, providing real-time analysis of disease in a non-invasive and portable way.

While these light-based technologies are being devised and developed, there is a parallel need to have computational modeling of these light-matter interactions done in a fast and accurate way. Analytical models for the propagation of light in turbid media provides an incomplete or inadequate solution to this particular problem. However, numerical techniques have gained traction in the past 30 years, and have overtaken the

analytical counterparts as the gold-standard in simulating light propagation. One of these numerical techniques is Monte-Carlo (MC) based, which tracks a photon with random or pseudo-random number generators dictating parts of the trajectory at each photon step, which guide the overall trajectory of the photon. This computational method of using random numbers to solve a problem that is deterministic in nature, essentially "solves" the analytical portion of the radiative transport equation.

Although MC based algorithms have been extensively used in the world of biophotonics, there is an inherent need to accelerate the numerical process, as MC methods are quite slow in their sequential implementation. GPU acceleration in recent years has produced the exact acceleration pathway for photon propagation, as in most models, one photon's trajectory is not reliant on any other photon's trajectory. The advent of GPUs as an easily accessible platform with the introduction of easy-to-use programming platforms made using these platforms much more achievable. The development of techniques with this acceleration as a fore-thought can make for algorithms that are faster at producing results while maintaining accuracy.

In this dissertation, we focus on using such a platform, called Monte Carlo Extreme (MCX), to inspect various tissue types. In the first aim of this project, MCX is used to query the responsivity of 4 different devices, 3 of which are mobile-phone-based devices, to different amounts of chromophores, namely, bilirubin, melanin, and hemoglobin, at multiple spectral points in order to determine the effect that additional chromophores had on reflectance seen at the surface. The range of data was in the order of thousands of different data points, which could be produced in under 2 hours by using the acceleration offered by MCX. For Aim 2, an efficient manner of simulating Raman

scattering as well as background Fluorescence and noise is presented and validated on Raman-based phantoms. The introduction of this efficient way of simulating Raman scattering in the MCX environment allowed for the production of rich Raman spectra in under 30 minutes, complete with autofluorescence background, which compared very well with the experimental signal from the Raman phantoms. Lastly, we used the same algorithm developed in Aim 2 to explore the multi-scaled relationships between bulk Raman spectra captured with a fiber probe placed at the surface of a brain with infiltrative glioma cancer, based on cancer grade. The increased proliferation of glioma cancer, as well as its spectral shifts, were taken into account, and subtle variations in both net Raman signal and layered Raman signals are noted, indicating a shift in the signal that can be associated with an increase in cellular proliferation and the presence of necrotic tissue and higher vascularization in the higher grade cancers.

Finally, future works will be discussed, as well as the innovation and novelty of the current body of work in this dissertation. Following this, significant conclusions from this work are discussed.

CHAPTER 2

BACKGROUND

In this chapter, we introduce the relevant background scientific context of this doctoral dissertation. Section 1.1 introduces the light-matter interactions relevant for this dissertation, including diffuse and Raman settings. Sec. 1.2, 1.3 and 1.4 describes the structural and optical properties of skin and brain as it relates to this dissertation work, with a special interest in bilirubin and melanin for skin, and grey and white matter, cerebrospinal fluid, and high-grade tumors for the brain. Sec 1.5 provides a survey of varied modeling approaches for different light-matter interactions, including the diffuse and Raman settings, and techniques and modfications that have been performed over the years. In Sec. 1.6, we review the current approaches in optical imaging and spectroscopy in diffuse settings, including diffuse reflectance techniques, Raman scaterring and Fluorescence spectroscopy.

Light-Matter Interactions in biological tissues

The electromagnetic spectrum is broad in the spectral domain, covering gamma rays, which have a very short wavelength, to radio waves, which have long wavelengths. Figure 2-1. Shows wavelength ranges for the entire wavelength range, and each wavelength ranges' associated diagnostic technology.

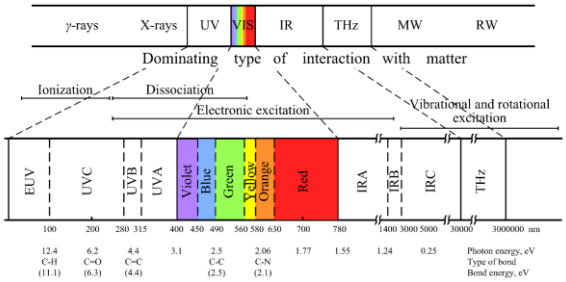

Figure 2-1. The electromagnetic spectrum of light

The spectral domain of light, and associated technology associated with each sub-range of light. Figure retrieved from Ref. [1].

In this dissertation, we are mostly interested in the visible range wavelengths from 400-700 nm and in the near-infrared region (NIR), which sits between the VIS and IR in Figure 2-11. In this spectral domain, there are several different effects that a photon may go through:

- Specular reflection
- Absorption
- Scattering
- Fluorescence
- Raman scattering

These are presented in detail in the following subsections, along with a mathematical description and physical relevance. Note that these effects are not an exhaustive list of all light-matter interactions.

Specular Reflection and Refraction

Specular reflection is an effect that happens at the interface of two media and is characterized as a mirror-like reflection of light rays. Each angle of light hitting the tissue does not enter the tissue, but rather reflects off the surface of the tissue as if it were a mirror. The vector direction of the light ray heading outwards from the medium is then a function of the initial angle that the ray has in the first medium, relative to the surface normal of the second tissue, reflected in an identical but opposing direction, known as the law of reflection. Alternatively, light can enter the tissue. However, because of the refractive mismatch between layers, the angle through the second layer is then a function of the initial ray's direction in the first layer and refractive index of the 2 layers, commonly known as Snell's law:

$$n_1 \sin(\theta_1) = n_2 \sin(\theta_2) \qquad (2\text{-}1)$$

Snell's law and the law of reflection are presented in Fig. 2-2

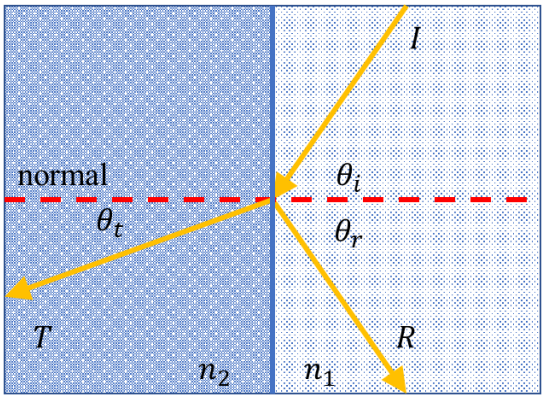

Figure 2-2. The law of reflection and Snell's law

Representation of the law of reflection (I→R) and Snell's law (I →T). The angle $\theta_r = \theta_i$ according to the law of reflection, and the angle $\theta_t = sin^{-1}\frac{n_1}{n_2}sin(\theta_1)$.

In most media, these two effects happen naturally. However, how much of the light is allowed to transmit into the second medium, and how much light is specularly reflected, depends on the refractive values for the two layers and the incident angle of light in the following way:

$$R_s = \left| \frac{n_1 \cos(\theta_i) - n_2 \cos(\theta_t)}{n_1 \cos(\theta_i) + n_2 \cos(\theta_t)} \right|^2 \quad (2\text{-}2)$$

Which is known as the Fresnel equation. R_s represents the amount of light that is specularly reflected, so that the light is then split into R_s reflected off the surface and 1-R_s allowed to transmit inside the second medium. So, for example, an air (n=1) to water (n=1.33) interface, with a light beam coming at 45°, would allow light to be transmitted into water at 32.12° relative to the normal with 5.23% of the beam having been specularly reflected and 94.77% of the beam allowed to be transmitted through by the above formulae.

As a caveat, it is worth noting that in most real-world situations, biological interfaces do not have a perfectly planar interface, which could affect the applicability of Snell's law and the law of reflection.

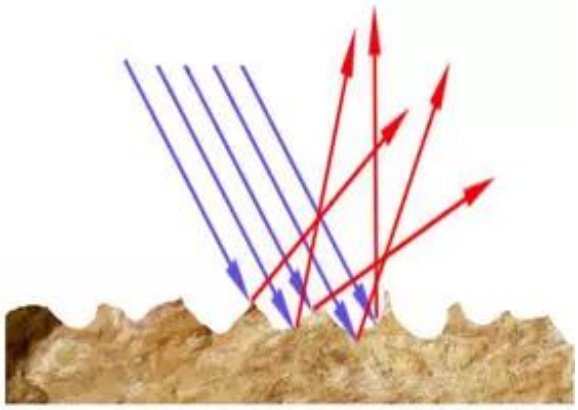

Figure 2-3. Differential scattering of light off an irregular interface

Representation of specular reflection of a biological sample having a non-planar interface with the air, and the reflection of light hitting the irregular surface. Figure retrieved from Ref [2].

The imperfections in most tissues are difficult to track individually; however, the averaged behavior for these biological tissues are well tracked at the macro-scale with Snell's law, the law of reflection and Fresnel's equation.

Absorption

The process of light absorption is the transformation of a light rays' energy into another form of energy, such as heat, as sound (as in the case of photoacosutic[3-6]), or as fluorescence as light traverses a tissue[7]. Groups or bundles of molecules have the ability to absorb some of the light traversing the medium, which is then typically transferred to heat in the molecules. The characterizing term for this absorption property is μ_a, commonly referred to as the absorption coefficient. This term physically represents the reciprocal of the distance d over which the light gets attenuated from an initial amount I_0 to $\frac{I_0}{e}$ [7]. This, in turn, fits into the exponential law for photon propagation in tissue as follows:

$$I(d) = I_0 \exp(-\mu_a d) \tag{2-3}$$

The coefficient μ_a is typically expressed in terms of cm^{-1} or mm^{-1}, which cancels out the d term (in distance units, such as mm) in the exponent, thus rendering the quantity inside the exponent unitless.

The physical process of absorbance is characterized by an effective cross-section in units of area. The area is a representation of the ability of the molecule to absorb light at a particular wavelength and does not necessarily describe the actual area of the molecule.

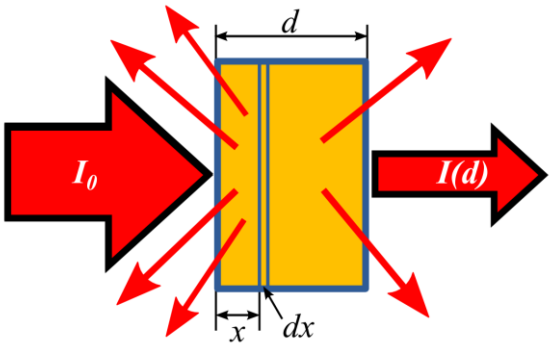

Figure 2-4. The process of absorption

The process of absorption in tissue due to both absorption and scattering. Figure retrieved from Ref. [8].

As such, each unit molecule has the ability to absorb according to a particular cross-section; the density of the molecules will also affect absorption. The last important parameter to consider is the number of incoming photons, denoted as N. Thus the formula that relates these three terms is:

$$\frac{dN}{dx} = -\rho_M \sigma_{abs} N \tag{2-4}$$

Where dx represents an arbitrary distance traveled in the medium. σ_{abs} represents the absorption cross-section of a homogenous mixture of molecules, and ρ_M equals the density of the molecules per unit volume. The $\rho_M \sigma_{abs}$ term combined is equal to μ_a.

Replacing the term dx on the right hand of the equation, and N on the left side, and substituting $\rho_M \sigma_{abs}$ with μ_a, equation 3 is recovered.

Another term commonly seen in diffuse spectroscopy is called the extinction coefficient ϵ, which is related to μ_a by the following formula:

$$\mu_a(\lambda) = \epsilon(\lambda)C \tag{2-5}$$

Where ϵ in typically in L/(mmol*cm) and C is the concentration of the absorbing agent, in mmol/L, so that the resultant multiplication is in units of 1/cm, which is the proper units for μ_a.

Elastic Scattering

Scattering is another of the light-matter interactions. In this sub-section, elastic scattering will be discussed, which means that light that has hit a molecule then scatters off the molecule at the same frequency. The next sub-header will discuss inelastic scattering, where the photon jumps to an excited vibrational state at a different wavelength than the incident photon.

Scattering occurs when a photon incident with a molecule changes its direction post-collision with the molecule. A photon may be under 1 of 2 regimes when this happens, which changes the scattering behavior. The two regimes are:

- Mie scattering, when the particle's size is within the same range as the wavelength of light hitting it
- Rayleigh scattering, in which case the size of the particle is much smaller than the incident photon wavelength

In the first case, we shall consider Mie scattering[9]. Mie scattering assumes that the shape of the molecule or particle is of a simple shape, be it either a sphere, ellipsoid, or cylinder. At the transport level, after the photon has collided with the particle, it changes its direction according to two direction angles, the first is a scattering angle, which is a measure of how much deflection from the incident photon has occurred after a collision with the molecule. The second angle is the azimuthal plane, which is orthogonal to the scattered direction of the photon and spans 2π. The deflection angle is graphically presented in Fig 5.

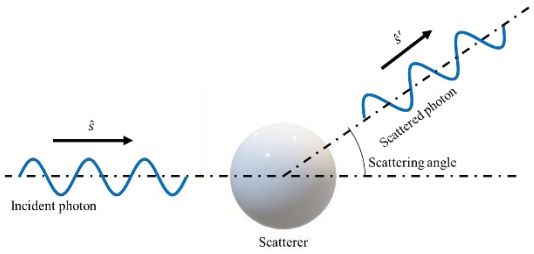

Figure 2-5. 2D representation of an elastic scattering event

An incident photon is set to collide with a scatterer with a unitary vector direction $\hat{s}$. After it collides with the scatterer, the photon has deflected by a scattering angle to a new direction vector $\hat{s}'$.

There are two unitary vectors in Fig. 2-5, $\hat{s}$ and $\hat{s}'$. These are the incident photons unitary direction vector and the scattered unitary vector. The angle θ represents the angle between the two vectors, and typically the angle ϕ represents the 2π azimuthal plane

angle. In order to get from the initial direction to the scattered direction, the scattering anisotropy factor is defined:

$$g = \langle \cos\theta \rangle = \int_0^{\pi} p(\theta) \cos(\theta)\, 2\pi \sin\theta \, d\theta \tag{2-6}$$

Equation 7 defines the anisotropy factor g, which is a description of the left-over forward scattering after a collision. G is bound from -1 to 1, with -1 being a complete reversal of direction after a collision $\hat{s}' = -\hat{s}$, and 1 is no effect on the direction after a collision, so that $\hat{s} = \hat{s}'$. The case that g=0 means that a particle is isotropic and falls into the Rayleigh regime. Henyey and Greenstein derived an analytical formula that can describe the angular dependence of light scattering by small particles[10], which they formulated into the Henyey-Greenstein function:

$$p\langle \cos\theta \rangle = \frac{1}{2} \frac{1 - g^2}{(1 + g^2 - 2g\cos\theta)^{\frac{3}{2}}} \tag{2-7}$$

Which dictates the probability of a particular scattering angle being chosen as a dependent on g. This formula is particularly useful in modeling photon transport, which will be discussed in a later heading.

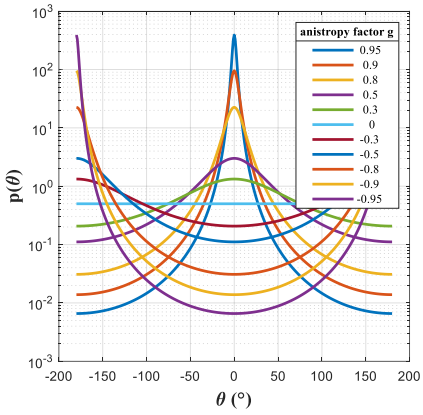

Figure 2-6. The Henyey-Greenstein function

The Henyey-Greenstein function shown over the entire range of scattering angles for varied g factors ranging from very forward scattering (g=0.95) to isotropic (g=0). Negative g factors are also shown, which are equal to the forward g offset by 180° phase.

Alongside the anisotropy factor g, which describes the tendency for deviation, there is also μ_s, which indicates the tendency of a particular medium to induce scattering on light hitting it. This is formalized with the component μ_s, which, just like with μ_a, is directly related to a scattering cross-section ρ_{sca} and the density of scatterers in the medium ρ_P in the following equation:

$$\frac{dN}{dx} = -\rho_P \sigma_{sca} N \tag{2-8}$$

Just as with the μ_a term, the composite $\rho_P \sigma_{sca}$ is equivalent to μ_s. A higher value of μ_s indicates a stronger tendency of the medium to induce scattering on incoming photons.

Rayleigh scattering occurs under the regime that a scattering particle is much smaller than the wavelength of light, so that $m\left(\frac{2\pi a}{\lambda}\right) \ll 1$. In this regime, the angular dependence of scattered intensity can be estimated by using the following formula:

$$I(r,\theta) = (2\pi)^4 \left(\frac{a^6}{\lambda^4 r^2}\right)\left(\frac{m^2-1}{m^2+2}\right) N \left(\frac{1+\cos^2\theta}{2}\right) I_0 \tag{2-9}$$

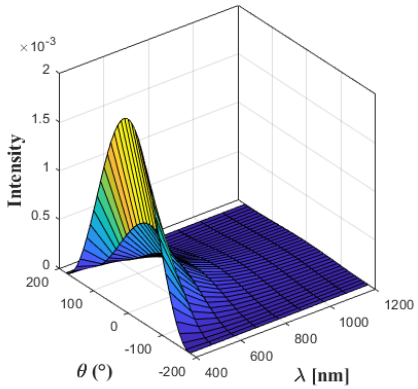

Figure 2-7. Graphical representation of Rayleigh scattering in terms of wavelength and degree offset

Light intensity as a function of angular dependence θ and of wavelength λ. The variables a, r and I_0 were all set to be 1, and the relative index of refraction m was set to be 1.1.

The scattering concepts introduced in this heading so far only relate to single scattering events. In biological tissue, more than one scattering event may occur in the tissue and the μ_s is typically much larger than the μ_a, so that several scattering events before an absorption event. In these cases, the variable μ_s' can be introduced, which incorporates both μ_s and g in one combined term:

$$\mu_s' = \mu_s(1 - g) \tag{2-10}$$

Known as the reduced scattering coefficient. The reduced scattering coefficient can help in describing the diffusion of photons through a random walk in tissue at the VIS-NIR regimes, where $\mu_s \gg \mu_a$. In this regime, the transport mean free pathlength (TMFP) as shown in Fig 8 can represent the equivalent of many mean free pathlengths (MFP).

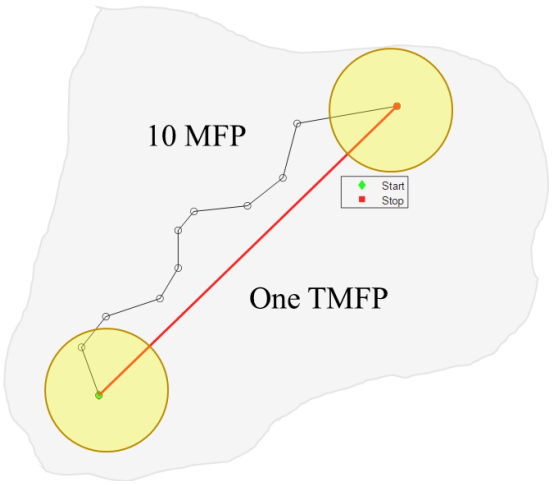

Figure 2-8. μ_s vs μ_s'

Representation of the trajectory of 10 scattering events under scattering regime, and one scatter event using the reduced scattering coefficient, which describes the same overall trajectory.

This approximation is useful as it simplifies the radiative transfer equation to the more straightforward to solve the diffusion equation, which is discussed in a later section.

Inelastic Scattering

Inelastic scattering occurs when there is a transfer of energy between incident photons and scattering molecules. In elastic scattering, there is no loss of energy after a collision event, so the outgoing photon is at the same frequency as the incoming photon. However, with inelastic scattering, there is an excitation of the scattered molecule to a virtual excited state, after which the molecule relaxes to a higher or lower vibrational state, known as Raman scattering. During this relaxation, a photon is emitted that represents the frequency between the excited virtual state and the vibrational state.

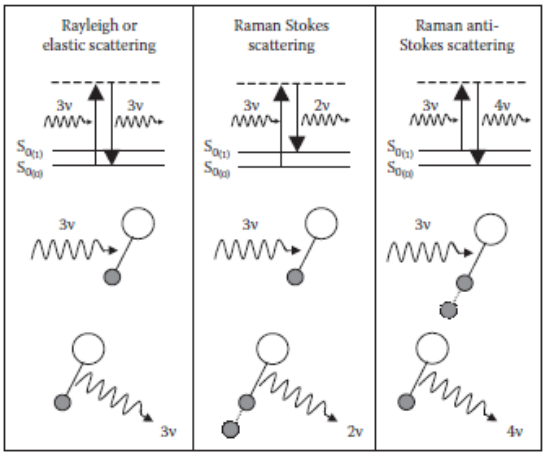

Figure 2-9. Different types of scattering

The different types of scattering phenomena are presented, with elastic scattering on the left, and different Raman scattering in the middle and right boxes. Figure retrieved from Ref. [11].

Figure 2-9 shows 3 different types of scattering, the first being an elastic process, and the second and third being inelastic. In the elastic scattering example, the net energy difference between the in and out-going photons is the same, so no energy is given to the system. The next two examples show the different ways that Raman scattering can happen in a molecule. The first example is of Raman stokes scattering, more commonly known as spontaneous Raman scattering. In this case, the frequency of the outgoing photon is lower than the incident photon. Spontaneous Raman scattering is a weak effect, occurring only once in a million times [12, 13]. In the case of an anti-Stokes shifted Raman scattered photon, the energy of the outgoing photon is actually higher than the incoming incident photon, as the energy of the molecule is transferred to the outgoing photon.

Raman spectra are usually presented in terms of the energy difference between the in and outgoing photons energy difference in frequency, in cm^{-1}, known as relative wavenumber ($\Delta\tilde{\nu}(cm^{-1}) = \left(\frac{1}{\lambda_{exc}} - \frac{1}{\lambda_{em}}\right) x \left(\frac{10^7\ nm}{cm}\right)$) or Raman shift. This is a convenient way to report Raman spectra, as the vibrational peaks for a particular chemical bond are always at the same locations in this regime, regardless of the incident frequency of photons.

A Raman spectrum shows the amount of vibration of a particular chemical bond in terms of relative wavenumbers; these peaks are directly informative of the amount of a particular structure present in a biochemical tissue.

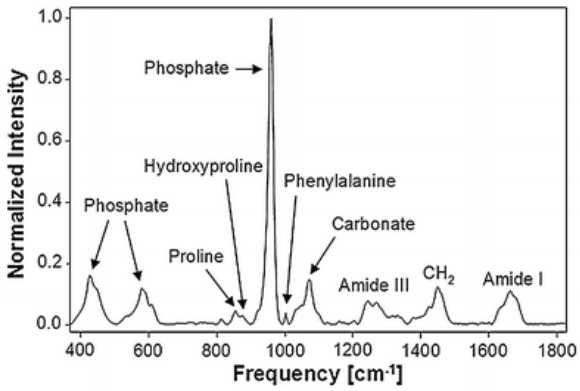

Figure 2-10. Raman spectrum of bone

The Raman spectrum of bone taken from the tibia of a 6-week old mouse bone. Each peak in the spectrum is representative of a particular chemical structure present in the sample. The spectrum was acquired using a 785 nm excitation laser and was baseline-corrected. Figure retrieved from Ref. [14].

Fluorescence

Fluorescence is an absorption process that can take place in a molecule through either endogenic (autofluorescence) or exogenic processes. Fluorescence occurs when a

molecule in the ground state S_0 gets elevated to an excited state S_1 as a result of absorbing a photon. The new photon energy state is not at equilibrium, and so the photon relaxes back to the ground state through a series of non-radiative transitions and fluorescence, in which a photon is released [15-17].

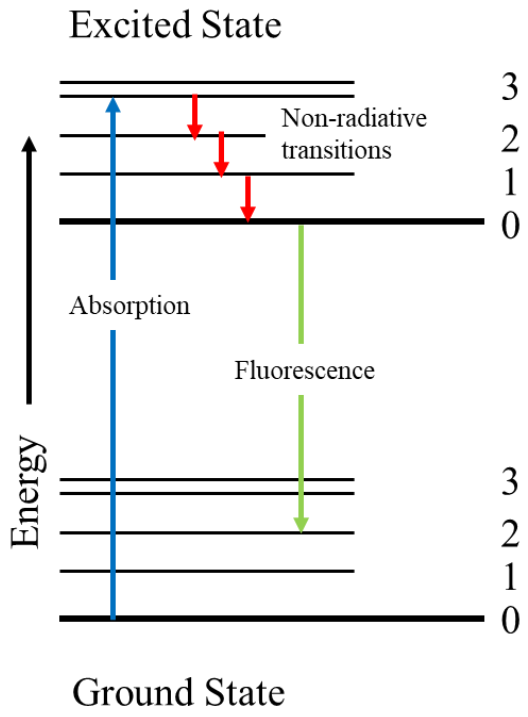

Figure 2-11. Jablonski diagram showing the different energy level transitions that lead to Fluorescence

This is a different effect than inelastic scattering, in which a molecule is raised to a virtual vibrational state which it directly exits. In fluorescence, the molecule is raised to an allowed (by Hamiltonian mechanics) excited state, where it spends some time relaxing to the ground state via radiative and non-radiative processes. The amount of time that it

takes for the molecule to relax from its excited state is known as τ, which is formally the amount of time it takes for the molecule to relax to $1/e$ of its excited state after initial absorption. Alongside this parameter, there is also the quantum efficiency ϕ_f which represents the number of fluorescent photons released per the number of photons absorbed.

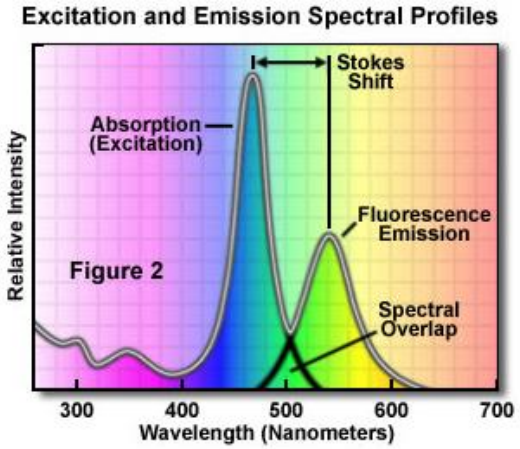

Figure 2-12. A typical fluorochrome with absorption and emission spectra

The absorption curve is left of the emission curve, indicating higher energy light, which can be absorbed differently based on which wavelength of light is used, thus affecting the quantum yield. Retrieved from Ref. [18].

Skin

The skin is the most superficial part of the body, acting as a soft outer tissue covering, with three primary functions [19, 20]:

1. Protection from external aggressors, such as radiation and chemicals, mechanical impacts, pressure and temperature variations, and micro-organism invasion.
2. Regulation, as with body temperature feedback that leads to sweating.

3. Sensation through the plethora of nerve cells that detect and relay changes in the external environment to the brain.

In the following sections, we will focus on presenting the optical and structural variations based on the different layers of skin. Each layer of skin has different optical properties, dependent on chromophore concentrations. Each chromophore will be listed by layer, as well as subsequent impacts on the skin's overall optical properties.

Structure

Skin is the largest organ of the human body by weight, with an average weight of 15% of a human's overall weight[21]. Skin provides an effective barrier between the body's internal structures and organs and external pathogens and assaults. A graphical representation of human skin is presented in Figure 2-14. The skin is separable into the epidermis, dermis, hypodermis, and subcutaneous layers (i.e. bone or muscles).

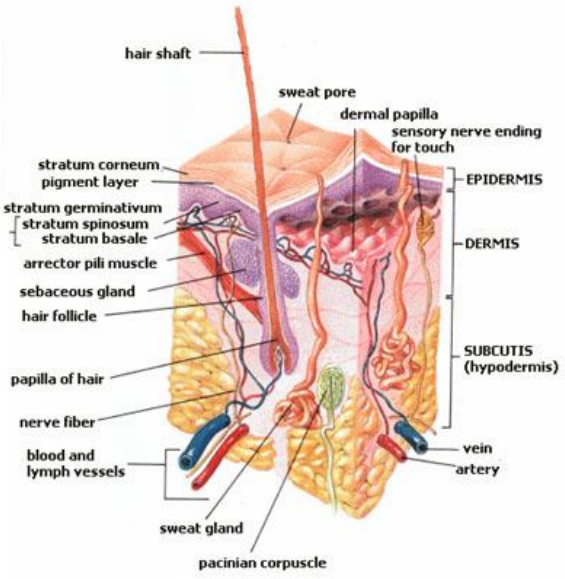

Figure 2-13. The different layers of skin

The different layers of the skin and the associated structural components associated with each layer. Retrieved from Ref. [22].

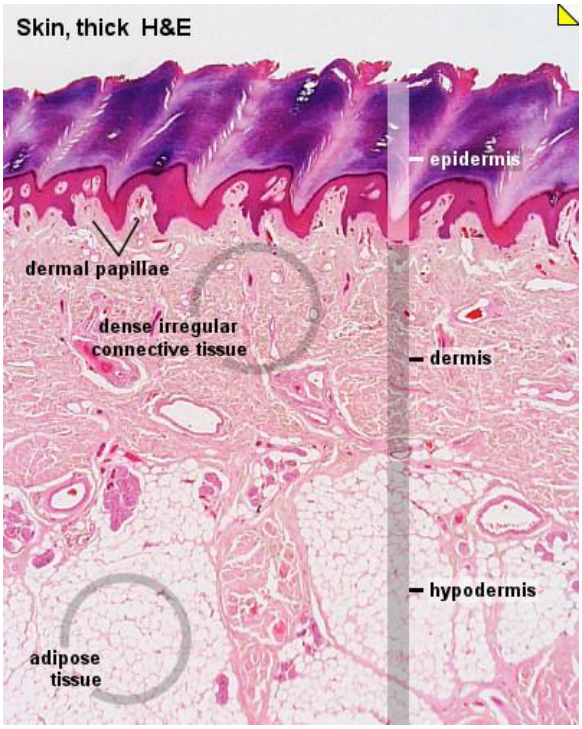

Figure 2-14. The first three layers of skin under Haemotoxylin and Eosin (H&E) staining

The first three layers of skin under Haemotoxylin and Eosin (H&E) staining, showing the layers with variable intensities based on cell nuclei (blue) and extracellular matrix (ECM) and cytoplasm presence (pink). Retrieved from Ref. [23].

Epidermis

The epidermis is the outermost layer of the skin, and provides the first line of defense against environmental pathogens[24] and regulates the amount of water lost by the body[24, 25]. The epidermis is a continually renewing epithelium, subdivided into the

basal layer, the spinous layer, the granular layer, and the stratum corneum, which acts as the first line barrier with the external environment. The primary cell produced in the epidermis is keratinocytes, which further synthesize into anucleated squamous cells which form the stratum corneum layer[24]. In addition to keratinocytes, melanocytes are present in the basal layer. These melanocytes produce the pigment granule melanosome, which contains melanin. Melanocyte pigment protects the skin from ultraviolet (UV) radiation and also gives the skin its color. The epidermis thickness in adults can vary based on sex, age and race, however, the average epidermis thickness is about 0.1 mm, which is about the thickness of a sheet of paper[26].

In neonates, the thickness of the epidermis layer is less than in adults, and the amount of melanin produced is less as well[27, 28] as the infant is in a state of active development. During this time, neonates microrelief structures are denser, the stratum corneum is thinner and the dermal and granular cells are smaller. These differences between adult and neonatal epidermis are important to consider when making a model of neonatal skin, which is presented in Chapter 3.

Dermis

The dermis is the second layer of skin, separated from the epidermis by the dermal-epidermal junction, otherwise called the cutaneous basement membrane zone (BMZ). The dermis varies largely in thickness, from 0.5-5 mm in adults, depending on body location. The thinnest dermis is found on the eyelid, whereas the thickest is on the back [21]. The dermis is split into two parts, the papillary dermis, which is in contact with the BMZ and is supplied with blood vessels and nerve endings, and the reticular dermis which is the main component of the dermis and is in contact with the hypodermis.

The dermis is primarily composed of collagen fibers, elastic tissue, and cellular components. Approximately 70% of the weight of the dermis is from collagen type I and III[29], and elastic fibers account for another 5% weight. A gelatinous substance called the ground substance, composed of proteoglycans and glycoproteins engulfs the collagen and elastic fibers in suspension and makes up most of the remaining weight [21]. The dermis is the most vascularized layer of the skin and is the main entry point to provide nourishment and waste removal for the dermis and epidermis layers.

Hypodermis

The hypodermis, also known as subcutaneous tissue, is the lowermost layer of the integumentary system (skin and its appendages) and is mostly composed of adipose tissues, connective tissues, and macrophage cells. The thickness of the hypodermis varies between different people, different disease types and different positions on the body [30]. The hypodermis has several vital functions[31]:

- Storing fat for later use
- Protection/cushioning of mechanical impacts
- Attaching the upper layers of skin to the underlying muscle
- Body temperature regulation by functioning as an insulator to external temperatures

Brain

The complex human body is governed by its most complex organ – the brain. Weighing at about three pounds, the brain plays the most important role of controlling the

entire bodily functions while translating information from the outside world by means of the five senses. It contains billions of neurons that remain in contact with each other, and by means of these neural units, the brain produces and controls every kind of action, thought, experience, feeling and memory in a human being.

These neurons form connections with each other in ranges of thousands or even tens of thousands through very small structures known as synapses. A synapse is basically a site for the transmission of an electric impulse between neurons. Almost a million new connections are built within the brain every second [32]. It is through these tiny structures and constantly changing neural connections that personalities are shaped and habits are learned.

Structure

- The central nervous system comprises of three major parts:
- **Cerebrum:** The cerebrum is the largest and the most anterior part of the brain, and is responsible for the coordination of voluntary actions and for the interpretation of complex sensory activities such as touch, vision, and hearing. It is divided into two hemispheres known as the right and left hemispheres of the brain. The right part of the cerebrum controls the left side of the body and vice versa. A bundle of neural fibers, known as the corpus callosum, connect these two parts and controls the communication between the right and left part of the cerebrum.
- **Cerebellum:** In humans, cerebellum plays a major role in motor control and is located below the cerebrum, smaller in size. In some animals, however, it may be

equal to the cerebrum in size, or even larger (such as in the mormyrid fish)[33]. It coordinates the movement of muscles and maintains balance and posture. The cerebellum is divided into three zones known as the vermis, the intermediate zone, and the lateral hemispheres. It can also be subdivided into three parts based on their functioning, namely cerebrocerebellum, spinocerebellum, and vestibulocerebellum. All these zones help with the proper movement of the body, such as allowing for error connection, and helping with visual guidance during movement.

- **Brainstem**: It is located in the posterior of the brain and is continuous with the spinal cord. The involuntary actions such as breathing, digestion, sneezing, vomiting, swallowing, and sleep cycles come under the domain of the brainstem. It also connects the spinal cord to the cerebrum and the cerebellum. It is divided into three parts; the midbrain, the pons and medulla oblongata. The brainstem is very small in size and only constitutes around 2.6% of the brain's total weight [34].

Neurons are found in different forms in the brain. Although they can be divided into thousands of different types, from the point of view of their functionality, they can be divided into three broad types.

- **Sensory Neurons**: These neurons are related to senses, such as making sure the tongue can taste, the nose can smell, ears can hear, eyes can see, organs can touch or feel external objects which the brain can use to form an overall sense of the surroundings.

- **Motor Neurons**: These neurons facilitate both voluntary and involuntary body movements. They are responsible to form a quick contact between brain and spinal cord and body parts, both internal and external, and glands spread within the body. A further division of these neurons occur and named as lower neurons and upper neurons. The first type carries signals from body parts to spinal cord while the second type connects brain with spinal cord.
- **Interneurons**: This is the most common type of neurons that mostly transmits signals between both sensory and motor neurons. Some of interneurons are related to sense of pain and also capable of sending messages directly to the brain center.
- These are also named as associative neurons.

From the point of view of shape, neurons can be divided into these types.

- **Multipolar neurons**: This is the most common type of neurons which contains a cell body, a single but long axon and a group of short dendrites. Its axon has two branches which enable it to connect with dendrites to receive messages and send it to the spinal cord.
- **Bipolar neurons**: This type of neurons is mostly found in the retina of eyes, top of nasal cavity and inside of an ear. It also forms a chain of messages through cell body to spinal cord and brain.
- **Pseudo-unipolar neurons**: These are mostly similar to bipolar neurons and come into action in the situation of pressure, touch and pain. They are devoid of dendrites and signals are sent through axons.

- **Glia**: These are also called glial cells and work as additional but integral support for nervous system. Without the presence of Glia, neurons cannot function properly. These cells provide guide neurons towards their destinations and protect them from ions and other chemicals which may cause damage to neurons.

Cerebrospinal fluid

Cerebral spinal fluid (CSF) is a colorless liquid that surrounds the brain and spinal cord. It is created by cells called choroid plexus which are formed by bunches of capillaries. 140 to 270 ml volume of CSF is found in an average person's body. Its main functions include extracting nutrients from blood, providing protection to the brain and getting rid of brain cells' waste. It is created in and circulates through the ventricular system, which consists of four cavities present within the brain, then enters the subarachnoid space to exit via the arachnoid villi into the venous system.

White Matter

This is also part of the central nervous system and it acts as a vessel for glial cells responsible for the production of myelin and the astrocytes. It ensures that signals are transmitted fast. White matter also influences motor and sensory functions. It generates a proper response to outside stimuli. Its place is subcortical, the deeper tissues of the human brain. One of its functions is the protection of nerves from external harm.

Grey Matter

This is part of the central nervous system and composed of neural cell bodies also called soma. Its function is to control activities related to senses and muscles. It is found in the cerebrum, the cerebellum, and truncus encephali. Grey matter is made up of axon terminals, dendrites and all nerve synapses which form connections between neurons. It contains a lot of cell bodies and a few axons. Axons are responsible for transmitting information away from the cell body to neurons, muscles and glands. Dendrites act in the opposite direction and bring information to the cell body. Synapse is a small gap between neurons and it provides a mechanism for all the two-way transmission.

High-Grade Tumors

A brain tumor occurs when abnormal cells in the brain form, either as a primary tumor (one that started in the brain) or a secondary tumor (metastasized from another section of the body). The cause of most brain tumors is still unknown to this day [35] and survival rates are predominantly based on maximized removal of the bulk tumor, with chemotherapy and radiotherapy treatments having mixed effects. Even with the maximal removal of the tumor, the post-surgery survival rate is relatively weak, with the median survival rate being 14 months [36].

Glioblastoma Multiforme (GBM) is the most aggressive primary cancer of the brain (rated as a Grade IV). In this category, there are four types of sub-types; classical, proneural, mesenchymal and neural. These subtypes have been identified as having different levels of normal epidermal growth factor receptor (EGFR) and mutated EGFRvIII, mutated p53/TP53 genes responsible for cell death, IDH1 gene which that encode isocitrate dehydrogenase-1 and NF1 gene which encodes for neurofibromin.

These are the most well-known genetic mechanisms for GBM; however, there are 1000's of different genes and genetic pathways that have yet to be revealed.

Optical Properties of Skin and Brain

The optical properties of skin, namely, μ_s, μ_a, g and n will be discussed for individual chromophores present in the varied layers of the skin in this section. Additionally, we will go over some previous studies in brain optical properties, which are relevant for Chapter 5.

Absorption Properties

The skin plays host to a variety of chromophores. The most important chromophores in the skin vary based on the skin layer and will be discussed with the outermost layer, the epidermis, coming first, and the hypodermis last. In the epidermis layer, the strongest absorbing chromophore is melanin. Melanin is assumed to be distributed evenly and is varied in its fractional volume from 1-3% for light-skinned Caucasians an 18-43% for darkly pigmented Africans. Previous studies on melanin's optical properties [37-40] point to the fact that melanin in the UV-VIS range is monotonically decreasing as wavelength increases. A visual of melanin is presented in Figure 2-15 over the variable physiological range of 0.01 to 0.1 fractional volume. In neonates, melanosome molecules are smaller than their adult counterparts, as well as less densely packed, which reduced the overall optical absorption from melanin.

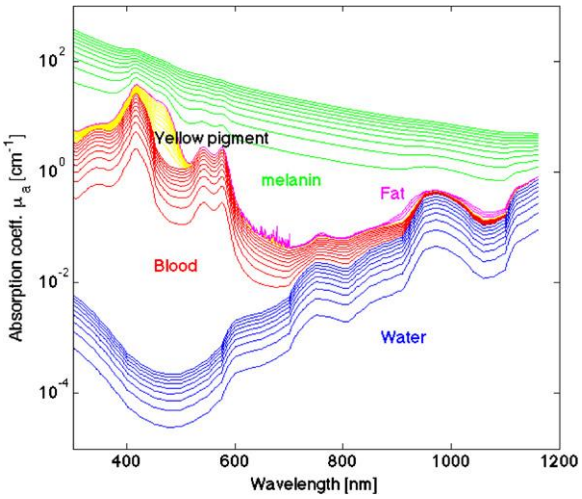

Figure 2-15. Total absorption coefficient μ_a for varied relative concentrations of 5 different absorbing chromophores. Figure retrieved from Ref. [41].

Next comes the dermis layer. In this layer, there are two primary absorbers. The first is bilirubin, and the second is hemoglobin, either oxygenated or deoxygenated. Bilirubin is a yellowish compound that is the result of catabolic pathways that breaks down heme. It is this molecule that causes jaundice in adults and neonates, and indicates a failure of the body's ability to breakdown the molecule and secrete it through the bile and urine [42]. This effect is more pronounced in neonatal infants, as there is a switch from the mother's hemoglobin to the baby's own hemoglobin production, which causes more heme lysis, conjugated with the liver's immature metabolic pathways which cannot process the waste[43-47]. Because of this, 60-80% of all neonates are born with some form of hyperbilirubinemia, which declines by 10-14 days after birth [45]. However, it is important to screen for bilirubin in neonates, as an excessive amount of bilirubin can cause irreversible harm to the neonate, such as sensorineural deafness, enteropathy and kernicterus. The optical absorption of bilirubin are shown in Figure 2-15 over a range of

physiological values (1-20 mg/dl). Hemoglobin is the second strong absorber in the dermis layer. Hemoglobin can either be oxygenated or deoxygenated as it delivers oxygen to the body from the lungs, which varies its optical absorbance factors. The molar extinction coefficients are shown in Figure 2-16.

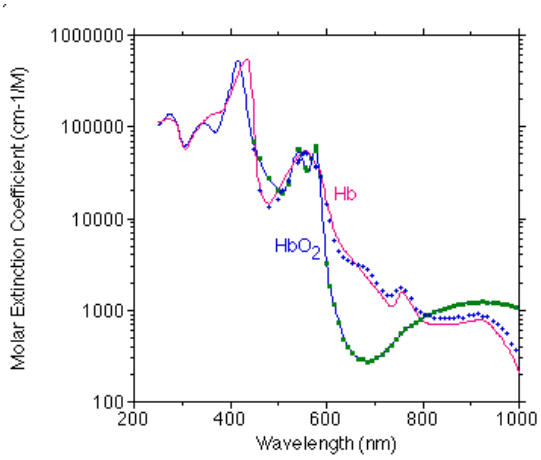

Figure 2-16. Molar extinction coefficients for oxy- and deoxygenated hemoglobin

Changes in optical absorbance features occur as the oxygenated version of hemoglobin carries up to 4 oxygen molecules. Retrieved from Ref. [48].

In the hypodermis, the major chromophore of interest is the adipose tissues, which aggregate into subcutaneous fat. The optical absorption is presented graphically in Figure 2-17. Several groups have explored the optical properties of fat emulsions [49, 50] and the hypodermis[38, 51].

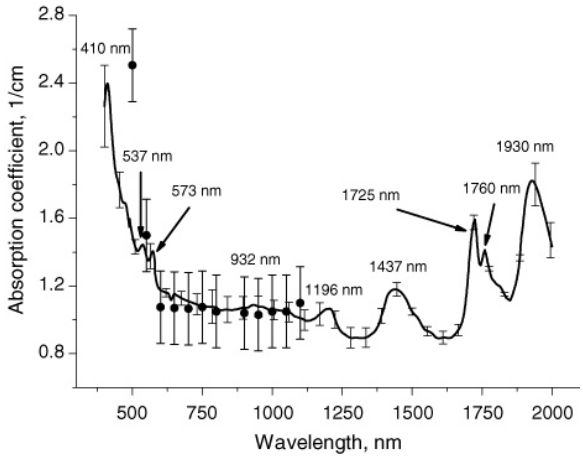

Figure 2-17. Optical absorbance coefficients for human subcutaneous adipose tissue. Retrieved from [51].

Biological tissues are difficult to quantify, as changes occur between different persons, different tissues and even different times. The major absorbing factors in the UV-VIS-NIR regimes are:

1. S Oxygen saturation
2. B Average blood volume fraction
3. W water content
4. Bi bilirubin concentration
5. βC β −Carotene concentration
6. F Fat content
7. M Melanosome volume fraction

As proposed by Jacques et. al [41], these 7 absorbing quantities can be summed together in the following equation to construct any arbitrary biological tissue:

$$\mu_{a,T} = BS\mu_{a,oxy} + B(1-S)\mu_{a,deoxy} + W\mu_{a,water} + F\mu_{a,fat} \quad (2\text{-}11)$$
$$+ M\mu_{a,melanosomes} + 2.3C_{bili}\epsilon_{bili} + 2.3C_{\beta C}\epsilon_{\beta C}$$

In eq. 2-11, the oxygen saturation, the water content, the fat content, the oxygen saturation, and the melanosome content are in fractional volume measures (i.e., 0.95 for oxygen saturation represents 95% oxygen saturation).

Anistotropy Factor

The anisotropy factor is an associated term in the reduced scattering coefficient. As seen in Fig 1-18, the anisotropy factors for skin and brain tissue are highly forward scattering, as are most biological tissues having wavelengths in the visible light regime [52, 53].

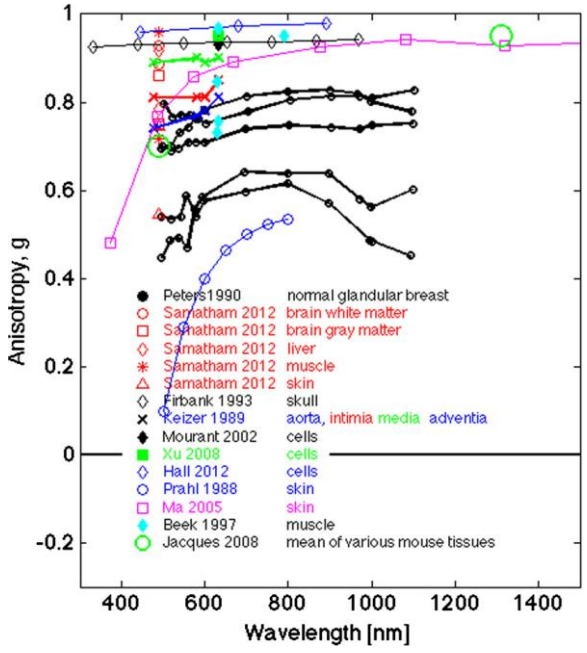

Figure 2-18. Anisotropy factor for some biological tissues with varying wavelengths. Retrieved from [41].

Scattering Properties

The main source of scattering in biological tissues like skin is due to filamentous proteins; keratin is the major source of scatter in the epidermis, and collagen is the principal scattering constituent in the dermis[54]. Additional scattering is due to melanosomes in the epidermis, cell nuclei, cell walls, and smaller structures of the skin [55]. The Mie scattering solutions for these filamentous proteins have been approximated by [56, 57]. Jacques et al. [41] proposed the following equation to combine both Mie and Rayleigh scattering to determine the reduced scattering coefficient μ_s':

$$\mu_s' = a' \left(f_{Ray} \left(\frac{\lambda}{\lambda_0} \right)^{-4} + (1 - f_{Ray}) \left(\frac{\lambda}{\lambda_0} \right)^{-b_{Mie}} \right) \tag{2-12}$$

Where λ is the wavelength being queried and λ_0 is a reference wavelength, chosen as 500 nm by Jacques, in order to yield a dimensionless value inside the parenthesis. f_{Ray} is the fraction of Rayleigh scattering and 1-f_{Ray} is the fraction of Mie scattering. a' represents the μ_s' term at λ_0, b_{Mie} is the exponent factor for the Mie scattering. The Rayleigh term is:

$$\mu_s' = a' \left(f_{Ray} \left(\frac{\lambda}{\lambda_0} \right)^{-4} \right) \tag{2-13}$$

And the Mie term is:

$$\mu_s' = a' \left((1 - f_{Ray}) \left(\frac{\lambda}{\lambda_0} \right)^{-b_{Mie}} \right) \tag{2-14}$$

Which are then summed up to make eq 15, which produces a more complete μ_s'. The factor f_{Ray}, b_{Mie}, and a' varies between tissue types. Figure 19 provides the reduced scattering coefficient for skin and brain tissue, which are both relevant to this dissertation.

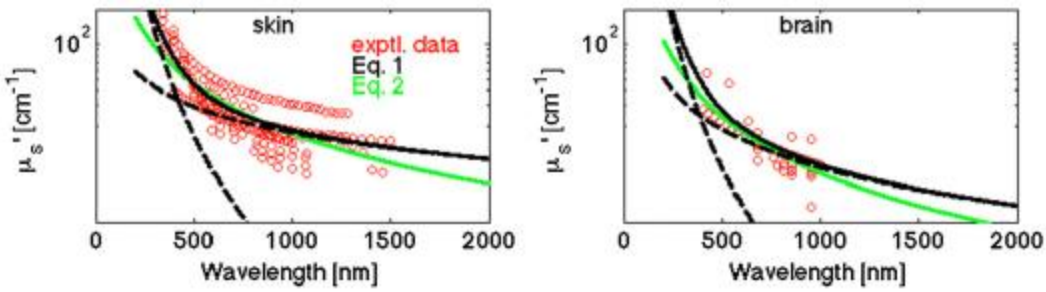

Figure 2-19. Reduced scattering coefficient μ_s' for skin and bain.

Dots represents previous studies. The green lines are fitted with eq [Mie], the black solid lines are the fit after applying eq [μ_s']. Retrieved from Ref[41].

The optical properties of varied tissue layers for the brain are also reviewed in [41], who comments on different groups who have approximated the optical properties over varied wavelengths and in in-vitro and in-vivo situations. Some of the retrieved reviewed groups are described in the next few sentences. Beck et al. [58] used wavelengths from 420-450, 532 and 635 nm with a fiber optics probe to recover the optical absorbing and reduced scattering coefficients of the brain, which were further used in a diagnostic modality. Bevilacqua's group used a fiber optics probe at 4 discrete wavelengths (674, 811, 849 and 956 nm) to probe the *in-vivo* human white matter, scar tissue, optic nerve, and tumor optical properties. Zhao et al. [59] used frequency domain NIR spectroscopy to determine the optical properties of neonates at 2 NIR wavelengths (788 and 832 nm), commenting on the reduced absorption coefficient neonates compared to adults. Additionally, there is a study by Yaroslavsky[60] that explores the induvial optical properties of the brain by layer, using an integrating sphere setup, which returned

μ_a, μ_s and g for white and grey matter, cerebellum, pons, thalamus, and 2 different brain tumors over the range of 400-1100 nm.

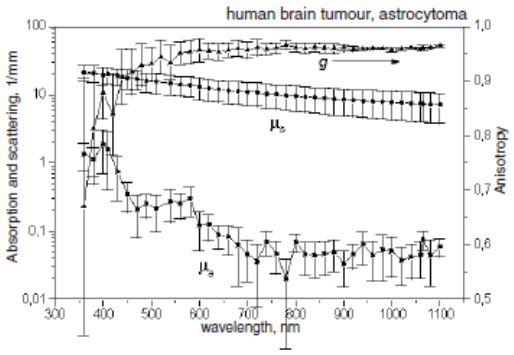

Figure 2-20. The absorbing and scattering coefficients, along with the anisotropy factor g for an astrocytoma tumor measured in-vitro. Retrieved from [60].

Full reviews of optical properties of biological tissues, measured in-vivo or in-vitro are provided in Ref. [41, 61, 62].

Refractive Index

The real refractive index n describes how much slower the speed of light v in a particular tissue is relative to the speed of light n a vacuum (c_{vac}). Formally defined as $n = \frac{c_{vac}}{v}$, the refractive index can be estimated for most biological tissues by using the water content to dry mass ratio of the sample. The formula for this effect is:

$$n = n_{dry} - \left(n_{dry} - n_{water}\right)W \tag{2-15}$$

With W being water content, expressed in fractional volume, n_{dry} being the refractive index of a dry mass of the tissue and n_{water} being the refractive index of water. Using this formulaism, with an appropriate value of n_{dry} set to 1.514, it is possible to

get the refractive index of most biological tissues [41]. Figure 21 shows the refractive index of some biological tissues captured experimentally with an Abbe's refractometer (red dots), compared to the estimation of n using the above formula.

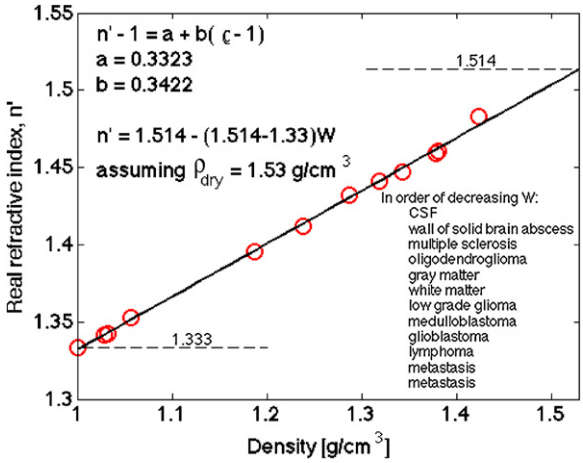

Figure 2-21. The refractive index of some biological tissues, including CSF, white and grey matter. Retrieved from [41].

The refractive index becomes important in modeling photon propagation, as the speed of travel through a medium is dependent on n. Additionally, if there are refractive mismatches between different layers, which is common in biological tissue, then the refractive mismatch makes the photon be either transmitted to the second layer according to Snell's Law or reflected according to the law of reflection.

Modeling of the propagation of light in tissue

Modeling has been important in biophotonics for a variety of reasons, which are highlighted in the following list:

- Fundamental understanding

- Design and fabrication of hardware
- Data Collection
- Data analysis

Varied groups have tried to use both analytical and numerical platforms over the years and use these platforms to explain one or more of the points indicated in this list. The radiative transfer equation, and the subsequent diffuse equation are examples of analytical platforms for solving for photon propagation, and these methodologies have their positive and negative attributes, which will be discussed in the following subheadings. On the other side of things, numerical techniques can do a better job of tracking light-propagation in many different situations, but these also have their own merits and demerits, which will be discussed later in this heading, as well as early and current methods aimed at increasing the utility of these numerical techniques.

Photon transport in biological media can theoretically be tracked and modeled in a closed-form, analytical way using the radiative transfer equation (RTE). However, RTE is oftentimes difficult to solve in real-world situations with varied and arbitrary layer dimensions and launch functions. We will briefly discuss the principles of RTE and how the equations of radiative transfer are best suited to model light transport, and why this equation is difficult to solve (usually solved by numerical solvers). The derivations presented are largely based on Wang[63] and of Chandrasekhar[64].

Spectral radiance, represented with the symbol $\boldsymbol{L_v}$**,** is defined as the energy flux per unit of normal area per unit of solid angle per unit of time per unit of temporofrequency. The normal area is orthogonal to the flux direction. The radiance $\boldsymbol{L}$ is defined as the spectral radiance integrated over a small frequency range $[\upsilon, \upsilon + \Delta\upsilon]$, and

is a representation of spectral radiance at a particular frequency range, and thus has units equivalent to spectral radiance without the temporofrequency. The equation for radiance is:

$$L(\vec{r}, \hat{s}, t) = L_v(\vec{r}, \hat{s}, t)\Delta v \tag{2-16}$$

The variable $\vec{r}$ is the position, $\hat{s}$ is the unit direction vector and t denotes an element of time. The amount of radiant energy dE that flows through the differential area dA within the differential solid angle dΩ during a differential time dt can then be defined with the following formula:

$$dE = L(\vec{r}, \hat{s}, t)(\hat{s} \cdot \hat{n})dAd\Omega dt \tag{2-17}$$

Where $\hat{n}$ is representative of the outward normal vector unit of dA and $\hat{s} \cdot \hat{n}$ is a representation of the dot product of the unit direction vector $\hat{s}$ and the unit normal vector of the area $\hat{n}$. The dot product then gives the cos of the angle between the 2 unit vectors, which means that the above formula can be represented as:

$$dE = L(\vec{r}, \hat{s}, t)\cos\theta\, dAd\Omega dt \tag{2-18}$$

Radiance is the dependent quantity in the equation of radiative transfer, and can further define other types of outputs, such as fluence rate. Fluence rate, defined as Φ is defined as the energy flow per unit area per time regardless of the flow direction, meaning it is integrated over the 4π solid angle. Fluence rate relates to radiance as follows:

$$\Phi(\vec{r}, t) = \int_{4\pi} L(\vec{r}, \hat{s}, t)d\Omega \tag{2-19}$$

This equation can further be simplified to spherical coordinates, which is done in [63]. The differential time unit is not included in fluence rate, and so this is a

representation of the overall radiance over all steradian angles over a range of time, with no discrimination in time. However, fluence, which is the time-integrated fluence rate, is the addition over all times of fluence rate, which takes the analytical form:

$$F(\vec{r}) = \int_{-\infty}^{\infty} \Phi(\vec{r}, t)dt \tag{2-20}$$

The final relevant physical quantity is defined as current density or energy flux, denoted with J. The current density is the net energy flow per unit area per unit time and is the result of the multiplication of radiance by the $\hat{s}$ vector.

With an idea of what the outputted dependent terms of the RTE are, the derivation based on various factors can then be derived. The subsequent derivation is based on derivations in [64].

In the first place is the consequence that a beam is not pencil-like in shape and orthogonal to the surface of the medium, so that it may be of a Gaussian shape or an even more complicated shape, such as with spatial frequency domain imaging (SFDI), entering the medium at 45° relative to the surface. In this case, the light beam is said to be either convergent or divergent. The description of energy divergence is thus:

$$dP_{div} = \frac{\partial L(\vec{r}, \hat{s}, t)}{\partial s} dsdAd\Omega \tag{2-21}$$

In this case, dP is the energy exiting the volume element, where the volume is equal to $dV = dAds$ so that the above formula can be expressed as:

$$dP_{div} = \frac{\partial L(\vec{r}, \hat{s}, t)}{\partial s} dVd\Omega \tag{2-22}$$

The sign convention is that a negative value for dP means the beam is converging in the volume and positive means the beam is diverging. Next is the effect of the

attenuation coefficient, the addition of μ_a and μ_s, on energy losses in the volume over all angles. The attenuation coefficient means that a light beam can exit the volume both as a consequence of either being absorbed by a molecule or being scattered away from the volume. The formula for energy if loss due to these effects is given as:

$$dP_{ext} = (\mu_t ds)[L(\vec{r}, \hat{s}, t) dA d\Omega] \tag{2-23}$$

Then there is the effect of scattering on the energy loss in the volume. Given that a medium has μ_s, then the energy scattered from the medium's volume is:

$$dP_{scat} = (\mu_s dV)\left[\int_{4\pi} L(\vec{r}, \hat{s}, t) P(\hat{s}', \hat{s}) d\Omega'\right] d\Omega \tag{2-24}$$

The introduction of a phase function $P(\hat{s}', \hat{s})$ takes into account the probability as a measure of steradian angle, and this function must be normalized to unity so that it fits into the equation above.

$$\int_{4\pi} P(\hat{s}', \hat{s})\, d\Omega = 1 \tag{2-25}$$

The variable $\hat{s}'$ represents the direction vector of the propagation light, and the unit vector $\hat{s}$ represents the direction vector of the beam after having been scattered. The angle difference between the incoming and outgoing scattered light is then functionally dependent on the scattering anisotropy factor g in the following way:

$$g = \int_{4\pi} P(\hat{s}', \hat{s})(\hat{s}', \hat{s}) d\Omega \tag{2-26}$$

Using the above formula, $P(\hat{s}', \hat{s})$ can be solved for and inputted into the formula for energy losses due to scattering, with L and μ_s being given.

The last concept that can cause energy differences in the model is called the source function. This function is a measure of the emissivity of a particular volume and is formally defined as:

$$S = \frac{j}{\mu_a} \tag{2-27}$$

Where j is the emission coefficient. The energy contribution to the volume due to a source is thus:

$$dP_{src} = S(\vec{r}, \hat{s}, t) dV d\Omega \tag{2-28}$$

Finally, the preceding elements must be combined in a formula, known as the radiative transport equation (RTE). The energy change in the volume must be equal to the aggregation of all known effects in the volume, which is a combination of extinction, scattering, divergence and source function in the volume. The total energy change is then:

$$dP = -dP_{div} - dP_{ext} + dP_{scat} + dP_{src} \tag{2-29}$$

Which is required by the conservation of energy principle. The above formula can be fit into the following equation:

$$dP = \frac{1}{c} \frac{\partial L(\vec{r}, \hat{s}, t)}{\partial t} dV d\Omega \tag{2-30}$$

By substituting terms in equation 17, with the equations for the energy variations due to divergence, emission, scattering and source, we get the general formula for radiative transport:

$$\frac{1}{c}\frac{\partial L(\vec{r},\hat{s},t)}{\partial t}dVd\Omega$$

$$= -\frac{\partial L(\vec{r},\hat{s},t)}{\partial s}dVd\Omega - (\mu_t ds)[L(\vec{r},\hat{s},t)dAd\Omega]$$

$$+ (\mu_s dV)\left[\int_{4\pi} L(\vec{r},\hat{s},t)P(\hat{s}',\hat{s})d\Omega'\right]d\Omega \quad (2\text{-}31)$$

$$+ S(\vec{r},\hat{s},t)dVd\Omega$$

This formula can be simplified by eliminating the $dVd\Omega$ which shows up in all terms, and by converting dP_{div} in divergence form.

$$\frac{1}{c}\frac{\partial L(\vec{r},\hat{s},t)}{\partial t} = -\hat{s}\cdot\nabla \mathrm{L}(\vec{r},\hat{s},t) - \mu_t \mathrm{L}(\vec{r},\hat{s},t)$$

$$+ \mu_s \int_{4\pi} \mathrm{L}(\vec{r},\hat{s}',t)P(\hat{s}',\hat{s})d\Omega' + S(\vec{r},\hat{s}',t) \quad (2\text{-}32)$$

Which is the RTE equation that describes light transportation through any medium with known optical properties.

Diffuse Theory

The RTE equation quickly becomes difficult to solve, largely due to multiple scattering events, which creates a redundant cycle of RTE's[65]. Dullemond describes the problem of scattering in a diffuse environment, where there are often multiple scattering events, as a "chicken-egg" cycle; each scattering cycle is often the result of many previous scattering cycles, forming a recursive pattern. Add to that the fact that more than one ray of light could be passing through a point x_0, and that scattering itself is

based on the integration of a probability density function (PDF), finding a solution to the RTE is difficult and in most cases cannot be analytically solved.

Chandrasekhar offered a solution to the RTE using H-function theory[64], which will not be discussed in this dissertation. This solution is only applicable when considering a semi-infinite homogenous medium, and uses an isotropic scattering phase function, which is not usually the case in biological media. Another solution in this case is the Eddington approximation[66], which once again only applies in a very specific case of light incidental on a plane.

To simplify solving for the RTE, it is common-place to make certain assumptions on the behavior of light which in turn reduces the number of independent variables.

$$RTE(\vec{r}, \hat{s}, t) \rightarrow DE(\vec{r}, t) \tag{2-33}$$

The overall approximation for this regime is that the scattering coefficient of the medium is much larger than the absorbing coefficient, which in turn means that scattering quickly reaches an isotropic distribution while not having been absorbed in any significant way. With this assumption in place, a derivation of the diffuse approximation (DA) can be offered.

Before deriving the diffusion equation, it is required to have an understanding of spherical harmonics and where these harmonics fit into simplifying the RTE into the DA. Harmonic functions, as stated by [67] are solutions to the Laplace's equation, and are used extensively in various fields such as the heat equation and interacting electric fields. Spherical harmonics (SH) may look daunting but offer a straightforward solution to Laplace's equation. First is the definition of a basis over a unit sphere with the following parametrization:

$$s =< x, y, z > =< sin\theta cos\phi, sin\theta sin\phi, cos\theta > \quad (2\text{-}34)$$

This basis should be familiar as it is simply the spherical coordinates of a unit sphere, defined with 0 except for on the edge of the unit circle. Laplace's equation in cartesian coordinate is:

$$\nabla^2\phi = 0 \quad (2\text{-}35)$$

Where ϕ is the quantity of interest. Converting Laplace's equation from cartesian coordinates to spherical coordinates gives the spherical harmonic differential equation (SHDE):

$$\left[\frac{1}{sin\theta}\frac{\partial}{\partial\theta}\left(sin\theta\frac{\partial}{\partial\theta}\right) + \frac{1}{\sin^2\theta}\frac{\partial^2}{\partial^2\phi} + l(l+1)\right]u = 0 \quad (2\text{-}36)$$

Humi [68] gave a solution to the above formula by using raising and lowering operators, which in turn define the spherical harmonics of the system. A brief explanation of spherical harmonics is provided by [69] and is presented below. Setting u to be $F = \Phi(\phi)\Theta(\theta)$ gives:

$$\left[\frac{1}{sin\theta}\frac{\partial}{\partial\theta}\left(sin\theta\frac{\partial}{\partial\theta}\right) + \frac{1}{\sin^2\theta}\frac{\partial^2}{\partial^2\phi} + l(l+1)\right]\Phi(\phi)\Theta(\theta) = 0 \quad (2\text{-}37)$$

Which when distributing the terms:

$$\left[\frac{\Phi(\phi)}{sin\theta}\frac{\partial}{\partial\theta}\left(sin\theta\frac{d\Theta}{d\theta}\right) + \frac{\Theta(\theta)}{\sin^2\theta}\frac{d^2\Phi(\phi)}{\partial^2\phi} + l(l+1)\Phi(\phi)\Theta(\theta)\right] = 0 \quad (2\text{-}38)$$

Multiplying the above equation with $\sin^2\theta\,/(\Theta\Phi)$ allows for the separation of variables. This separation of variables gives back 2 terms, one in terms of ϕ being constant and the other in terms of θ being constant. The two solutions to Laplace's equation are then:

$$\Phi(\phi) = Ae^{-im\phi} + Be^{im\phi}\text{ , } \phi \text{ portion is constant} \quad (2\text{-}39)$$

$$\Theta(\theta) = P_l^m(cos\theta)\ , \theta \text{ portion is constant}$$

In the above case, P_l^m represents the associated Legendre polynomial. The bounds of the problem statement are m=-1,-(l-1),…,0,…,l-1,l and l be . The spherical harmonics are then defined as the multiplication of $\Phi(\phi)\Theta(\theta)$:

$$Y_l^m(\theta,\phi) = \sqrt{\frac{2l+1}{4\pi}\frac{(l-m)!}{(l+m)!}}P_l^m(\cos\theta)\mathrm{e}^{\mathrm{i}m\phi} \tag{2-40}$$

The spherical harmonics defined above are a representation of a basis set for the expansion of radiance, which when expanded to the first order give back the diffuse approximation (DA)[63] in terms of an isotropic component and a first order anisotropic terms. The overlying assumption that the medium is largely isotropic makes this assumption possible.

$$L(\vec{r},\hat{s},t) \cong \sum_{n=0}^{l}\sum_{m=-n}^{n} L_{n,m}(\vec{r},t)Y_{n,m}(\hat{s}) \tag{2-41}$$

The expansion term n=0, m=0 represents the isotropic expansion, whereas the terms n=1,$m = 0, \pm 1$ would represent an anisotropic component.

Substituting the isotropic spherical harmonics term into the definition of fluence rate gives:

$$\phi(\vec{r},t) = 4\pi L_{0,0}(\vec{r},t)Y_{0,0}(\hat{s}) \tag{2-42}$$

The above equation means that the fluence rate ϕ is equally distributed over 4π solid angle. The anisotropic spherical harmonic terms can be introduced into eq. 37 so that s, which is the surface of a unit sphere, can then be expressed in terms of spherical harmonics expansion:

$$\hat{s} = \left(\sqrt{\frac{2\pi}{3}} \left(Y_{-1,1}(\hat{s}) - Y_{1,1}(\hat{s}) \right), \sqrt{\frac{2\pi}{3}}\, i \left[Y_{1,-1}(\hat{s}) + Y_{1,1}(\hat{s}) \right], 2\sqrt{\frac{\pi}{3}}\, Y_{1,0}(\hat{s}) \right) \tag{2-43}$$

The dot product multiplication of $\hat{s}$ by the definition of energy flux J gives the following term:

$$\vec{J}(\vec{r}, t) \cdot \hat{s} = \frac{4\pi}{3} \sum_{m=-1}^{1} L_{1,m}(\vec{r}, t) Y_{1,m}(\hat{s}) \tag{2-44}$$

The dot product of current density J with the unit vector field s represents a projection of current density onto $\hat{s}$.

The isotropic function and anisotropic function are then combined to formulate a definition of radiance:

$$L(\vec{r}, \hat{s}, t) = \frac{1}{4\pi} \phi(\vec{r}, t) + \frac{3}{4\pi} \vec{J}(\vec{r}, t) \cdot \hat{s} \tag{2-45}$$

The modified radiance equation can then be introduced into the formal RTE equation an after multiplying both sides by $\hat{s}$ and integrating the scattering element over the 4π solid angle gives the following:

$$\frac{1}{c} \frac{\partial \vec{J}(\vec{r}, t)}{\partial t} + (\mu_a + \mu_s') \vec{J}(\vec{r}, t) + \frac{1}{3} \nabla \phi(\vec{r}, t) = 0 \tag{2-46}$$

Where $\mu_s{}'$ is the reduced scattering coefficient described in a previous section. The above formula has two terms $J \; and \; \phi$, but the unit directional vector $\hat{s}$ does not appear in the equation, meaning that the scattering, being isotropic in nature in this simplification, does

not rely on the incident nature of an incoming beam. However, the anisotropy factor g is present in $\mu_s{}'$, where it can introduce some distribution of scattering based on the angle of the incident light to scattered light. Also, $\hat{s}$ is implicit in the definition of J. Therefore, a derivation that aims to eliminate J would be convenient. By assuming that the change in energy flux over unit time is small, then it is possible to reduce eq 48.to a simpler form as the time derivative goes to 0.

$$\vec{J}(\vec{r},t) = -\frac{1}{3(\mu_a + \mu_s')}\nabla\phi(\vec{r},t) \tag{2-47}$$

Where the variable group $\frac{1}{3(\mu_a+\mu_s')}$ is often treated as one variable D. The previous formula is an example of Fick's law [70] which is used to describe diffusion processes. The substitution of Fick's law into eq 48, reformatted in scalar differential form, then simplifies to:

$$\frac{1}{c}\frac{\partial\phi(\vec{r},t)}{\partial t} + \mu_a\phi(\vec{r},t) - \nabla\cdot[D\nabla\phi(\vec{r},t)] = S(\vec{r},t) \tag{2-48}$$

Which is the DE for the case that the diffusion approximation is applied. An inspection of the DE reveals several things. First, is the fact that the unit direction vector is not included in the final formula. This is convenient as it means that the number of inputs into the DA is less than the RTE, namely, $\vec{r}$ and t, as opposed to the RTE which takes 7 input parameters $(\vec{r},\hat{s},t)$. Also, the importance of not having $\hat{s}$ in the DE points out that an incoming light beam hitting position $\vec{r}$ will scatter completely isotropically, which is one of the defining axioms of using the DE.

A simple example of the use of DE is presented for a point source shining down on a single-layered homogenous medium. In this case, the source function S becomes:

$$S(\vec{r},t,\vec{r}',t') = \delta(\vec{r}-\vec{r}')\delta(t-t') \tag{2-49}$$

Where t'=0 and $\vec{r}' = 0$ which makes the above formula in terms of just $\vec{r}$ and t. Solving the DE for this situation gives:

$$\frac{1}{c}\frac{\partial\phi(\vec{r},t)}{\partial t} + \mu_a\phi(\vec{r},t) - \nabla\cdot[D\nabla\phi(\vec{r},t)] = \delta(\vec{r}-\vec{r}')\delta(t-t') \tag{2-50}$$

The above equation simplifies to the following and the derivation of this formula is extensively described by Wilson et al [71].

$$\phi(\vec{r},t) = \frac{c}{(4\pi Dct)^{\frac{3}{2}}}\exp\left(-\frac{\vec{r}^2}{4\pi Dct}\right)\exp(-\mu_a ct) \tag{2-51}$$

Two different time-independent plots are shown with final time-varying 2 units magnitude in a 2-dimensional spatial domain in figure 2-23.

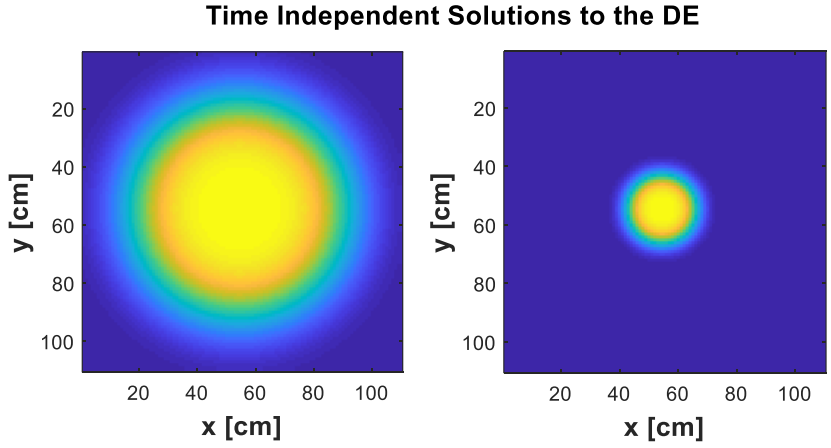

Figure 2-22 Time-Independent solutions to the DE

Graphical solutions from using the DE for a homogenous layer with time span equal to 5e-8 and 5e-10 seconds. μ_a and μ_s' are statically set to 1 cm^{-1}, with a point source isotropically launching from the center of the grid.

The previous figure should also be instrumental in understanding the flaws in using the DE. The distribution of light is entirely dependent on the distance between the source and the point being inspected, which is given by $\vec{r} - \vec{r}'$. This way of solving for light distribution is rapid as it is analytical.

However, the accuracy of using DE can impair the utility of using such a model. Errors in this model are especially large at distance close to the emitter and with narrow time spread function. This problem has been reported by [72] and [73], and many other groups. [73] reported that the DE has excellent accuracy compared to Monte Carlo models at a certain distance from the emitter ($r > 2/\mu_s'$) and at a certain elapsed time ($t > 4t_0$). [72] similarly noticed inaccuracies at distances smaller than R_{crit} where $R_{crit} = \frac{2}{\mu_s' + \mu_a}$. At points $r < R_{crit}$, the DE irradiances were highly inaccurate, but otherwise accurate compared to using an MC in spatial domains farther than R_{crit}. Both authors attribute the high inaccuracies in the DE to the fact that the DE uses approximations that no longer stand at these close-by points. One of the critical factors is the assumption that $\mu_s' \gg \mu_a$, which guarantees that the radiance is isotropic, however, below one transport mean free path, this condition is not necessarily true and can lead to model inaccuracies in the DE. The derivation of the DE in [63] has an explicit clause that the fractional change of current density over a distance l_t is negligible:

$$\left(\frac{l_t}{c}\right)\left(\frac{1}{\left|\vec{J}(\vec{r},t)\right|}\left|\frac{\partial \vec{J}(\vec{r},t)}{\partial t}\right|\right) \ll 1 \qquad (2\text{-}52)$$

Where l_t is known as the transport mean free path (TMFP) and the time to traverse l_t is known as the transport mean free time (TMFT). In order for the above stipulation to hold true, both the first and second pairs of parentheses must be much smaller than 1. Holding l_t static, the change in current density must be much smaller than the magnitude of the current density:

$$\left|\frac{\partial \vec{J}(\vec{r},t)}{\partial t}\right| \ll C\,\vec{J}(\vec{r},t) \tag{2-53}$$

Where C is a constant in this case related to μ_a and μ_s'. However, close to the source, radiance does not follow this stipulation. A disk beam coming from the top-down will tend to have a particular scattering direction in biological tissue for the first few scattering cycles, for example, and thus does not follow the DE assumptions for these initial scattering cycles. The same argument can be made for a short TMFT. When using a time t very close to t_0, there could be, just as in the case of distance, an unaccounted effect due to early anisotropic effects.

A Brief History of Monte-Carlo Methods in Optics

Monte-Carlo (MC) has been used extensively in various fields such as finances[74] and geothermal analysis[75]. While there is no formal definition for what an MC method (MCm) is, generally, MCm's fall into a category of computational problem solvers that function of randomly generated numbers and inverse sampling to solve deterministic problems. The idea of solving a problem that may be deterministic in nature, but difficult to solve analytically, with MC, was first formally introduced in the late 1940's by John Von Neumann, who used a MC method to explore radiation shielding in different materials. This story is recounted in a paper by Eckhardt[76]. Very briefly,

Von Neumann was intrigued by the idea of using an MCm to serve as a practical method to “abstract thinking”. He further concluded that “the statistical approach is very well suited to a digital treatment”, where the digital treatment he was talking about was using an MCm to solve neutron diffusion in fission devices. At the time, MC was not the official name given to these stochastic methods; however, a colleague of Von Neumann, Nicholas Metropolis, suggested naming the technique after the city of Monte Carlo, Monaco, which was well-known for gambling. Since, MCs have gained traction, being used for ever more complicated problems such as analyzing the quantum many-body problem, an analysis of interactions between many microscopic systems which are small enough to fall under the regime of quantum mechanics[77] and potentially discovering hidden planetary systems outside of the solar system[78].

MC’s, while not having a central definition, generally follow a series of simple rules when solving a problem[79]. These rules are:

- Modeling of the system as a series of probability density functions (PDFs)
- Repeatedly extracting from the PDF by using a randomly generated number
- Aggregate statistics of interest

Using these basic rules, most problems that are deemed unsolvable or difficult to solve by traditional analytical methods become “solvable” using an MC approach.

As a simple example, the value of pi can be estimated using a quarter circle inscribed inside a unit square. Randomly generated points are then thrown on the grid, and π can be estimated by counting the number of points inside the grid vs all the points and equating the ratio to $\pi/4$.

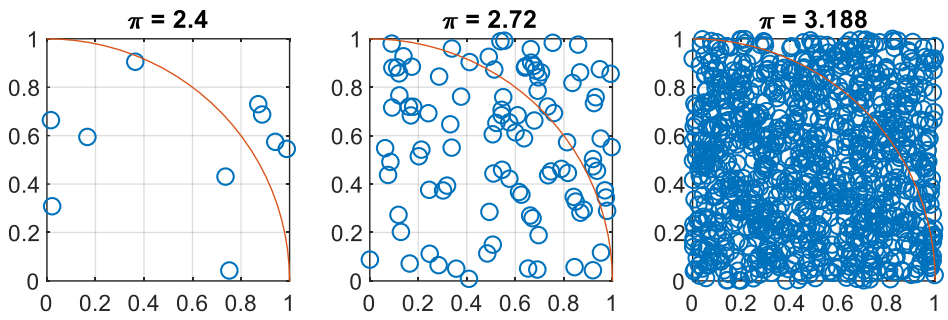

Figure 2-23. Estimation of π using MC method

The estimation of π done with 10, 100 and 1000 points. As the number of randomly generated points increases, the estimated value π reaches an expected value of π.

The above problem uses generated random numbers to find a deterministic answer for π. The accuracy of the model heavily depends on the number of sampled pairs of coordinates. With ten generated samples, the accuracy of the calculated number is approximately an integer of the expected value of π. By launching 1000 random points, the accuracy of π is within one decimal point. By launching 1e7 sample points, the generated value of π is 3.1397, which is close enough to the actual value of π for most engineering applications. In the circle model described above, the inputs are the 2-dimensional coordinates, randomly sampled from 0 to 1 inclusive in x and y. From these coordinates, an extracted value of π can be formulated, and this value gets close to the actual value of π with an increased number of data points. However, this technique requires a large sample pool, as do most MCms, in order to return a result that is accurate and precise.

MCs were introduced in the field of optics in the 1980s, with Wilson et al. [80] publishing an article on the subject of using MC methods to solve for radiance in a homogenous tissue. A beam of light was simulated entering the medium with user-specified μ_a and μ_s. The incident light beam was either orthogonal to the surface of the medium as a disk type source or could simulate a fiber optic inside the medium with an exit angle of the fiber being specified by the numerical aperture (NA) of the fiber. Each photon packet was launched in the medium following a distribution set by the launch function, after which the photon packets were tracked in terms of scattering and absorption. The photon packets were only allowed to scatter 4 to 8 times in an isotropic pattern after the initial launch with a scattering length s specified by:

$$s = -\ln(\epsilon)/\mu_t \tag{2-54}$$

Where ϵ is a pseudo-random number between 0 and 1 inclusive. At each scattering site, a percentage weight of the photon packet, initially set to unity, was deposited at the site as a percent of the incoming weight multiplied by the ratio of absorbing to attenuation ratio as follows:

$$W \leftarrow \frac{\mu_a}{\mu_t} W \tag{2-55}$$

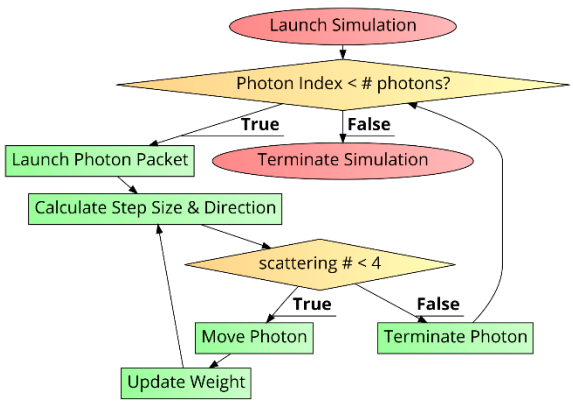

Figure 2-24. Flowchart for the MC model proposed by Wilson et al. in 1983

The flowchart represents the logical steps taken to simulate photon propagation in a homogenous medium. The scattering cycles max number is hardcoded to 4, though 8 was also used in Wilson's simulations. The simulation ends when the photon index of the current photon packet exceeds the total number of photons launched. The photon packet scatters four times, after which the flow loops to the initialization of a new photon with the initial direction set by a source distribution.

The program was written in FORTRAN and took 75 to 125 minutes to calculate the photon distribution for 1e5 photon packets launched. Wilson commented on the novelty of using an MC model to inspect light dosimetry in tissues, noting that MCs had been widely used in ionizing radiation treatments of the time. However, several issues were described that hindered the accuracy of their model. These issues were:

- Improving the number of scattering events per photon packet
- Allowing for photon packets to be scattered anisotropically
- Allowing for non-homogenous arbitrary model tissues
- Accounting for interface boundaries
- Diversifying the illumination geometries
- Tracking a photon packet in terms of the spatial and directional component

Over the next decade, groups aimed to improve MCms to overcome some of these limitations with varied success. After Wilson came Keijzer et al. [81] in 1989, who aimed at introducing anisotropic scattering in their models by using the Henyey-Greenstein to calculate deflection trajectories. The Henyey-Greenstein function [10], formulated by Henyey and Greenstein in 1941, is shown below:

$$p(\theta) = \frac{1}{4\pi} \frac{1 - g^2}{(1 + g^2 - 2gcos\theta)^{\frac{3}{2}}} \quad (2\text{-}56)$$

Where θ is the scattering direction relative to the incident beam.

The scattering direction in 3-dimensions requires two independently sampled random variables, one in the azimuthal direction (longitudinal to the incident direction of a photon) and one that is lateral to the incident beam. The Henyey-Greenstein function can approximate light scattering well, as discussed by Jacques[52]; the Henyey-Greenstein function was originally implemented to study atmospheric Mie scattering but was implemented to represent anisotropic scattering in microscopic and macroscopic media after Jacques found that the function analytically compared to experimental behaviors for multiple scattering.

Prahl and Jacques offered some papers in the late ’80s and early ’90s which aimed to find resolutions to the 6 problems stated by Wilson. In 1989, Prahl published an “A Monte Carlo model of light propagation in tissue”, which aimed to describe photon propagation through any media, which considers anisotropic scattering by the Henyey-Greenstein function, takes multiple layers with different optical properties, considers refractive mismatches between the layers, considers internal and external specular reflection. However, it would not be until 1995 that Jacques and Wang[82] would propose a light propagation model that could work readily on most computers (as it is written in the C programmatic language) and would formally resolve the issues mentioned by Wilson. This model will be discussed in the next heading.

MCML – a general starting point

MCML – Monte Carlo model of steady-state light transport in multi-layered tissues – has been extensively modified over the years to simulate different light effects in tissue. However, in this section, only the base MCML will be described.

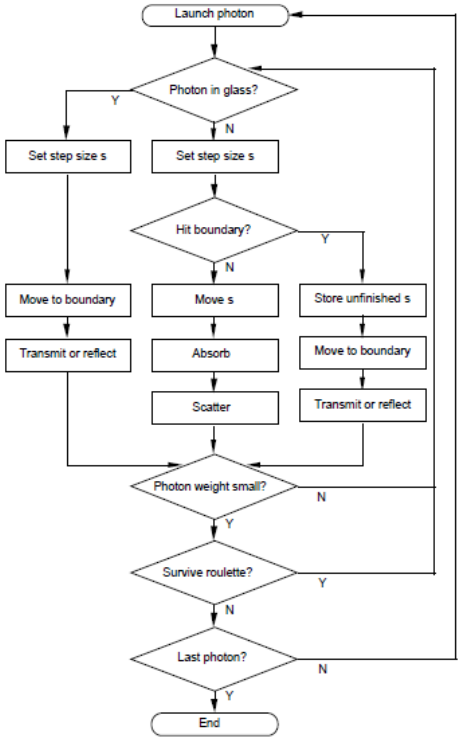

Figure 2-25. Flowchart for MCML

The flow chart shows the procedure elements considered and the steps taken to run the algorithm. The outer loop controls the number of photons launched, the 1st nested loop controls for a "roulette" term described in the text, the 2nd nested loop controls for whether the photon packet weight is below a threshold.

In MCML, a photon trajectory is started from above the multi-layered medium, heading straight down. At the boundary between the ambient medium and the relevant medium, Fresnel reflection is calculated by the formula:

$$R_{sp} = \frac{(n_1 - n_2)^2}{(n_1 + n_2)^2} \tag{2-57}$$

The weight of the photon packet is then reduced to 1 - R_{sp} when initially entering the medium. Next, the step size of the photon packet is calculated using an inverse sampling method.

$$s = -\frac{\ln(\epsilon)}{\mu_t} \tag{2-58}$$

Where μ_t is the attenuation coefficient for the first non-ambient layer in the medium (in most cases). Once the photon packet has moved the scattering length into the medium, it leaves behind some of its weight at the local grid it is placed in, which, just like with Wilson's model, is a ratio of absorbance to attenuation coefficients. Then, a new photon trajectory is computed by the Henyey-Greenstein function:

$$\cos\theta = \begin{cases} \frac{1}{2g}\left[1 + g^2 - \left(\frac{(1 - g^2)}{1 - g + 2g\epsilon}\right)^2\right], & g \neq 0 \\ 2\epsilon - 1, & g = 0 \end{cases} \tag{2-59}$$

When g is equal to 0, then Henyey-Greenstein is equivalently $1/4\pi$ over all angles and so can be set to a simpler function $2\epsilon - 1$.

There is a chance that the photon packet will hit an internal or edge boundary, which is taken care of in MCML. The distance between the photon packet's current location and the boundary of the layer in the direction of the velocity of the photon packet is calculated and compared to the step size s. If it turns out that s is greater than the boundary distance, then the photon is moved to the boundary of the layer, after which 2 scenarios are considered.

- Transmittance from Layer 1 to Layer 2 (Assuming photon packet is in layer 1)
- Internal reflection in Layer 1

The incident angle to the boundary wall is calculated using $\theta_i = \cos^{-1}|\mu_z|$ where μ_z is the z-component of the directional vector of the photon packet. If the critical angle θ_c, calculated as $\sin^{-1} n_t/n_i$ is smaller than θ_i, then the beam is internally reflected. If $\theta_i < \theta_c$, then a random number is produced and compared to the internal reflectance value, which is calculated as:

$$R(\theta_i) = \frac{1}{2}\left(\frac{\sin^2\theta_i - \theta_t}{\sin^2\theta_i + \theta_t} + \frac{\tan^2\theta_i - \theta_t}{\tan^2\theta_i + \theta_t}\right) \tag{2-60}$$

Where θ_t is the transmission angle from layer 1 to layer 2, calculated by Snell's law ($n_1 sin\theta_1 = n_2 sin\theta_2$). If the value of ϵ falls below or equal to the internal reflection value, which is guaranteed when $\theta_i > \theta_c$, then the photon packet is internally reflected, otherwise, the photon packet is transmitted through to the second layer or the ambient medium. In the case, that the photon exits the layer into an ambient medium, then it is terminated, and the algorithm sequentially moves on to the next photon packet. If the photon packet is transmitted into another layer, then its trajectory is updated to be:

$$\begin{aligned} \mu_x' &= \mu_x n_i/n_t \\ \mu_y' &= \mu_y n_i/n_t \\ \mu_z' &= SIGN(\mu_z) cos\theta_i \end{aligned} \tag{2-61}$$

The photon packet then re-launches to accomplish its remaining trajectory according to what is leftover of its original s minus the distance traveled to the boundary. At each step, absorbance occurs at the voxel according to Beer's-Lambert law:

$$W \leftarrow W\left(\frac{\mu_a}{\mu_t}\right) \tag{2-62}$$

The photon packet is allowed to repeat many cycles of scattering and absorbing until the weight of the photon packet reaches a particular level (i.e. 1% of initial weight), after which the photon packet will enter a "Russian Roulette" style termination technique. The Russian roulette scheme is well-suited to termination in Monte-Carlo techniques; as commented by [83] it is the most widely used variance-reduction technique. In MCML, the Russian Roulette reduces the bias of photon termination prematurely, by allowing the photon to propagate with weight:

$$W_{i+1} = \begin{cases} mW_i, & \epsilon \leq 1/m \\ 0, & \epsilon > 1/m \end{cases} \tag{2-63}$$

Where m is an integer positive number that represents the number of bins of which only one will allow the photon to continue through to the next cycle. This Russian Roulette only applies once a photon weight has been registered with a value underneath a preset user threshold.

This model and subsequent variations in this model have been used since to inspect multilayered tissue such as the epithelial skin in neonates [84] and skin cancer intrusions [85-87] and the head and brain[88-90] as some examples.

MC for modeling Fluoresence

Fluorescence MC's have a history that spans back as far as diffuse MC's. It was Kiejser et al. who first proposed an MC for fluorescence in 1989 [91]. This MC model was used to inspect the fluorescence of the aorta as it relates to collection geometries and

optical tissue properties. The MC model worked as a convolution of excitation absorption, with the distribution of fluorescence sources:

(2-64)

$$F(\lambda, \boldsymbol{r}) = \int_0^D \int_0^{2\pi} \int_0^{\infty} \Psi(\boldsymbol{r'}, \boldsymbol{z'}) \beta(\lambda, \boldsymbol{z'})\, X\, E\left(\lambda, \sqrt{\boldsymbol{r^2} + \boldsymbol{r'^2} - \boldsymbol{2rr'}\cos(\theta')}, \boldsymbol{z'}\right) r' d\boldsymbol{r'} d\theta' dz'$$

Where E is the escape function representing the fluorescence from a particular depth point source, D is the thickness of the sample, Ψ is the initial absorption distribution, θ' is the difference in azimuth angle between r and r', z' is the depth in the tissue and β is the intrinsic Fluorescence coefficient, which is the product of quantum yield of the chromophore with its μ_a at the emission wavelength. Using this formula, Keijzer et al. were able to conduct a theoretical exploration of the human aorta with different optical properties, and different collection efficiencies. They concluded that using a single-fiber system was most appropriate for detecting tissue differences at the surface, but that capturing light with fiber at a further offset was beneficial for capturing non-surface based fluorophore, but with less efficiency. This way of modeling fluorescence was used by other groups over the years. Zeng et al. [92] used the same methodology to explore skin autofluorescence with a 442- nm He-Cd laser, noting that the recovered spectrum tended to more and more tilted in term of z as the absorption and scattering coefficients decreased with increasing wavelengths.

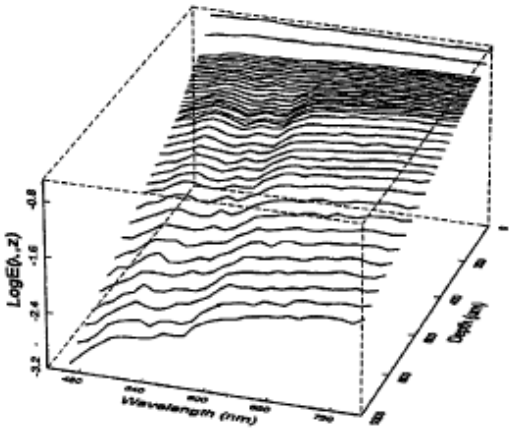

Figure 2-26. Modeleld fluorescence escape efficiency E for skin's first 1000 μm. Retrieved from Ref. [93].

A similar study was performed by Wang et al. [94], who used this model to explore relative contributions to the overall fluorescence signal from the different layers of the skin, commenting on the influence of the epidermis's and dermis's layers.

Another way to approach the problem of modeling fluorescence was proposed by Liu[95], who approached the problem by modifying the input optical properties placed in the model. The first assumption is that there is a probability of a photon being absorbed either by an absorber or a fluorophore, but without emitting fluorescence, which is defined as:

$$P_{nf} = \frac{\mu_{ac}(1-\phi_c)}{\mu_{ac}+\mu_{sc}} \tag{2-65}$$

Where μ_{ac} is the combined fluorescence and absorbing coefficients $\mu_a + \mu_{af}$, and ϕ_c is the quantum yield and $\mu_{sc}$is the scattering coefficient. The probability that a photon is fluorescent simply requires that the 1-ϕ_c term be replaced with ϕ_c. By setting these

equations to be equal to the overall probabilities that the photon can or cannot be fluorescent after being absorbed gives:

$$\frac{\mu_{a,f}\phi}{\mu_a + \mu_{af} + \mu_s} = \frac{\mu_{a,c}\phi_c}{\mu_{ac} + \mu_{sc}} \tag{2-66}$$

$$\frac{\mu_s}{\mu_a + \mu_{af} + \mu_s} = \frac{\mu_{sc}}{\mu_{ac} + \mu_{sc}} \tag{2-67}$$

Solving for μ_{ac}, ϕ_c and μ_{sc} gives the modified input parameters for the MC model (i.e. $\mu_a \rightarrow \mu_{ac}, \mu_s \rightarrow \mu_{sc}$). Using this framework, Qiu et al. were able to validate the model using artificial phantoms and show that the model worked well. However, the simulations took several hours to several days, depending on the number of photons simulated.

Mycek and Vishwanath proposed a new MC model in 2005 [96] for simulating fluorescence based on inversely sampling the probability of a photon becoming fluorescent. The photon starts its life as a regular photon, following the prescribed diffuse MC rules. However, at each step, there is a new checked variable, which compares a random number to the probability of the photon being fluorescently emitted. In the case that fluorescence does occur, the photon is then scattered isotropically, a time-delay τ is added to the time of flight of the photon and it continues its propagation according to the optical emission properties. Using this model, Mycek was able to produce maps of fluorescence distributions in a bi-layered model, with different fluorophores and different lifetimes, inspected with different fiber optic probe configurations.

MC for modeling Raman Scattering

At the same time as fluorescence models were being developed, Raman models were also being developed.

Matousek used an MC model, that was similar to a code proposed by Pfefer for fluorescence[97], which kept track of where in the medium diffuse photons converted to Raman photons, according to hard-set probability. This model was used to inspect subsurface Raman effects in a theoretical multi-layered model [98], which was later validated using *trans*-stilbene powder and PMMA powder phantoms [99]. The aim of these investigations was to validate that spatially offset Raman spectroscopy (SORS) could be a valuable method for investigating subsurface Raman signals while suppressing contributions from surface-level Raman effects. Everall, at about the same time, proposed a model that just like Matousek, assumes that the probability of Raman scatter is checked against a hard-set limit P_{ram} [100]. However, Everall was interested in the time dynamics of the system, using the model to explore Kerr-gated picosecond time-resolved Raman spectroscopy [101] as opposed to SORS. Keller et al. later used a model based on Mycek's method for fluorescence MC [96], with a time-delay set to be 0, to investigate SORS in modeled breast cancer tissues[102], with a new parameters $R_{s,i}$ representing a Raman cross-section. Using this model, Keller et al. were able to show Raman scattering as a function of source-detector offset in determining breast cancer thresholds in terms of the depth and size of tumor. Wang et al. used the convolution method shown in eq 67 modified to inspect Raman scatter instead of fluorescence by modifying β to be the intrinsic Raman coefficients instead being the intrinsic fluorescence coefficient[103] to inspect the layered contributions to overall signal captured at the surface of the skin.

Other groups have also modeled Raman spectroscopy to determine signal for embedded hidden objects [104, 105] and inspect spatial distribution of Raman sensitivity dependent on measurement geometry [106].

More in-depth review papers on the subject of general MC models, as well as fluorescence and Raman MC models, are offered by [107] and [108].

Acceleration in MC

MC's for simulating photon propagating through turbid media is now considered a gold standard [107-109] when it comes to forward modeling propagation through a medium with known geometry and optical properties. However, MC-based models are less computationally efficient than their analytical counterparts, due to their stochastic nature, which makes obtaining results a much more arduous and time-consuming task. Therefore, over the years, methods for accelerating MCs through algorithmic amelioration have been proposed by various groups, which are broadly divided into 3 different categories:

- Scaling Methods
- Perturbation Methods
- Variance Reduction Methods

Scaling methods are based on the fact that the scattering properties are responsible for the photon packet's path and the absorption properties are responsible for the weight reduction at each scattered site [107] independently. Knowledge of the scattering paths are thus only dependent on the scattering coefficient and knowledge of the absorbance is only dependent on the absorption coefficient, and variants of these two properties can be

entered and solved for with path length and absorption from a reference MC simulation. Graaff et al.[110] proposed a scaling method in 1993, noting that "Monte Carlo results can be used again in simulations with the same phase function and albedo but where μ_t is different". A scaling approximation was used to find the reflectance and transmission of a slab of tissue with 2 different absorption values, which were compared to results from Prahl[61]. The scaling method showed that only 1 MC simulation at a reference albedo was necessary to generate results for a large range of albedos. Liu et al.[111] used the principles offered by Graaff and used scaled MC to calculate reflectance over a wide range of optical properties in multiple layered turbid media. Using one reference MC simulation, Liu et al. were able to get comparable results in 2- and 3- layered epithelial tissue models compared to running independent MC for each optical property, reducing the time dependence dramatically while still getting relevant data. Pifferi et al [112] used an interpolation over several MC references to improve the accuracy of their scaling model. 5 different μ_a and μ_s' were simulated over 1.5 to 24 cm^{-1} and 0.1-1.6 cm^{-1} respectively. Experimental reflectance and transmission measurements were gotten from phantoms and iteratively compared to an interpolated simulation map. The comparison of experimental and simulation were generally below 10% for μ_a for a particular range of $\mu_s{}'$, indicating that an interpolated scaling method can bring more accuracy than just a single run scaling approximation.

Perturbation methods in MCs are based on the perturbation theory[113], which separates a problem into two components; an unperturbed reference measurement and a perturbed measurement which has similar but not identical optical properties. The

perturbed response is then linked to the unperturbed reference by the difference in optical properties between the two.

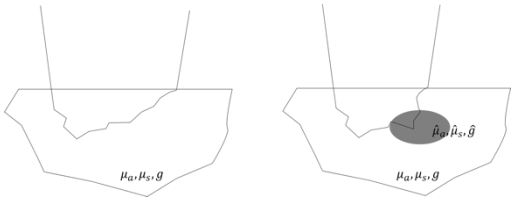

Figure 2-27. Homogenous and perturbed media, with a single photon path length shown

A full simulation through the homogenous medium is done in pMC, followed by a partial MC that begins when the packet hits the spheroid inside the tissue. It is not necessary to do simulations through the homogenous medium of the turbid medium since it can be described by the homogenous solution.

That is to say, if one medium is a homogenous tissue with static optical properties and the other medium is the same medium with a small spherical shape buried inside, the perturbation theory would simply copy the initial parts of the path from the reference simulations until the sphere is reached, at which point a new MC can be started, which can cause a significant time reduction. The new weight of the photon packet through this perturbed area is then:

$$w_{new} = w\left(\frac{\mu_s^n}{\mu_s}\right)^j \exp([-(\mu_t^n - \mu_t)S]) \tag{2-68}$$

Applicable only once the reference and sample's optical properties become different. The parameters with an n represent the sample's optical properties, S is the perturbed path length and j is the number of collisions of the perturbed sample. Using this technique, Sassaroli et al. [114] were able to make an MC method that uses one complete

MC reference simulation, and one partial MC simulation for a sample under inspection (a slab similar to the homogenous reference but with totally absorbing spherical defects hidden inside) to produce results similar to running an independent MC, but with time constraints being significantly less. Other groups have also taken advantage of the perturbation MC (pMC) [115-117] to explore multi-layered media. Seo et al.[117] used a combination of pMCs and differential MCs (dMC) to solve for optical properties in heterogeneous systems, claiming that by using this method, probe designs could be quantitively optimized.

Variance reduction techniques are often used in MC methods, as they can provide a better estimation of light-matter interactions. One such technique responsible for photon termination in the MCML program is called roulette, or importance sampling [118, 119], which terminates a photon in an unbiased way. After the photon reaches a termination threshold W_{th}, it is then engaged in a "Russian-Roulette" like process, where the probability of the photon being terminated equals:

$$W \leftarrow \begin{cases} mW & if\ \epsilon \leq 1/m \\ 0 & if\ \epsilon > 1/m \end{cases} \tag{2-69}$$

In this manner, the routine is faster, as photons are terminated earlier on average, while not introducing a bias in the system.

Acceleration in MC due to hardware improvements

In 2007, the Compute Unified Device Architecture (CUDA) platform from Nvidia was released, which made the Graphics Processing Unit (GPU) more accessible than in previous years. CUDA made the adaptation of workflows that were inherently

parallelizable possible to port to the graphics card, including the task of modeling photon propagation. Practically, a single photon, from initialization to termination, is not dependent on any previous photon trajectory. This means that the MCML and other similar codes were able to be massively accelerated by the GPU. Alerstam et al. were one of the first groups to use this platform to accelerate MCML[120, 121] massively. Afterward, they released the source code and binaries of CUDAMCML [120], and it and subsequent variations are still being used today in a variety of bioengineering studies[121-123].

In 2009, Fang et al. introduced a more versatile and flexible MC simulator on the CUDA platform, called MCX (Monte Carlo eXtreme), which could provide many light sources past a pencil-beam, or Gaussian beam, and was designed from the start to be as efficient as possible on the GPU[89]. This code can perform up to 1000x faster than sequential models depending on the installed graphics card. This platform is still being used in diverse fields such as photacoustics[124], time-resolved NIR spectroscopy[125] and hemodynamic responses to speech[126] are some recent studies that used MCX to simulate photon propagation in particular contexts.

Optical technqiques in tissue and *in-vivo* diagnostics

Optical spectroscopy and imaging have become popular tools in tissue diagnostics *in-vivo* in recent years. The properties of the body can be queried using non-ionizing light, which poses no threat to the patient and the medical staff, and can reveal structural, morphological and biochemical information that can further be used to diagnose and potentially treat a patient (i.e., photodynamic therapy, cold-laser therapy). As such, optical spectrometry and imaging have been gaining popularity, coinciding with constant

and novel improvements in technologies such as in spectrometers and detectors, which means an explosive adoption of optical devices for clinical and biomedical applications using light-based technologies. Some of these broader platforms are described in the following sections. Briefly, this include ballistic light technologies such as optical coherence tomography (OCT), diffuse systems such as confocal laser scanning microscopy (CLSM), diffuse optical tomography (DOT) and diffuse optical imaging (DOI), Raman spectroscopy, such as spontaneous Raman (SR), spatially offset Raman spectroscopy (SORS), stimulated Raman spectroscopy (SRS), and coherent anti-stokes Raman spectroscopy (CARS), and fluorescence techniques such as exogenous-dye Fluorescence, autofluorescence, second and third harmonic generation (SHG, THG) and two-photon Fluorescence.

Optical Coherence Tomography

OCT is a technique based on the ballistic trajectory of a photon, i.e., a photon that traverses a scattering tissue in a straight line, with only a few scattering events. OCT uses low-coherence light to capture micrometer-scale images of tissue, and typically uses NIR wavelength light, which has a higher penetrating power in biological tissue ($\mu_s' \gg \mu_a$). It is sometimes referenced as “optical ultrasound” although recently, with the introduction of photoacoustics, less so. OCT works by using an interferometer, typically a Michelson type interferometer, and a low-coherence light source. The low-coherence light is split into two parts, a reference arm, and a sample arm, and the light rays are recombined after the sample arm has interacted with the sample. Because the reference arm is able to move in its longitudinal axis, an interference pattern of the two beams can be made, but only if the optical distance traveled by both beams are in the same range. Because of this OCT is

able to scan 3-dimensional volumes with high accuracy by its rejection of photons that have scattered too many times and fall outside this optical distance. OCT was originally coined in 1991 by James Fujimoto of MIT[127] and has grown in popularity over the years as it is a low-level light technique that does not damage the sample by over-illumination, while at the same time producing high-resolution microscale high-fidelity 1, 2 and 3-dimensional images. There are several distinct OCT methodologies that have come out over the years; the biggest ones are Time-domain OCT (TD-OCT), which is the original OCT method[127], Frequency-domain OCT (FD-OCT), which introduces an additional grating, sensor grating or spectrometer that can allow for the high-speed scanning without loss of resolution[128, 129], Swept-Source OCT (SS-OCT), which uses a coherent laser source as the illumination beam, and polarization-sensitive OCT(PD-OCT), which can provide structural orientation of samples by using the polarization of the source[128]. Because of the key features of OCT (instant, direct measurements of tissue morphology, no preparation, live subsurface imaging at microscopic scale), OCT is commonly used in ophthalmology[130-133], cardiology[134-136], oncology[137-141] and dermatology[142-144].

Confocal laser scanning microscopy

Confocal laser scanning microscopy (CLSM) is an optical method that increases the optical resolution and contrast of viewed images by using a scanning platform and a spatial pinhole in tandem to reject any out-of-focus signal, thus providing a cleaner and more resolute image than OCT at the offset of taking more time to perform its imaging task. Fig 29 shows a typical CLSM platform. Light from a laser source is passed through a collimating lens, after which it reflects off a beamsplitter, and then passes through a set

of scanning mirrors, which can very accurately tilt the light in the x and y-plane. After being scanned, the beam reaches the back of an objective lens, which focuses the beam onto the sample. The light then returns the same way as the initial laser beam, transmitting through the beamsplitter, and to a second lens that focuses the light, which then passes through a pinhole. The addition of this pinhole means that any signal that does not belong to the particular XYZ position being imaged on the sample is rejected, so that only relevant signal passes through. This can provide images that have more resolution than OCT; the increased time commitment comes from the scanning part of the system. Finally, the light that has made it through the pinhole passes to a photomultiplier tube (PMT), which converts incoming photons into electrons, which are then digitized and passed to a viewing platform on a computer.

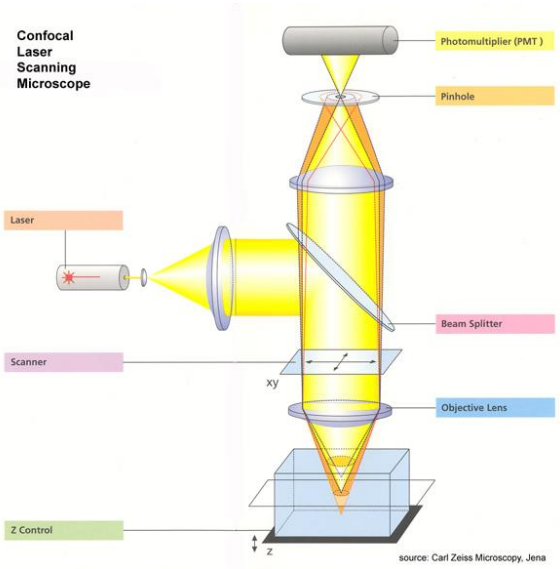

Figure 2-28. A typical CLSM apparatus, retrieved from [145]

When this methodology is combined with fluorescence (fluorescence CLSM), or Raman (Raman CLSM), filters would need to be attached that rejects the absorption

wavelengths in fluorescence or the Raman laser line, but the advantage in both settings is an enhanced image which can reveal micro-resolution morphological and biochemical structures that are dependent on the lateral spacing, and also the depth into the sample being investigated.

CLSM has been in use since the 1960s when Marvin Minsky patented the principle[146]. Since, it has been used to explore all types of biological tissues, such as collagen waviness in the arterial adventitia[147] and to explore melanocytic skin tumors[148].

Diffuse Optical Imaging

Diffuse optical imaging (DOI) is a diffuse technique (multiple scattering events) usually applied in the VIS and NIR regime which aims at reconstructing a 2- or 3-dimensional quantitative mapping of optical properties based on light-matter interactions in scattering media. A light, either as LEDs or laser diodes, is shone on a biological matter, and owing to the optical properties of the sample, the light will return the surface after optical interaction with the sample differentially. The light that reaches the surface is measured and fed into a model-based image reconstruction scheme and the optical properties can be reconstructed. Since the photon has had multiple scattering events before reaching the surface, the calculation of optical properties from the returned signal is not as easy as with OCT. Instead, groups have tried to solve for the optical properties using inverse MC models (these are ill-posed non-linear problems, and therefore difficult to solve, and are slow to provide solutions[149]), or with numerical linear and non-linear solvers with regularization methods [150].

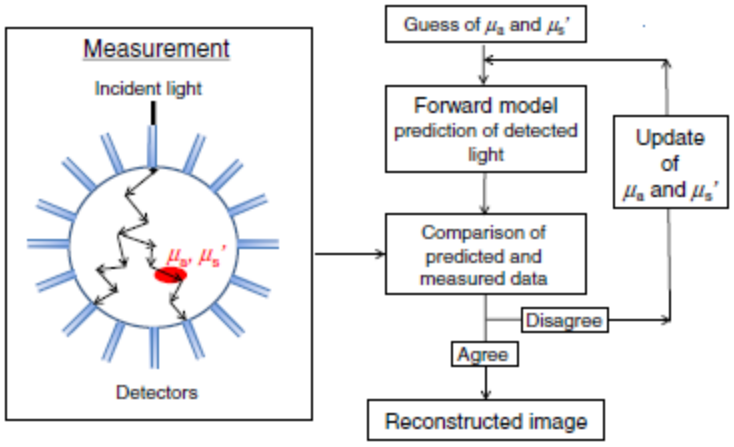

Figure 2-29. Model-based iterative image reconstruction scheme, retrieved from [151]

In Fig 30, light is launched from the top (illumination source) and scatters and absorbs in the circle while propagating to the detectors. Using the information from the detectors, as well as an inverse MC model, the optical properties can be retrieved. In diffuse optical tomography (DOT), this is done with many illumination sources[128, 142, 143, 152]. Other groups have used frequency-based approaches such as spatial-frequency domain imaging (SFDI)[153-155] and frequency-domain photon migration (FDPM)[59, 156, 157].

Raman Spectroscopy Techniques

Raman spectroscopy is the method that allows for the capture of Raman scattered photons. A simple example of Raman setup is presented in Fig 30.

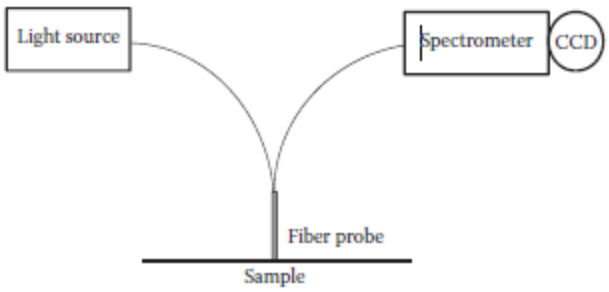

Figure 2-30. Schematic of a Raman fiber-optics probe and spectrometer setup for tissue diagnosis. Retrieved from [11].

Since Raman scattering is such a weak effect compared to the elastic scattering, a filter is typically placed in the detected light path that rejects the elastic light. The light source is usually a laser with narrow bandwidth, to increase the resolution of the recuperated spectrum. The spectrometer and detector are dependent on the light being captured. For UV-VIS excitation source, silicone charged-couple device (CCD) detectors are used, whereas for longer wavelengths in the UV-NIR-IR regime, indium gallium arsenide (InGaAs), germanium or indium phosphate (InP) may be used. Even though the Raman effect is a weak phenomenon, it is useful in determining the biochemical content of a sample, as the returned spectrum is indicative of an active vibrational mode. Therefore, Raman spectroscopy has been used to study breast cancer[158-160], brain cancer[161-164], lung cancer[165] and skin cancer[93, 166, 167] and pre-cervical cancer[168] to name a few examples.

A challenge in clinical Raman spectroscopy is the innate presence of autofluorescence when interrogating biological tissues[169]. Autofluorescence occurs at the same frequency range as Raman signal, and can be magnitude scale larger than the

biochemically relevant Raman features, and the noise produced by fluorescence can surpass the Raman peaks. Efforts have been made to subtract and minimize the impact of autofluorescence in two ways: mathematical subtraction of autofluorescence, and instrumentation based approaches. Numerical techniques are applied as a post-processing step after capturing a raw Raman signal, with algorithms that aim at separating the lower frequency autofluorescence from the higher frequency Raman features. There have been many algorithms proposed over the years, ranging from first and second-order differentiation[170], frequency-domain filtering[171], and polynomial fitting[169, 172, 173]. These techniques have different strong and weak points attached to them; for example, the differentiation technique is an efficient method for fluorescence subtraction; however, the Raman features can end up distorted and requires a sophisticated fitting algorithm to reconstruct the Raman line shapes[171]. Groups have also looked at implementing structural changes to Raman spectroscopy to diminish the unwanted autofluorescence curve. Some of the earlier hardware methods include wavelength shifting[174] and time-gating[175], which have both shown promise at minimizing fluorescence interference. More recent hardware changes include the use of NIR laser sources combined with new material for cameras made of InGaAs or germanium[11, 176-178], and the implementation of stimulated Raman platforms[179, 180], though these systems are more expensive and complex. However, be it numerical or hardware improvements, the objective of these techniques are to minimize signal interference from the fluorescent background, which must be done in order to use Raman spectroscopy in the clinic[11].

Spatially Offset Raman Spectroscopy

Spatially offset Raman Spectroscopy (SORS) is a method that uses the Raman methodology with varying detector placements to query more in-depth layer information from the sample. A minimum of 2 measurements is taken one at the source illumination and one further away in a lateral dimension. By using this schema, the photon measurements can be taken that represent deeper tissue zones, as photons that have scattered deeper in the tissue are much more likely to propagate back to the surface with a lateral dimension.

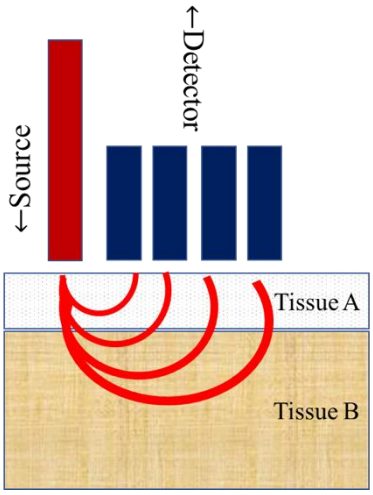

Figure 2-31. The principle of SORS

Several fiber optics positions will retrieve varied information of layer A to layer B. The fibers closer to the illumination source will tend to describe the superficial layers and as the detector fibers get further away, the measured signal will have more information about the deeper layer.

SORS was first used by Matousek[98] and has since been used in pharmaceutical authentication[181], transcutaneous glucose sensing[182] and in breast tumor evaluation and margin threshold analysis[102, 183].

Stimulated Raman Spectroscopy Techniques

With spontaneous RS, or with SORS, there remains the problem of a weak Raman signal, which in most biological tissue, also rides atop a medium to strong fluorescence signal. Several groups have tried to mitigate this factor by using longer wavelengths and InGaAs arrays, which does drive down the fluorescence background[176, 177]. However, there also problems associated with this solution, namely, the InGaAs detectors used are noisier than CCD detectors, and so require a longer integration time per signal acquisition, which has negatively affected the introduction of InGaAs arrays into clinical settings.

Alternatively, stimulated Raman spectroscopy (SRS) and Coherent anti-stokes Raman spectroscopy (CARS), are two Raman methodologies that can perform video-rate live-time results by "forcing" the photon to inelastically scatter. Both SRS and CARS are third-order non-linear phenomena. SRS uses two photon frequencies to promote resonance at a particular frequency which corresponds to a vibrational state, where a photon is then emitted. CARS uses 4-wave mixing to generate a photon at the anti-stokes frequency, which is stronger than spontaneous Raman and is far removed from the fluorescent background. Fig 32 shows the Jablonski diagram for these three processes.

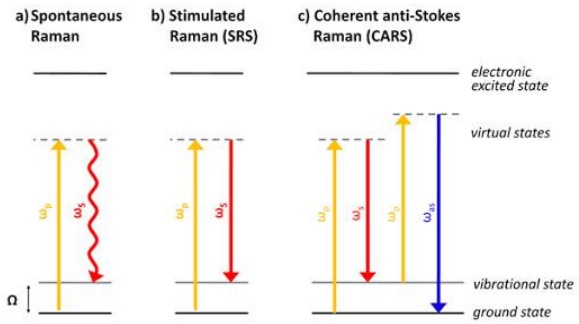

Figure 2-32. Jablonski diagram for spontaneous Raman, SRS(2nd photon in red is driven as opposed to spontaneous) and CARS.

There are many variations of these stimulated techniques which will not be discussed in this section. Some notable works and theories in these fields are offered by [179, 180, 184, 185] and [186-188].

Fluorescence Spectroscopy Techniques

Fluorescent spectroscopy is a popular imaging technique as it can provide a sharp contrast between molecules with an attached active fluorophore from their background. Shining light at a particular frequency can activate either endogenous markers or exogenous markers, which can shed light into the understanding of cell behaviors in cancerous situations[189-191], guide complex brain surgeries[192] in real-time and diagnose cancer in in-vivo settings[189, 193, 194].

Autofluorescence

Autofluorescence is the phenomenon of emission by a molecule due to its endogenous fluorophores. Some common endogenous fluorophores are NADPH, chlorophyll, flavin, and riboflavin, which are fluorescent at different wavelengths

(NADPH absorbs at 340 nm, and fluoresces at 450 nm, chlorophyll absorbs at 665 nm and emits at 726 nm). In Raman spectroscopy of biological tissue, such as in the kidney[178, 195], autofluorescence is a strong effect that can be several magnitudes of intensity more intense than the Raman signal. However, autofluorescence has been used independently by various groups to explore the feasibility of using a 337 nm excitation with fiber optics to diagnose cervical cancer[196] in a clinical setting. The study found that as the tissue progresses from being normal to being cancerous, there is a decrease in fluorescence due to collagen and oxyhemoglobin, and an increase in NAD(P)H. Autofluorescence has also been used in the diagnosis of esophageal cancer[197, 198], bladder cancer[199] and colon cancer [200, 201], to name a few studies.

CHAPTER 3

MONTE-CARLO MODELING OF CONVENTIONAL AND MOBILE PHONE CAMERA BASED TRANSCUTANEOUS BILIRUBINOMETRY IN PIGMENTED INFANTS

Abstract

Newborns in the high-income countries are routinely screened for neonatal jaundice using transcutaneous bilirubinometry (TcB). In sub-Saharan Africa, TcB is not widely adopted due to lack of resources, and mobile phone camera based TcB could help expand screening. Concurrently, studies have reported reduced accuracy of clinical TcB in pigmented infants with elevated bilirubin. GPU-accelerated Monte-Carlo modelling is used to evaluate the combined relationship of pigment and bilirubin on both clinical TcB and mobile-phone approaches to TcB. Results indicate differences in sensitivity to bilirubin concentration based on pigmentation and optical configuration. Model outputs are validated against Mobile phone TcB measurements of optical phantoms. The analysis methods provide guidance for multi-parametric assessment of reflectance in TcB and development of mobile phone TcB.

Introduction

Transcutaneous bilirubinometry (TcB) is a diffuse reflectance (DR) based technique to estimate serum bilirubin concentrations in newborns to screen candidates for treatment for neonatal jaundice [202, 203]. TcB works by measuring reflectance near bilirubin's absorption maxima at 470 nm, and at least one additional reference measurement above 500 nm to normalize for optical variations in tissue such as perfusion or pigmentation [204, 205]. Two or more spatially offset detection pathways can also be used to bias measurement depth-dependence between skin layers, which assist in improving the accuracy of bilirubin estimations [206]. Over the last 20 years, TcB has become an important element of a systematic approach for screening newborns risk for extreme hyperbilirubinemia (EHB) in high-income countries [207-210]. As a result,

appropriate treatments are administered in a timely fashion, and instances of chronic bilirubin encephalopathy (CBE) and EHB related deaths are extremely rare in countries such as the United States [43, 211, 212].

EHB related neonatal mortality and CBE are primarily present only in low- and middle-income countries (LMIC), where adoption of systematic approaches for screening, diagnosis, and therapy is not widespread [213, 214]. While the gold-standard for measurement of bilirubin levels remains total serum bilirubin (TSB), TcB can serve as a valuable surrogate where laboratory facilities or testing reagents have varying degrees of availability, and cost considerations are significant [215-217]. Still, the cost of currently available TcB devices remains an obstacle for their adoption within LMIC as part of standard practice, and as a result, several groups have explored mobile phone-based variants involving use of the mobile phone camera [218-222], with one study reporting correlation vs. TSB similar to more costly clinical TcB devices [223]. At the same time, studies of clinical TcB devices have reported both an overestimation and an increased variability of bilirubin estimates in infants with high levels of pigment and bilirubin [224-227]. This scenario is both more common in LMICs, and more consequential, as inaccuracy can complicate utilization of valuable treatment resources[216].

DR from neonatal skin can be a complicated phenomenon, with a mixture of contributions from scattering and several chromophores, including bilirubin and melanin. Additionally, each chromophore's contribution to measured reflectance varies with mean photon pathlength through each layer of tissue (i.e. epidermis, dermis), which is wavelength dependent. Monte-Carlo (MC) modeling has been a well-suited approach for

theoretical investigation of DR in TcB, providing valuable insights into the influence of pigment, scattering, illumination/collection geometry, and light source selection, all of which have contributed to the evolution of TcB devices [84, 228-230]. However, MC studies have not been reported for the unique configurations of mobile phone-based TcB, nor have published MC studies provide direct insight into clinical reports of inaccuracy in pigmented infants. Part of this challenge can be attributed to the significant computational requirement required for MC studies that simultaneously evaluate the shared effects of varying bilirubin levels, varying infant pigment, and physical TcB device geometry.

Through the advent of readily available GPU parallelizable processing, MC modeling can be performed on a massively accelerated scale in comparison with non-parallelized approaches [231], the ability to study shared relationships between multiple chromophores [89], and a wider variety of illumination/collection configurations simultaneously [35,36][232, 233]. Revisiting MC modeling of TcB can similarly enable a closer study of shared relationships between chromophores and reflectance, as well as TcB configurations that range from typical devices to new mobile phone approaches.

In this manuscript, a GPU-accelerated MC framework is used to explore the combined influence of melanin and bilirubin on DR as measured by clinical TcB, as well as mobile-phone-TcB approaches. The results focus on the effect a combination of higher than average pigment and bilirubin levels have on measured reflectance in order to better understand recent clinical reports [224-227], as well as guide development of mobile-phone TcB. Finally, model outputs of two different mobile-phone TcB configurations are validated with optical phantom measurements.

Monte Carlo Model

The Monte-Carlo model reported here was implemented using the Monte Carlo eXtreme (MCX) platform [89], with the specification of the illumination, detection, and tissue optical properties to model DR as measured in various situations in transcutaneous bilirubinometry. GPU acceleration of the MC model allowed 1e8 photon packets to be launched in each simulation. Each photon packet undergoes progressive attenuation with each individual optical interaction until the termination threshold of 0.5% was reached. Individual simulations were completed in under 10 seconds on a Lenovo ThinkStation P700 PC with an NVIDIA M4000 (1664 cores) graphics card.

Neonatal Skin Model

The overall optical model for neonatal skin is represented as a four-layer medium (Figure 1), largely based on prior work [84]. Each layer is parameterized by its thickness and bulk optical properties (μ_a,μ_s ,g,n). Each layer was set to 30x30 mm in the lateral dimensions with 25x25-μm grid elements, totaling 800 voxels in the lateral plane. Layer thickness was held static, as the focus here is on the combined effects of bilirubin and melanin. The total depth of the tissue volume was 1.5 mm, with 25 μm voxel depth.

The first layer is representative of the epidermal layer in infants; this layer is 50 microns in depth [234] and drove the selection of the 25 μm voxel dimension. The fractional volume of melanin (f_{me}) represents neonates having different skin pigmentation. The relation between fme and the absorption in the epidermal layer is:

$$\mu_{a_{epi}}(\lambda) = f_{me}\mu_{a_{me}}(\lambda) \quad (3\text{-}1)$$

The term $\mu_{a_{me}}$ is an approximation of melanosomes absorption in the epidermal layer as a function of the wavelength [235]. Melanin is assumed to be the only absorbing agent in the epidermal layer, and the absorption is a combination of the fractional volume of melanin and the absorption coefficient of melanin. In darkly pigmented neonates, the maximum melanin fractional volume was set to 10% [236].

The reduced scattering coefficient for both the epidermis and dermis was calculated analytically as a function of wavelength [237], as was the anisotropy factor [238]. While scattering can vary substantially in tissue and is also dependent on gestational age [57], it was not varied here since the focus was on bilirubin and melanin.

The second layer is 900 μm thick and represents the dermis of the infant. In this layer, there are two main absorbers: hemoglobin (oxy- and deoxygenated) and bilirubin. The absorption coefficient for bilirubin can be presented as a function of wavelength:

$$\mu_{a_{Bi}}(\lambda) = 2.3026 \frac{[Bi]}{P_{MBi}} \varepsilon_{Bi}(\lambda) \tag{3-2}$$

Where [Bi] is the concentration of bilirubin in g/L, $PMbi$ is the gram molecular weight of bilirubin and ϵbi is the extinction coefficient of bilirubin in $cm{-}1/M$. The absorption coefficient for hemoglobin in the dermis is a mixture of oxy- and de-oxygenated hemoglobin:

$$\mu_{a_{bl}}(\lambda) = S\mu_{a_{oxy}} + (1 - S)\mu_{a_{de-oxy}} \tag{3-3}$$

Where S is the oxygen saturation rate of the infant, assumed to be 93% for all subsequent simulations [239] and the μa for oxy and de-oxygenated blood are determined in a similar manner to bilirubin from the extinction coefficients [48]. The overall μa for the dermis is a sum of the weighed mean of individual products of hemoglobin and bilirubin absorbance and blood and bilirubin volume fraction (Vhb, Vbi) from:

$$\mu_{a_{dermis}}(\lambda) = V_{Hb}\mu_{a_{Hb}}(\lambda) + V_{Bi}\mu_{a_{bi}}(\lambda) \quad (3\text{-}4)$$

The third layer, the hypodermis, is 300 microns thick in neonates so that the sums of the epidermis, dermis and hypodermis depth are equivalent total skin thickness in neonates [240]. The optical parameters for the third layer ranged from 0.13 to 0.07 $mm{-}1$ for μ_a [241] and 3.94 to 2.48 $mm{-}1$ for μ_s[51]. The anisotropy factor g and refractive index n were statically set to 0.8 and 1.44 respectively across the spectral range.

The fourth layer was of the skull/bone structure underneath the skin, with μa set to 0.0096 [242] and μs from [41]. The anisotropy factor g and refractive index n were statically set to 0.89 and 1.5, respectively.

The effect on modeled DR was studied as a function of variations in [Bi], f_{me}, Vhb, and wavelength. f_{me}varied from 0 to 10% with a 1%increment, with melanin volume fraction's greater than 3% being representative of infants of African origin [236]. The [Bi] was varied from 0 to 25 mg/dL in 1 mg/dL increments, where concentrations above 10 mg/dL can be loosely considered jaundiced, and concentrations above 20 mg/dL can be considered severely jaundiced [243]. The Vhb was varied from 0% to 2% in 0.5% increments, with variations practically arising from the amount of pressure device operators may apply when making contact measurements. Comprehensive simulations for all combinations of chromophore concentration/volume fraction were performed from 470 to 650 nm in 10 nm increments, resulting in a 4-dimensional data set of DR vs variations in bilirubin, hemoglobin, melanin, and wavelength.

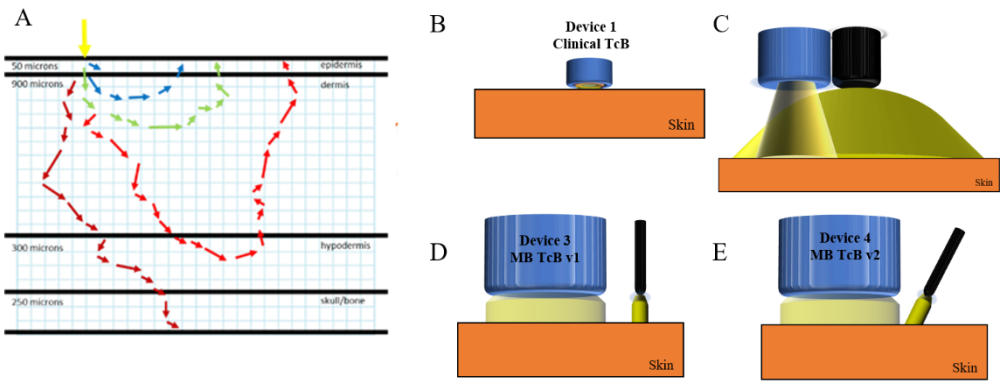

Figure 3-1. MCX Tissue and Device Configuration.

(A)Four-layer tissue model implemented for all simulations. Colored arrows illustrate wavelength-dependent optical paths. (BE)Device configurations. (B) Dräeger JM-103 clinical TcB, (C) Mobile phone camera 5 cm from skin surface, (D) Mobile phone TcB with confined illumination at 0° to normal,and (E) mobile phone TcB with confined illumination at 30° to normal.Black illumination source, Blue-virtual detector

Physical Bilirubinometer Model

Models for 4 different TcB device configurations were reproduced based on their photon launch functions and detector geometries. Conceptual illustrations are shown in Figure 3-1,B-E, with detailed specifications below. Modeled reflectance is captured based on photons that pass through each devices appropriately positioned virtual detector in the model space.

Device 1 was made to resemble one of the most common TcB devices, the Dräeger JM-103 [244], which has a donut-shaped illumination ring with an inner radius of 1.33 mm and an outer radius of 1.78 mm, and a pair of detectors which collect two different optical paths. The short-pathlength, epidermis-biased, detector was placed inside the illumination ring, with a 1.15 mm radius. The long-pathlength, dermis-biased detector

was placed outside the illumination ring, with inner and outer radii of 2.08 and 2.99 mm, respectively.

Device 2 represented simple mobile phone photography of neonatal skin at a distance of 5 cm, with the mobile phone camera flash providing uniform illumination over the skin's surface, and the detection scheme configured to correspond with typical mobile phone f/# of 2.4 and field-of-view of 59.15◦.

Device 3 and Device 4 modeled a DR approach using a spatially confined illumination which was offset from detection, near the skin surface. These configurations represent a simple, inexpensive compromise between device 1 and device 2, by incorporating the spatially confined illumination and offset characteristic to clinical TcB (Device 1) with the mobile phone camera illumination and detection(Device2). In both devices 3 and 4, the detector simulated measurement 10 mm above the skin with a radius of 7 mm, and f/# of 2.4, with illumination-detector offset of 10.45 mm. In device 3, illumination was a 2 mm disc, orthogonal to the skin, while in device 4 the illumination angle was 30° to the normal of the skin.

Model Analysis Method

Each photon packet carries information related to its trajectory (position and direction) and pathlength (Δx) through the tissue model. Only photon packets whose position and direction are within the acceptance parameters of the virtual detector are recorded. The collection efficiency of the device (η) is defined as the ratio of the number of detected photon packets to the total number of photon packets launched, ($\eta = N_{detected}/N_{total}$), and must be accounted for in determination of total detected reflectance ($R_{detected}$),

which is calculated through Beer-Lambert's law and the optical properties of each layer as defined in the tissue model.

$$R_{Detected} = \eta W_0 \prod_{layer=1}^{n} R_{layer} = \eta W_0 \prod_{layer=1}^{n} e^{-\mu_{a,layer}\Delta x_{layer}} \quad (3\text{-}5)$$

Where W_0 represents the weight of each photon packet as it enters the tissue model, after accounting for specular reflectance at the tissue surface, and R_{layer} represents a contribution to the total reflectance from each layer. The weight of the photon packet after having interacted with each layer is attenuated accounting for the pathlength traversed in each layer of the tissue model (Δx_{layer}) and the absorption coefficient of each layer ($\mu_{a_{layer}}$). The total detected reflectance is then the product of the reflectance in each layer [89]. Additional insight into simulations of DR can be gained by parsing each individual layer's contribution to the total attenuation via the layer-dependent pathlength output, Δx_{layer}. The layer-dependent attenuation of layer i (A_{layer_i}) was defined as,

$$A_{Layer_i} = \frac{\mu_{a,layer_i}\Delta x_{layer_i}}{\sum_{layer=1}^{n} \mu_{a,layer}\Delta x_{layer}} \quad (3\text{-}6)$$

Where the summation in the denominator of (3-6) represents the total attenuation, which mathematically derives from product of the exponential terms in equation for total detected reflectance (eqn 3-5).

Tissue Optical Phantoms

Simple validation of the Monte-Carlo model was performed through mobile phone reflectance measurements of polydimethylsiloxane (Sylgard® 184 Silicone Elastomer DOW/Corning) optical phantoms [245] with embedded scattering and

absorptive elements. The selection of PDMS and the specific chromophores was based on achieving stable shelf-life and producing optical properties that mimicked tissue chromophores. Yellow dye 6 was selected as a shelf-stable analog of bilirubin as they both are characterized by absorption maxima near 470 nm, with minimal absorption above 525 nm [246] . Dissolved instant grind coffee crystals (Folgers Classic Roast® Instant Coffee Crystals) were selected as stable analogs of melanin [247]. $TiO2$ (2.5 mMol/mL) was incorporated into the PDMS to provide scattering [248, 249]. Yellow dye 6 and coffee were added to separate PDMS mixtures, which after curing, resulted homogeneous, single-chromophore layers to individually mimic dermis and epidermis, respectively. Yellow 6 phantoms were cast in individual 25x25x1 mm custom 3D printed molds, which served as both simple single layer phantoms for initial validation of the MCX model and mobile phone measurement of DR, as well as a tissue model approximation of the dermis in dual-layer phantom experiments. Dual-layer phantoms were created by casting a coffee layer directly atop of the Yellow 6 layer, using a single 60 micron thick adhesive tape (Scotch® Magic™ Tape) as the cast negative. The mixtures were degassed for 30 minutes and placed into an oven at 80° C for 4 hours. Single-layer phantoms were created with constant $TiO2$ concentration and yellow dye 6 concentrations varying from 1.7e-7 to 4.1e-7 mol/mL in 0.3e-7 mol/mL increments. Hemoglobin was not included as this study focuses on the relationship of bilirubin and melanin.

The optical properties of the phantoms were retrieved using an integrating sphere (IS) (IS200, Thorlabs) and a white LED light source (CWHLP1, Thorlabs) coupled through a 0.39 NA 400 micron fiber (M92L01, Thorlabs). The outgoing tip of the fiber

was collimated with a lens (LA1131, Thorlabs). Calibration of the IS was done with a 99% reflectance standard (SRS-99-010, Labsphere). Optical properties were determined from the measured reflectance and transmittance using inverse adding doubling software(IAD)[250-252].

2.3. Mobile Phone Adaptation and Reflectance Measurement

Mobile phone reflectance measurements were obtained using the onboard camera and LED flash of a Nexus 5 (LG Nexus 5) Android smartphone. A rapid prototyped (Connex 3 Object 500 3D printer, Stratsys Ltd.) adaptor printed in black material (Vero Black, Stratsys Ltd.) was fitted to a generic snap-on protective phone case, and aligned over the camera and flash. The adaptor design masked the flash, directing and spatially confining the illumination. The adaptor also housed a 470 nm bandpass filter (FB-470-10, Thorlabs) infront of the camera to spectrally resolve detection. Two adapters were fabricated to match the specifications described above for modeled Devices 3 and 4. Uncompressed images from the camera were converted into Digital Negative (.dng) format (Adobe DNG Converter) in order to avoid information loss through compression. All subsequent analysis is performed in MATLAB (Mathworks). DNG images are demosaiced [253] resulting in RGB images with spectral components primarily defined by the optical filters spectral response. The exposure time on the cell phone was set to 200 ms, the focus set to infinity and light sensitivity (ISO setting) set to 1,000. All images were taken five times and averaged to reduce noise. Dark images were taken with the flash off and the camera aperture blocked, and the averaged result was then subtracted from sample images to produce measured DR. In order to confirm appropriate

implementation of the model platform here, measurements of optical phantoms with pre-determined optical properties were compared against corresponding modeled estimates.

Results

Appropriate mobile phone camera measurement of reflectance model and implementation of the MCX model was validated through comparison of empirical measurements of single-layer phantoms with varying concentrations of yellow 6 dye against corresponding model outputs (Figure 3-2). Characterization of the phantoms with IS measurements and IAD resulted in absorption coefficients ranging from 0.2 to 0.9 mm-1, which spans a range similar to reported absorption coefficients of bilirubin in neonates [60]. Use of these optical properties in MCX resulted in modeled blue channel reflectance that correlated well with empirically measured reflectance (R^2=0.96).

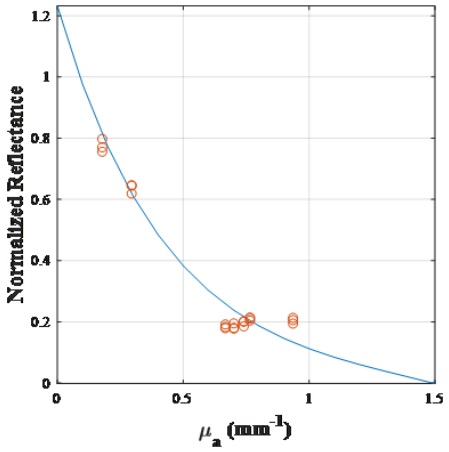

Figure 3-2. Simulated MC results

Simulated MC results (blue line) and experimentally captured blue channel reflectance (orange dots) for single-layered phantoms using mobile phone device 3.

In order to demonstrate the well-understood basis of optical measurements from neonatal skin, MCX modeled DR in the blue, green, and red color channels is plotted as one chromophore concentration is varied across the physiological range while the other two are held fixed (Figure 3-3). Changes in [Bi] only affect the blue channel (Figure 3-3 A-C). However blue channel reflectance is also affected by both changes in Vhb and fme (Figure 3-3 D,G). In this instance (mobile phone device 3), it is notable that an increase in [Bi] from 0 to 25 mg/dL results in a 8.4% decrease in blue spectral channel reflectance, while a change in fme from 0 to 10% produces a larger 13% change, which highlights the significance of skin pigment's influence. Red channel measurements offer an opportunity to correct for melanin, with variation independent of [Bi] and Vhb (Figure 3-3 C,F,I). Simulations were performed for all combinations of chromophore levels, and required 9 min to generate in total, with Figure 3-3 only showing a portion of the results for simplicity.

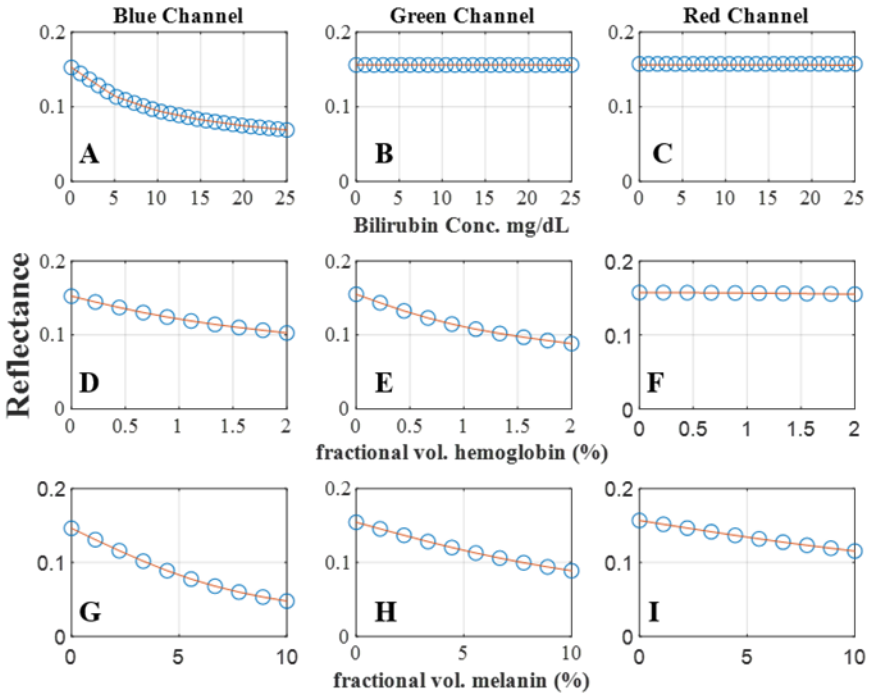

Figure 3-3. Modeled spectral reflectance vs. tissue chromophore concentration for mobile phone bilirubinometer device 3.

Modeled reflectances are depicted for specific spectral channels (columns: Blue=470nm, Green=550nm, Red=650nm). Rows depict the influence of changes in individual chromophore levels for bilirubin (top row), hemoglobin (middle row), and melanin (bottom row). In each row, non-varying chromophores are fixed at the center of the modeled range(Bilirubin: 12.5 mg/dL, Melanin: 5%, Hemoglobin: 1%).

The modeled reflectance as a function of both melanin and bilirubin levels in the blue channel (470 nm) for Device 1 (Clinical TcB) is shown in Figure 3-4A. The flatest gradient in DR exists at high melanin/high bilirubin levels, in comparison with a much steeper gradient at low melanin/low bilirubin levels. The influence of pigment is more clear in Figure 3-4B, where signals are 19% lower across all [Bi] levels for darkly pigmented infants. Finally, Figure 3-4C depicts the reflectance sensitivity vs. bilirubin (dR/d[Bi]), and shows a decrease as [Bi] increases. In addition, Figure 4C shows reflectance sensitivity to [Bi] is decreased in pigmented infants.

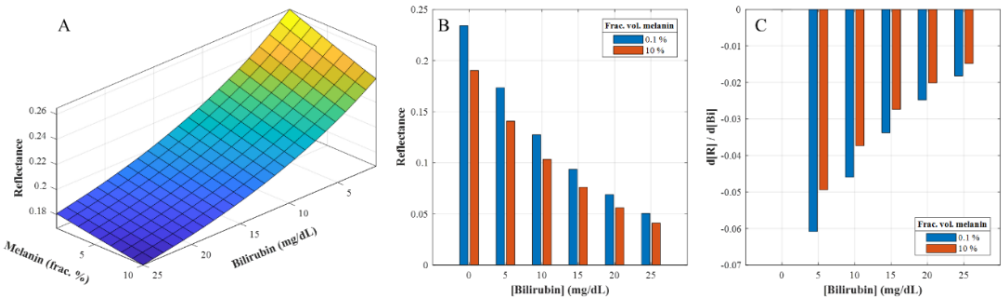

Figure 3-4. Blue channel reflectance (470 nm) for Device 1 (Clinical TcB) vs. bilirubin and melanin (A).

Comparison of reflectance vs [Bi] for both low (0.1%, red) and high (10%, blue) f_{me} infants (B). Reflectance sensitivity (dR/d[Bi]) vs [Bi] for low and high f_{me} infants (C).

A comparison of changes in modeled reflectance and reflectance sensitivity to bilirubin across the 4 modeled devices is shown in Figure 3-5. Device 1 (Clinical TcB) captures more reflectance (Figure 3-5A), and has a greater sensitivity vs. [Bi] (Figure 3-5B) in comparison to Devices 2-4 (mobile phone based TcB). Note that while the rank order of mobile phone devices reflectance intensity changes above/below [Bi] = 15mg/dL (Figure 3-5A), Device 4 consistently demonstrates higher reflectance sensitivity to bilirubin (Figure 3-5B).

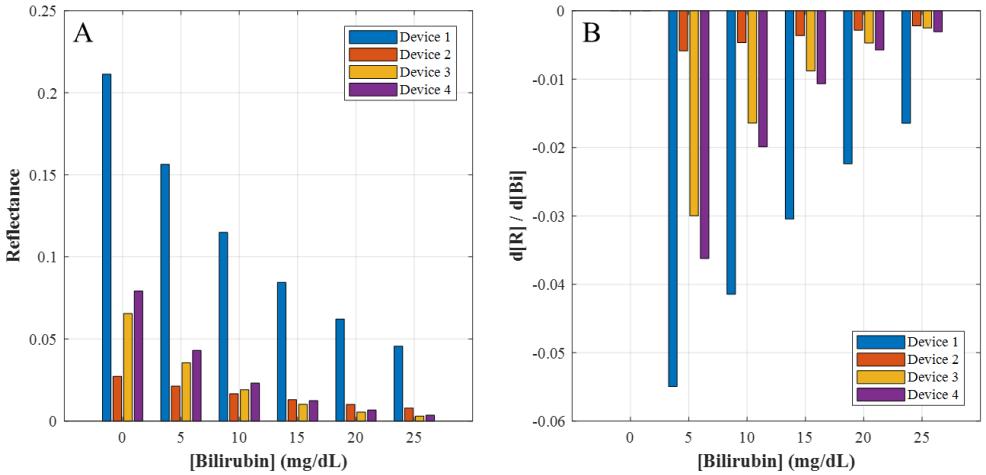

Figure 3-5. MC model comparison of TcB device designs for a clinical TcB

MC model comparison of TcB device designs for a clinical TcB (Device 1) and 3 different approaches to mobile phone TcB (Device 2-4). Blue channel (470 nm) reflectance intensity (A) and reflectance sensitivity (B) across the physiological range of bilirubin. f_{me} = 5%, V_{hb} =1%.

Further insight beyond the total modeled reflectance signal can be obtained through examination of layer-dependent attenuation ($A_{layer i}$,eqn 3-6). Figure 3-6A depicts blue channel A_{dermis} and $A_{epidermis}$ for the clinical TcB (Device 1). A_{dermis} is greater than $A_{epidermis}$, and clearly separate from $A_{epidermis}$ for all combinations of [Bi] and f_{me}. In comparison, A_{dermis} in Device 2 is not always greater than the $A_{epidermis}$(Figure 3-6B). This is also the case for the other mobile phone devices (Device 3& 4, data not shown). An alternative representation of the differences between the devices is the ratio of $A_{dermis}/A_{epidermis}$, which is shown in Figure 3-6C. $A_{dermis}/A_{epidermis}$ increases as [Bi] increases. Again, it is evident that the Device 1 (clinical TcB) is superior to mobile phone based techniques, but also that variations in mobile phone TcB configuration can influence $A_{dermis}/A_{epidermis}$. For Device 2 $A_{dermis}/A_{epidermis}$> 1 for [Bi] above 12.5 mg/dL, reaching a maximum of 2.08 at [Bi] = 25mg/dL. For Device 4 $A_{dermis}/A_{epidermis}$> 1 for [Bi] above 6.5 mg/dL, reaching a maximum of 3.

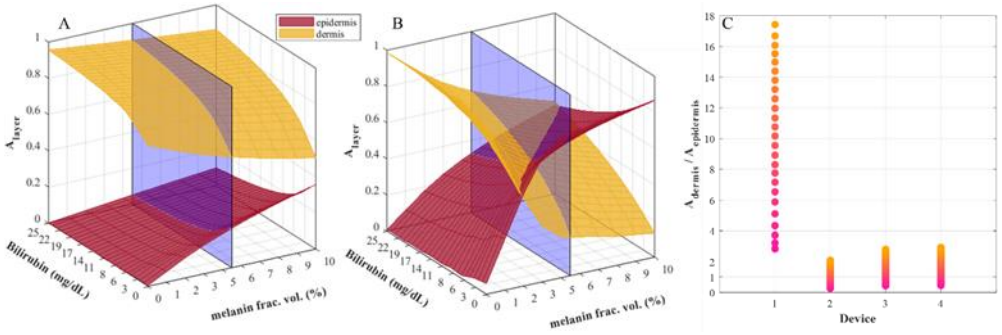

Figure 3-6. Blue channel layer dependent attenuation,

Blue channel layer dependent attenuation,A_{layer}, for epidermis and dermis for a clinical TcB (A, Device 1) and a mobile-phone device (B, Device 2). The blue plane in (A) and (B) indicates f_{me} = 5%. Comparison of all devices $A_{dermis}/A_{epidermis}$, with f_{me} = 5% over the range of [Bi](C). Color of dots in (C) ranges from [Bi] = 0 mg/dL (pink) to [Bi] = 25 mg/dL (yellow).

Finally, MCX models of mobile phone DR from Device 3 (0° illumination) and Device 4 (30° illumination) were validated against measurements from dual-layer phantoms with 4 neonatal skin models. Figure 3-7A depicts MCX results with high and low levels of bilirubin (5,20 mg/dL respectively) and melanin(1,5% respectively), with the A_{layer} of epidermis, dermis, and other layers (sub-dermis and bone) overlaid. Low melanin levels result in reflectance measurements dominated by contributions from the dermis, while high melanin levels result in decreased overall reflectance and a decrease in relative contribution from the dermis. In all instances, device 4 offers increased reflectance. Figure 3-7B depicts empirical measurements of dual-layered phantoms using mobile phone devices 3 and 4. Low and high bilirubin levels were approximated with yellow-6 phantom layers with μ_a of 0.40 and 0.90 mm^{-1}, respectively. Low and high melanin levels were approximated with coffee phantom layers with μ_a of 0.05 and 0.20 mm^{-1}, respectively. Phantom layer μ_a were individually determined with IS-IAD. Similar trends seen between Figure 3-7A & B validate the MCX models results.

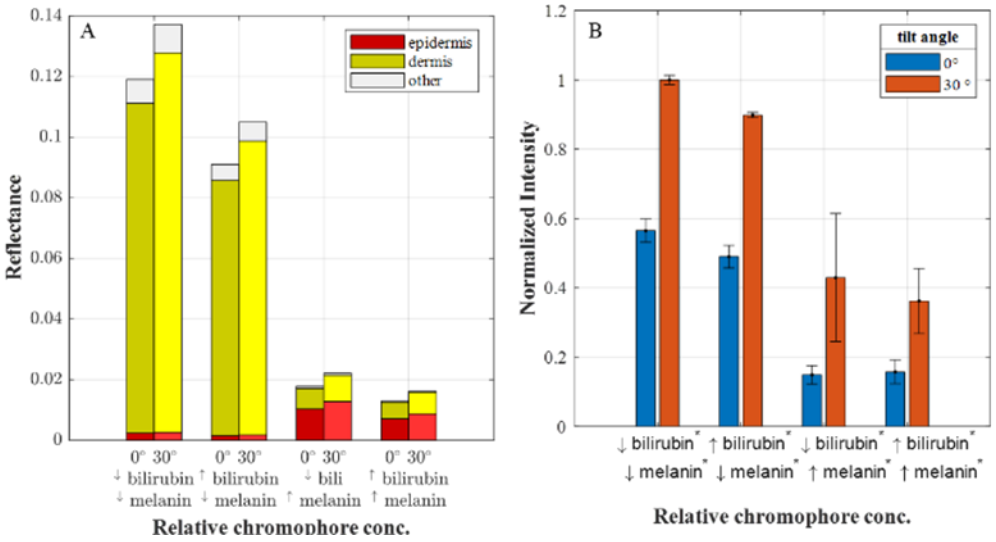

Figure 3-7. Blue channel reflectance modeled

in neonatal skin(A) and experimentally measured from dual-layer phantoms (B) for mobile phone Device 3 (0° illumination) and Device 4 (30° illumination). Modeled reflectance bar plots are divided into attenuation contributions from epidermis (red) and dermis (yellow), and all other layers(grey). Low and high bilirubin and melanin in (B) were mimicked with yellow dye 6 and coffee, respectively.

Discussion

TcB is currently a critical element within a broader systematic approach for the management of neonatal jaundice in high-income countries, and adoption of similar paradigms in subSaharan Africa and South-Asia would be a straightforward path to reducing disparities in outcomes [213, 214, 243]. However, reports of systematic overestimation and decreased accuracy in pigmented infants, particularly those with bilirubin levels above 20mg/dL [224-227], tempers the enthusiasm for TcB's adoption, because treatment resources can be scarce, and their inefficient utilization would be problematic [216]. This manuscript focuses on the theoretical differences between the primary spectral measure of bilirubin (blue channel reflectance), which is , as multiple parameters are varied, including not only pigmentation and bilirubin, but also device configuration. Ideally, a low-cost, mobile-phone based approach to TcB could be developed to expand access to screening, however adaptation of a technology designed for imaging to perform TcB must consider the critical issues recently brought to focus from these important clinical studies [216, 224-227].

While the theoretical basis for TcB is well developed and has been previously investigated through conventional MC modeling and phantom studies [84, 228, 230, 254], the implementation of the powerful GPU-parallelized MCX platform [89] is valuable because it expedites multiparametric modelling across physiological variations

in tissue properties and multiple TcB devices. An important initial step was basic validation of MCX derived simulations of reflectance against mobile phone reflectance measurements(Figure 3-2). Additional evaluation of the model was performed by varying bilirubin, hemoglobin, and melanin over their physiological ranges (Figure 3-3), and confirming the outputs support previously modeled [84, 230, 254], well-understood, phenomena in TcB such as bilirubin, melanin, and hemoglobin's contribution to blue channel reflectance and the independence of red channel measurements from changes in [Bi] and V_{hb}.

Clinical studies of commercial TcB conducted on exclusively pigmented infants of African and South-Asian origin have reported a systematic overestimation of bilirubin levels, along with decreased accuracy at high bilirubin levels (i.e. > 20 mg/dL) [224, 255]. The decreased reflectance in darkly pigmented infants vs. lightly pigmented infants (Figure 3-4B) indicates that if the blue spectral channel is used without correction for pigmentation, it can be expected that pigmented infants bilirubin estimates are higher than less-pigmented infants. Clinical TcB devices are known to incorporate additional spectral channels for correction [204], however, if the methods do not fully correct for pigmentation, or the regression models are built on multi-ethnic or primarily lightly pigmented infants, Figure 3-4B suggests underestimation is not unexpected. Moreover, the decrease in the gradient of the reflectance curve at high-bilirubin/high-pigment levels (Figure 3-4A) suggests an increased susceptibility of [Bi] estimation error that could result from limited dynamic range, measurement noise, and/or reflectance variability due to factors not modeled in this study, such as tissue scattering. This is also seen in Figure 3-4C, which shows a decreased reflectance sensitivity (dR/d[Bi]) as bilirubin levels

increase, with further reduction in sensitivity observed in darkly pigmented infants vs light pigmented. Taken together, these results reinforce previous modelling work [84, 254] and clinical studies [234] which suggest pigmentation's fundamentally confounding role in TcB, while also further highlighting the additional theoretical difficulty that accurate [Bi] estimation presents in highly jaundiced, darkly pigmented infants.

Mobile-phone TcB devices [219-223] could expand accessibility to screening in low-resource settings, however their design should consider high-pigment, high-bilirubin infants based on potential use-case scenarios.In addition, mobile phone based approaches for TcB should be simple in design and require minimal modifications.The results from Figure 3-5 demonstrate the superior capability of a clinical device vs. three different mobile phone TcB devices in capturing DR, as well as the superior sensitivity to changes in [Bi] across the modeled range of [Bi] in pigmented (i.e f_{me} = 5%) infants. Device 2 is the most straightforward mobile phone approach, simply quantifying reflectance with a close-up photo (Figure 3-1 C), while devices 3 & 4 (Figure 3-1D,E) incorporate spatially offset and confined illumination to emphasize measurement of DR, as is the case in the clinical TcB device. Device 4 further reduces the illumination-detection spatial offset and imparts an oblique illumination with the intention of confining photon interactions with superficial layers of the skin. Differences between the mobile phone devices emphasize the influence of illumination and collection geometry. As noted above, the sensitivity (dR/d[Bi]), can be considered a better measure of resilience to elements of variability, including noise, in comparison to reflectance. Figure 3-5B indicates the superior sensitivity of Device 4 in comparison with other mobile phone devices, across all [Bi].

Monte-Carlo modelling's value also includes theoretical insight into parameters such as layer-dependent attenuation, which cannot be directly observed from empirical measurements. Ideally, attenuation of blue channel measurements in TcB would primarily result from optical interactions occurring in the dermis instead of the epidermis in order to minimize the influence of melanin. This is the case for the clinical device (Figure 3-6A), which demonstrates higher dermal attenuation with a fairly uniform gradient, particularly at [Bi] >12.5 mg/dL. It is notable that the relative amount of layer dependent attenuation can vary substantially with [Bi] and f_{me} depending on illumination/collection geometry, as is seen in comparing the differences between Figure 3-6A and B(Device 2). A scenario in which epidermal attenuation is greater than dermal attenuation suggests the increased importance of spectral correction of chromophore concentration. Also, when layer dependent attenuation vs. chromophore concentration is characterized by a steep gradient, as is the case in all mobile phone devices, creation of regression models based on infants with a more narrow range of pigment variations will be more important to consider if robust melanin correction is not performed. With respect to the ratio of $A_{dermis}/A_{epidermis}$ for different [Bi] (Figure 3-6C), the differences between mobile phone devices again point to a subtle advantage for Device 4. While the challenge of accurate bilirubin estimation in pigmented infants with [Bi] > 12.5 mg/dL is rooted in fundamental tissue optics, evaluation of the MCX model derived outputs, including reflectance sensitivity (Figure 3-4C and 5B) and layer-dependent attenuation (Figure 3- 6, 7A), for different mobile phone TcB devices can help provide theoretical insight to guide design and minimize estimation error.

MCX results suggesting the superior performance of Device 4 over Device 3 in Figures 3-5 and 6 were empirically supported by measurements performed with devices on dual layer phantoms with chromophores that mimicked bilirubin and hemoglobin. The mobile phones were fitted with simple adaptors over the camera and flash module in order to perform spatially offset DR measurements. The differences between the two devices as seen in the models followed a clear trend supporting the benefit of reducing spatial offset and imparting oblique illumination.These benefits were also seen in empirical measurements (Figure 3-7B). One of the primary objectives of this manuscript was to utilize MCX modelling to evaluate the potential feasibility and perform comparative analysis of potential designs for mobile phone based TcB. While it is clear that the design of device 4 is preferred, it is also evident that the mobile phone designs evaluated here suffer from inferior sensitivity to [Bi] estimation in comparison with the clinical device (Device 1), and also are characterized by greater influence from melanin in the blue spectral channel. This primarily seems to be the result of illumination/collection geometry factors in which the annular illumination and collection of the clinical TcB device is both more efficient and better suited to capture pathlength dependent differences in optical attenuation. This is particularly important in TcB, where blue channel measurements that are fundamentally superficially biased, and thus more vulnerable to influence from melanin, must estimate the bilirubin resident in the underlying dermis. While this phenomena has been reported [84, 228, 230, 238, 254], the power of MCX implementation of a model of neonatal skin is that it simultaneously enables evaluation of the influence of paired variations in melanin-bilirubin chromophore

concentrations in addition to comparison of multiple specific illumination/collection geometries for design guidance.

The general approach to implementation of the tissue model here was sharply focused on the relationship between bilirubin and melanin on reflectance in the blue channel. However, the power of the MCX framework is its speed and capability of generating large volumes of data in short order. A number of other factors certainly play a significant role in real-world measurement of TcB. Optical scattering was fixed in each layer in this study, but is known to vary significantly in infants [84, 228, 230] and can play a substantial role in the variation of measured optical signals. Moreover, scattering is known to progressively increase as a function of gestational age [57] and epidermal thickness [228, 230, 254]. The MCX framework is well suited to conduct theoretical studies that more closely inspect the the influence of factors such as prematurity on TcB measurements.

Conclusion

GPU-accelerated Monte Carlo simulations were performed to compare the shared influence of bilirubin and melanin in clinical TcB and mobile phone approaches to TcB. The differences between blue-channel spectral reflectance in darkly and lightly pigmented infants was modeled, and confirmed the theoretical basis for overestimation and decreased accuracy at high bilirubin levels. A comparison of mobile phone approaches to TcB, with an emphasis on evaluating performance in high-pigment, high-bilirubin infants, indicated the strengths and weaknesses of these devices. Of the modeled mobile phone configurations, that with the smallest illumination detection offset and oblique illumination aided in recovering a more sensitive response to bilirubin, with more

of the signal arising from the dermis. The modelling approach reported here suggests a pathway for developing a low-cost device designed for screening pigmented infants.

CHAPTER 4 A COMPUTATIONALLY EFFICIENT MONTE CARLO MODEL FOR BIOMEDICAL RAMAN SPECTROSCOPY

Abstract

Monte Carlo (MC) modeling is a valuable tool for fundamental understanding of light-tissue interactions, guiding and evaluating optical design, and analyzing empirically measured data. Important considerations for MC models to guide development of biomedical Raman spectroscopy (RS) include the ability to simulate full spectra, the incorporation of background autofluorescence, which can often complicate in vivo measurements, and finally practical considerations such as speed and flexibility in implementation. Here, a MC model for RS is developed atop the open source GPU-parallelized MCX framework, and additionally reports the development of a computationally efficient statistical approach for emission photon generation. The MC model produces a complete Raman and fluorescence spectrum over a 161 point spectral range in 22 minutes. A comparison of modeled vs experimental spectra collected from gelatin phantoms is reported to validate model capability.

Introduction

Monte Carlo (MC) modeling is widely considered the gold-standard in theoretical investigation of light-tissue interactions[107]. Conventional approaches to MC modelling were computationally consuming, however acceleration of MC Modelling using techniques such as Graphical Processing Unit (GPU) parrallelization and distributed computing has dramatically expanded computational capacity[89, 231]. GPU-parallelization has resulted in MC modelling's continued contribution to recent advances in biomedical applications of photonics through expanded understanding of light-tissue interactions, design of complex optical configurations, and evolution's in data analysis[107], and has promising clinical applications in the breast, skin, brain, and

bone[14, 93, 159, 256, 257]. MC modelling of RS has previously been used to contribute theoretical knowledge of RS in tissues[102, 103], guide fiber optic probe design[97, 106], and advance the development spatially-offset RS[102, 183].

MC modeling of Raman scattering is challenging due the rare nature of it's occurrence in comparison with elastic scattering. Previous MC models (MC) of Raman scattering have been implemented using two different approaches; single-photon tracking[98-100, 102, 104, 105] and two-step methods[103]. In single photon tracking models, excitation photons are converted to Raman photons based on a hard-coded Raman conversion probability in relation to elastic scatter, and thus meaningful outputs require either an impractically large number of excitation photons, or an inappropriately large probability of Raman conversion[258]. Alternatively, in the two-step approach, an excitation distribution is first simulated, followed by an emission simulation at each voxel within the tissue model. The model output is then calculated as the sum of the convolution of the excitation distribution with all emission simulations. The two-step approach is less vulnerable to statistical noise from insufficient excitation photons and does not require a hard-coded probability of Raman conversion, however the number of computationally expensive convolution operations scales with the dimensionality of the tissue grid. Previous MC models of RS have been primarily implemented atop a sequential MC platform[98, 102-105] with limited computational throughput. Recently, a parallelized approach to RS MC has been implemented using the two-step method[259].

In a number of instances, the clinical potential of RS is based on multivariate statistical classification from on a multitude of spectral features[260], and therefore MC models of RS would ideally simulate a wide spectral range to guide translation. In

addition, empirical measurements of spontaneous Raman scattering in tissues are acquired in competition with corresponding autofluorescence background signals[169], which can significantly impact measurement signal-to-noise ratio, and also represent an important consideration for MC models of RS intended to inform clinical translation[176, 177, 260, 261]. Modeling the full spectral fingerprint for both Raman and Fluorescence thus would benefit from a platform for MC modeling with an expanded computational overhead.

Here, an MC approach for RS was developed atop the open source parallelized MCX platform[89]. In particular, the approach reported here utilizes a novel, computationally efficient, function called "isoweight", which performs conversion of excitation photons to emission photons by taking into account the relative flux of the excitation distribution. The computational throughput of the model is demonstrated by generation of full-fingerprint Raman spectra as well as the corresponding fluorescence background. Model outputs are validated against empirical measurements of phantoms with turbidity and fluorescence similar to human tissues.

Materials & Methods

Development of Raman and Fluorescence MC Model

The MC model reported here is developed (Microsoft Visual Studio 2017) atop the open-source MCX (Monte Carlo Extreme) base[89], and the C++ mexFunction was compiled using mexcuda on MATLAB 2017b to make the modified compiled MCX compatible with MATLAB. All simulations were performed on a LENOVO P700 Workstation PC with an NVIDIA Quadro M4000 graphics card and CUDA 8.0 (Nvidia

Co.). shows. The overall algorithm flowchart of MC model reported here is shown in Figure 1 .

MCX Generation of Excitation Distribution

The initial step in the algorithm is to directly utilize MCX to generate the distribution of the excitation photons within the tissue model. Briefly, a 3D cubic voxel model of the tissue is generated where optical properties (μ_a, μ_s, g, n) are assigned to represent each voxel in the system. In addition, each voxel in the tissue model is also characterized by a Raman($\kappa_R(\lambda)$) and Fluorescence($\kappa_F(\lambda)$) coefficient, which are not utilized in the generation of the excitation distribution, and discussed in more detail in the next subsection. MCX allows the illumination to be defined from a wide range of preset choices representative of typical physical light sources, and arbitrarily placed with respect to the tissue model. The number of photons launched is specified, as well as other parameters such as allowing specular reflection at external and internal boundaries, minimum energy before photon termination, and the detector positions and radii. These configurations are saved to a global memory cache accessible by the GPU, and the photons are ported over to the GPU side and allowed to propagate through the medium until reaching the termination threshold. The resulting map of photon flux within the 3D tissue model represents the excitation distribution (Figure 2 a).

Generation of Raman Scattering and Fluorescence

A custom launch function was implemented in MCX that isotropically launches either Raman scattered or fluorescent photons from within the tissue volume, weighed by the magnitude of the 3D excitation distribution flux, and is hereby defined as the

"isoweight" launch function. The previously generated 3D excitation flux distribution(2 a) is volume flattened into an indexed 1D excitation flux vector, where each index corresponds to a specific voxel within the 3D volume. The 1D excitation flux is then cumulatively summed and normalized, 0 to 1 inclusive(2 b). The normalized cumulative flux vs. volume index is then inverted, becoming a discrete distribution (2 c). A randomly generated uniform value samples the inverse normalized cumulative flux to identify the nearest (without being larger) corresponding the volume index from which to launch the new emission photon. When dealing with multi-labeled tissue volumes, the emission distribution is split into its labels so that if 60% of the excitation flux occurred in label 1 and 35% in label 2, then 60% of the emission photons will be launched through the 1st label and 35% of the photons are launched from label 2, efficiently using the user set number of photons. The excitation distribution is set to be 0 for all labels except the current, and the "isoweight" function is run on this modified excitation distribution on a per-label basis.

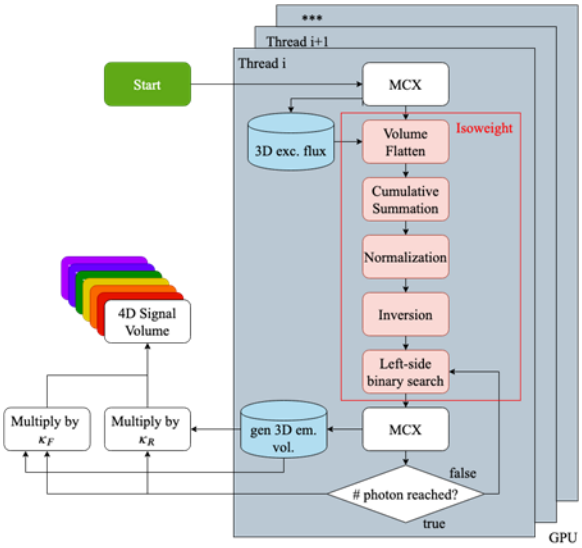

Figure 4-1. Flowchart depicting (a)The pipeline for running the RS MC model.

Flowchart depicting (a)The pipeline for running the RS MC model. Illumination photons are propagated through the standard MCX to generate a 3D excitation flux distribution. The excitation distribution informs the Isoweight figure (2), which generates emission photons that are then propagated through MCX to create a generalized emission distribution. The emission distribution is multiplied by separate Raman($\kappa_R(\lambda)$) and Fluorescence($\kappa_F(\lambda)$) coefficients, resulting in the final model output. (b) illustrates the informing of $\kappa_R(\lambda)$ and $\kappa_F(\lambda)$ from the result of autofluorescence subtracted RS measurements.

Searching the excitationdistribution is implemented in MCX as a ’left-side binary search algorithm. The ’left-side binary search algorithm is known for its speed[262], and when implemented on the GPU, dramatically increases the computational efficiency of emission photon generation. The model then launches an identical number of emission photons as specified for excitation, and propagates them normally in MCX based on the optical properties at the emission wavelength. Upon completion of propagation of the emission photons, the returned results represent a generalized 3D emission volume, which can be scaled by Raman($\kappa_R(\lambda)$) and Fluorescence($\kappa_F(\lambda)$) coefficients to generate unique 4D emission volume flux distributions, with the 4th dimension being wavelength.

The coefficients, $\kappa_R(\lambda)$ and $\kappa_F(\lambda)$, should be informed from raw empirical RS measurements of samples representing each class of voxel to be defined in tissue model, and ideally collected with instruments whose sampling volume is on the order of the chosen model voxel size. The measurements should be fluorescence subtracted[169], and both the intensity of the extracted Raman spectrum and fluorescence background should be retained and used to inform $\kappa_R(\lambda)$ and $\kappa_F(\lambda)$ (From Figure 1).

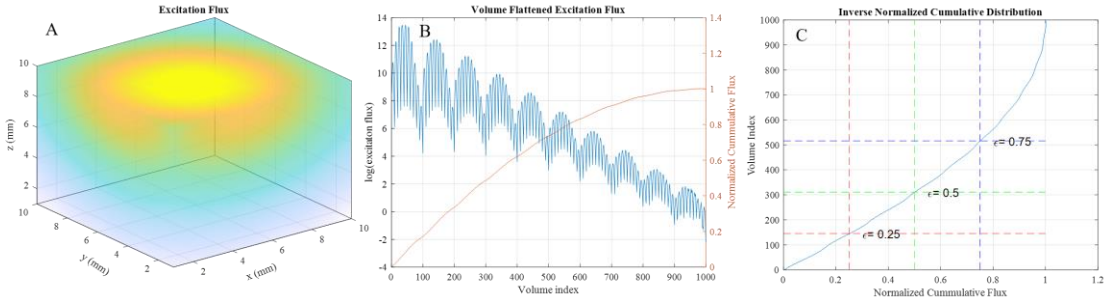

Figure 4-2 (a) 3D excitation flux for a homogeneous sample

3D excitation flux for a homogeneous sample (a). (b) 1D volume flattened representation of the 3D excitation flux (blue) and the corresponding normalized cumulative summation of the volume flattened excitation flux (orange). (c) The inverse of the normalized cumulative flux is bound on the x-axis between 0 to 1 inclusive, which can then be queried by a randomly generated number ϵ. Three examples of the left-hand binary search are shown, where values of ϵ are transformed into a volume index, which is then mapped to a position within the 3D tissue model at which a new emission photon is launched and propagated via MCX.

Phantom Studies

Gelatin Phantoms with embedded HAP capsules

Three sets of phantoms were produced in order to validate the RS MCX model. The phantoms were primarily constructed with two materials, a gelatin-based matrix and hydroxyapatite filled gelatin capsules. All capsules were industry “0” capsule sizes(18.44 mm length, 7.34 mm diameter).

The gelatin matrix consisted of unflavored gelatin powder (Walmart; USA; Knox gelatin) mixed with water at 10% w/v[25]. Optical scattering was primarily introduced through addition of 1 ml of soybean milk being added per every 72 ml of water. The solution was heated to 50˚C to stop solidification. The mixture was poured in plastic cups, cooled down by placing in a refrigerator set to 4˚C for an hour, after which a gelatin

capsule filled with hydroxyapatite (HAP) powder (Sigma-Aldrich; USA; Hydroxyapatite) was placed on the surface of the pre-solidified gelatin, and then followed by the application of a second layer of identical gelatin mixture poured over-top until a satisfactory depth of the capsule had been obtained.

Gelatin Phantom Subsets

The first phantom set consisted of 3 phantoms with pure HAP filled capsules at varied depths of 1, 2 and 3 mm. Capsules were placed atop the underlying gelatin matrix, and the second layer of gelatin mixture was carefully poured in to carefully measured pre-cut plastic cups to ensure appropriate depth.

The second phantom set was constructed with all capsules positioned at identical depths of 2 below the surface. Here, the capsules were filled with different relative concentrations of HAP powder to dry gelatin powder; the ratios were set to be 1:2, 1:1, and 2:1 %w/%w of HAP powder to dry gelatin powder.

Finally, two different gelatin flavors (strawberry and black cherry) of Jell-O (Krafts Foods; USA) were used in place of the unflavored gelatin to generate phantoms with different levels of background autofluorescence. Capsule depth was set to 2 mm.

Characterization of phantom bulk optical properties, μ_a, μ_s

Reflectance and transmittance measurements were collected from 1 mm slices of solidified gelatin mixtures, HAP and gelatin powder with an integrating sphere (IS) (Thorlabs; New Jersey; USA; IS200) illuminated using a quartz-tungsten-halogen (QTH) lamp (Thorlabs; New Jersey; USA; QTH10). Bulk optical properties (μ_a, μ_s) were calculated with software[26]. Calculated optical properties were nearly monotonic in the

Raman fingerprint window for 785 nm excitation evaluated here (835 to 915 nm, 780-1800 cm^{-1}); Gelatin matrix $\mu_a = 0.7 cm^{-1} \mu_s = 1.6e-7 cm^{-1}$, HAP $\mu_a = 11 cm^{-1} \mu_s = 770 cm^{-1}$.

Raman Spectroscopy

RS measurements of individual phantom materials were obtained in order to parameterize $\kappa_R(\lambda)$, and $\kappa_F(\lambda)$ coefficiencts for input into the MC model tissue volume. In addition, RS measurements of all fabricated phantoms were also obtained for comparison against model outputs. All measurements were made within 2 days of phantom preparation to ensure consistency.

The free space optical configuration is shown in Figure 3 . An IPS laser (Innovative Photonics Solutions; New Jersey; USA; I0785SB0050SA) operating at 785 nm with 50mW of excitation power was collimated, passed through a laser line clean-up filter (Semrock: LD01-785/10-12.5), and reflected off a dichroic mirror (Semrock: LPD02-785RU-25), then passing through a 25 mm focal length spherical lens before reaching the surface of the specimen. The calculated spot size was approximately 39 micron. The Raman scattered light was transmitted through the dichroic mirror, passed through a 785 nm long-pass filter (Semrock: BLP01-785R-25), and a 35 mm focal length cylindrical lens was used to couple the beam into a f#/1.8 spectrograph (Andor; USA; Holospec f#/1.8) with spectral coverage from 450 to 1950cm^{-1} and a spectral resolution of 7cm^{-1}. The detector was a 1024x256 pixel back-illuminated deep-depletion CCD thermoelectrically cooled to 70°C (Andor; USA; Newton EMCCD). Raman spectra were collected at three sites on the surface of each phantom, with five scans taken per site per phantom, and a 60 second integration time. Absolute and relative wavenumber

calibration of the 785 nm system was performed using a neon–argon lamp and acetaminophen.

Analysis

In order to relate the simulated spectra from the model to the experimental spectra, a scaling term (f(λ)) was determined.

$$f(\lambda) = Ec(\lambda)/Mc(\lambda) \quad (4\text{-}1)$$

Where Ec is experimental calibration measurement and Mc is modeled calibration. The 2-mm deep HAP gelatin phantom from the validation set 1 was used. The model outputs for all validation experiments was then multiplied by f(λ) to scale the results. The comparison of scaled-model outputs with the experimental RS measurements was the last step of the validation process. Experimental RS measurements were autofluorescence background subtracted[169] and smoothed using a 5-point moving average lowpass filter. Pearson's correlation was used to establish correlations between measurements and their associated simulations at 4 different spectral points - 962, 1181, 1475 and 1693 cm^{-1} which correspond to a phosphate peak $\nu_1 PO_4^{3-}$, phenylalanine, a CH_2 deformation and an Amide I C=O component respectively[14, 257]. All post-model processing steps were done in MATLAB.

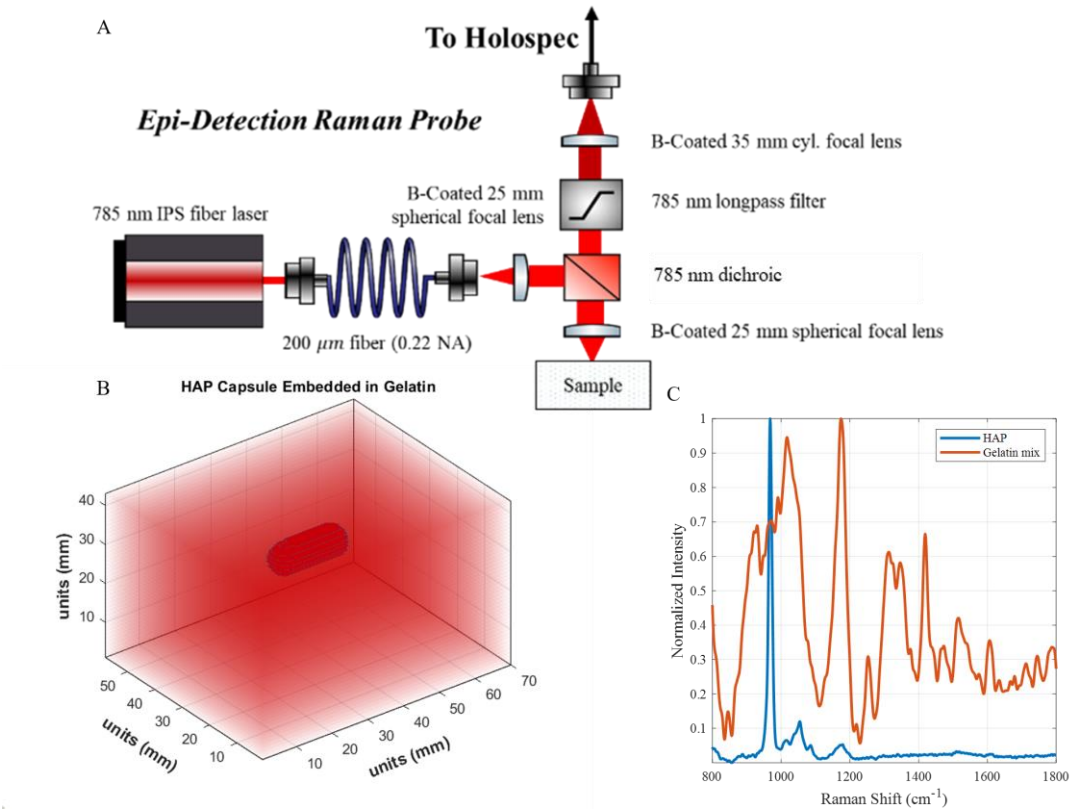

Figure 4-3 A schematic of the Raman probe used to capture signals experimentally.(b) A representative volume representation of a HAP capsule embedded in gelatin as used in the simulations. (c) Raman coefficients for HAP powder and gelatin micture.

Results

The simulation took under 22 minutes (21.54 min on average) to simulate 161 different discrete wavenumbers between 763 to 1801 cm^{-1} with 5e7 photons per simulation, totaling 8e9 photons per simulation.

1st phantom set – different depths

Figure 4 a shows the experimental Raman measurements at 3 different HAP capsule depths. As the depth increases, the overall signal descends. A similar trend in seen in the model (Figure 4 b). Comparison of the 962cm^{-1} phosphate peak using Pearson's correlation in Figure 4 c shows an R^2=0.96.

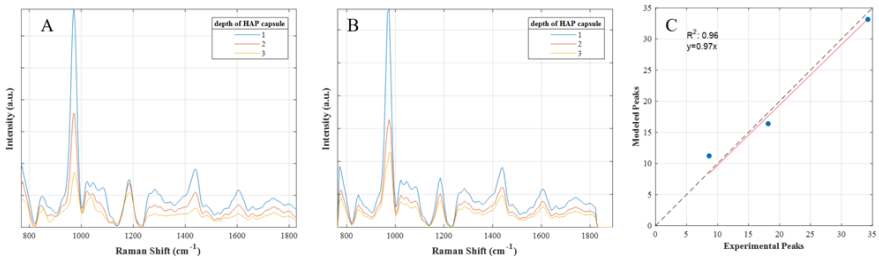

Figure 4-4 (a) Experimental RS signal for three depths. (b) Simulated signal for the same three depths. (c) Correlation between experimental and simulated at the 962cm^{-1} phosphate peak.

2nd phantom set - different relative concentration

Figure 5 a shows the experimental Raman measurements at 3 different concentrations of HAP. As the ratio increases, the signal at 962 $cm-1$ increases as HAP becomes more dominant in terms of volume inside the capsule. Again, the model shows similar trends in figure 5 b. Figure 5 c shows the correlation between the experimental and modeled spectra for the 962 cm^{-1} peak is good with R^2 of 0.91.

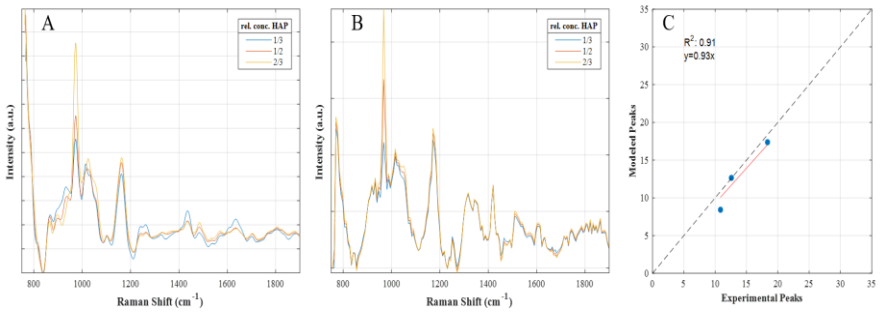

figure 4-5 Experimental RS signal for three relative concentrations of HAP/dry gelatin powder. (b) Simulated signal for the same three concentrations. (c) Correlation between experimental and simulated at the 962cm^{-1} phosphate peak.

3rd phantom set – different background autofluorescence

Figure 6 shows the experimental (a) and simulated (b) overall signal for strawberry and cherry flavored gelatin. With the relative intensity of the experimental and modeled spectra, without fluorescence subtraction, being relatively similar. The SNR (calculated at the intensity 962cm^{-1} divided by the standard deviation of the signal from 1650-1750cm^{-1}) is greater for the strawberry phantom vs the cherry phantom for both the modeled (36.2 vs 14.9) and experimental (38.8 vs 16.1) spectra.

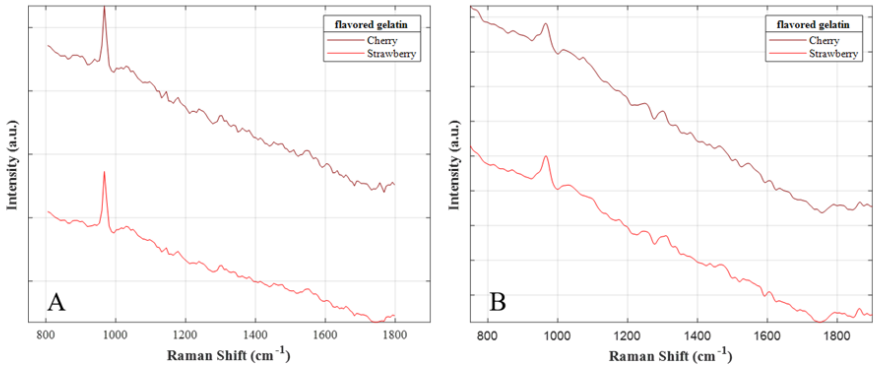

figure 4-6 (a) Experimentally captured net signal (background not removed) for two different flavored Jell-O phantoms (b) Simulated net signal (Fluorescence + Raman) for the same two flavors.

Discussion

Parallelization of DR MC modeling has led to more profound understanding of biophotonic phenomena, including phenomena in optical dosimetry[263], bone injuries[264], and transcranial photobiomodulation[265, 266]. The increased computational capacity has enabled a inspection of a broader range of modeled biological variation, that practically manifests as an expansion of the tissue model's parameterization. In RS, the measured signal is a feature rich spectra with features from a bunch of biochemicals all contributing to the final measurement. In comparison with DR spectroscopy, RS adds an additional dimension rich with diagnostically valuable biochemical information.Incorporating this expanded biochemical parameterization in MC models of RS could also result in advancements, as was the case in DR.

Prior Raman MC models were implemented in a sequential manner[98, 102-105], however recent work by Roth[259] has demonstrated the benefit of a parallelized Raman MC model, including the ability to model a broad Raman spectrum, and evaluate the influence of internal spectral absorption on the model outputs. This custom developed approach uses GPU acceleration combined with a variant of a two-step MC model process[91, 103] to produce statistically robust simulation results with less photon numbers than the direct single-photon tracking approach. This represented a significant improvement over sequential MC models of RS, however if RS MC studies are to mimic DR studies that investigate a wide range of biophysical variations in the tissue, further acceleration would be beneficial. Furthermore, modeling aimed at informing clinical translation of RS would also benefit from incorporation of appropriately scaled autofluorescence background, which can dramatically confound *in vivo* measurements. Here, a GPU accelerated MC model was developed from the open-source MCX project[89],which offers a well-developed platform with a flexible, wide breadth of physical parameters, and has a well-established ability to offer insight into biomedical diagnostics [263-266]..

The most efficient approaches for MC simulation of excitation-emission phenomena have all been developed using the concept of 1st determining the excitation spatial distribution, and then generating the emission in response. Previously, emission photons were generated by performing the convolution of a single emission through the entire tissue model geometry[103, 258]. This approach is burdened by the computational cost of convolution. A more efficient statistical alternative is to uniformly generate emission photons throughout the tissue model space, and then weigh the photons by the

excitation prior to further propagation. In this manuscript, the Isoweight algorithm generates emission photons at positions statistically sampled from the cumulative excitation distribution. As a result, the statistical likelihood of emission photon generation at any position in the tissue model space matches the physical basis for Raman scattering. In addition, the computational solution utilizes the left-side lookup routine, which can be easily parallelized on the GPU, resulting in an overall approach that is both statistically and computationally efficient. As a result, the MC model for RS is much better positioned to produce statistically robust outputs for RS across a wide range of wavenumbers while simultaneously producing the corresponding autofluorescence background that also be of importance in biomedical RS. The simulations reported in this manuscript were able to cover the fingerprint region, with 5e7 photons per simulation at 161 spectral positions (9.039e9 total photons), in under 22 minutes.

Validation of the isoweight approach for generation of RS emission photons was performed through the comparison of empirical RS measurements with MC models of RS. Figure 4 shows the agreement between modeled and measured Raman spectra for 3 different depths. This derives from the fundamental basis that the Raman scattered signal intensity will scale with the excitation intensity, which decreases with increasing capsule depth. Figure5 shows the agreement between modeled and measured from phantoms with varying concentrations, with an overall correlation coefficient of 0.91.This agreement fundamentally derives from the understood linearity of Raman scattered signal intensity vs. chemical concentration.

Finally, the ability of the isoweight approach to also appropriately model autofluorescnce was demonstrated based on the agreement between the modeled and

simulated spectra collected from phantoms fabricated using different artificial flavorings (Figure 6) . The relative agreement between modeled and experimental, SNR for the two background levels indicates that quantitative measures of spectroscopic quality are also retained in the MC model simulation. Alternatively, noise could also be simulated in the system in post model processing if more precise matches between model and empirical were sought for the purpose of device development.

Conclusion

A new approach for MC modeling of Raman spectra based upon the MCX platform is reported. The approach is able to produce modeled Raman spectra at >160 independent spectral bands, as well as the corresponding autofluorescence background signal. The model was aided by the implementation of a fast 'left-side' algorithm placed on the GPU side of the MCX platform, along with the excitation flux distribution. The model produced full Raman spectra in a feasible amount of time (301 spectral emission surfaces in <20 minutes), which is faster than previous Raman models. This massive acceleration can allow for Raman investigation of many different optical and physical configurations, such as optimizing a fiber optics probe for in vio measurements, simulation of subtle differences between normal and diseased tissues, or investigation of the effects of complex structural features within the tissue model volume. Much like how MCX has facilitated growth in understanding of complex phenomena in diffuse reflectance, we hope that this model can provide the same for Raman spectroscopy.

CHAPTER 5

APPLICATION OF GPU ACCELERATED MC MODELING OF RAMAN SCATTERING TO INFORM MULTI-SCALE SPATIAL RELATIONSHIP BETWEEN MICROSCOPY AND TISSUE LEVEL ANALYSES

Introduction

One of the most common, aggressive, and fastest-growing adult brain cancer is glioma [267], and although there have been extensive developments in the comprehension of the tumor's genetic origin [268] and in the diagnosis and treatment of these tumors[269], the 5-year survival rate varies immensely for low-grade tumors[270], and the median survival rate for high-grade tumors is only 12-15 months[271]. The initial symptoms of gliomas are nondescript and include headaches, which can be confused for other ailments, such as migraines and nausea[272], and often get misdiagnosed early on, allowing the tumor to grow in severity. The standard therapy for gliomas is maximal surgical resection [192] followed by postoperative radiotherapy and chemotherapy[273]. However, glioma tumor cells are inherently resistant to conventional therapies such as temozolomide (TMZ)[274], and unfortunately, the response to treatment is heterogeneous and unpredictable[275]. Despite such aggressive treatment, gliomas often recur in most patients [276]. Several factors make the treatment of gliomas difficult [277], including the brain's limited capacity to repair itself[278] and the fact that most therapeutic drugs cannot cross the blood-brain barrier (BBB)[277]. These issues make the development of a "cure" for gliomas a slow process, but progress is being made day by day[279-282]. It is clear that demographic and environmental factors are important for predicting outcomes in individual cases, but understanding the underlying molecular characteristics of an individual patient's cancerous tissue may account for the variability from case to case and can lead to better survival outcomes[283].

The most effective treatment for high-grade tumors remains total resection [284], even with the advent of new innovative discoveries in immunotherapy[285] and genetic

editing [286], and chemo- [287, 288] and radiotherapy treatments [289]. Visualizing and discriminating brain tumors and diffusively embedded tumor tissue post-resection in live-time is of great interest for guiding the invasive neurosurgeries required for the maximal resection of tumors while leaving as much of the surrounding normal tissues, so as not to cause neuro-deficits in the patient [290]. Groups have used fluorescence-guided spectroscopy to assist in these difficult surgeries to great effect using 5-ALA fluorescence [291-295] or fluorescein salts [292, 296-298]. Fluorescence spectroscopy, along with intraoperative MRIs and ultrasound, have achieved a higher specificity in margin detection of cancerous versus benign tissues, and are slowly becoming a valuable tool in the neurosurgeon's toolbox[299]; however, fluorescence techniques are heavily reliant on the incorporation of exogenous markers in the tissue and bind to tumors with varying degrees of success [300].

Raman spectroscopy is an inelastic effect that light has with matter so that the frequency of incoming light is up- or down-shifted after a scattering interaction with a molecule. The amount that the photon is shifted, measured in cm^{-1}, is associated with a vibrational state of the molecule, which varies according to the molecule's composition. Raman spectroscopy aims at recovering the rich Raman spectra that result from these inelastic collision states. Thus Raman spectra are deeply informed by the biochemical nature of the molecules in a particular tissue. Several groups have used Raman spectroscopy to recover the Raman features in both the fingerprint region (0-2000 $cm,^{-1}$) and the high-wavenumber regime (2800-3600 cm^{-1}). Jermyn et al.[162] developed a handheld Raman probe that could be used to interrogate brain tissue in live-time (<0.2s integration time) during brain surgeries, which they tested on 17 patients with varied

tumor grades. The probe had an overall accuracy of 92%, indicating that handheld probes such as this could be instrumental in determining malignant brain cells embedded in normal tissues. However, this study was a feasibility study aimed at demonstrating that Raman spectroscopy could be used intraoperatively to help in guiding tissue resection at the microscopic level. The same group would also use a simplified probe designed to look at the high-wavenumber region, which is sufficiently shifted in frequency so as not to require filters, noting a high ability to discriminate between malignant and benign normal tissue at these frequencies in real-time[256]. In both studies, the authors pointed to the fact that Raman spectroscopy had the ability to provide useful guidance in surgeries for the removal of tumor and invasive tumor cells, noting in a previous paper [164] that these Raman probes had the potential ability to detect cancerous cells centimeters beyond the threshold of stereotactic MRI scans.

However, a potentially weak link has existed in Raman spectroscopy, including brain-guided Raman spectroscopy, which comes down to how the resultant spectra are segregated based on robust statistical models. These statistical models can offer insight into variate tissue analysis, but do not provide a fundamental understanding of the underlying cellular morphology that defines the resultant Raman spectra. As such, statistical models can only provide a meaningful segregation scheme on the existing data but are maladapted to provide predictive abilities on new tissues based on cellular morphologies not seen on the current data. This problem has been noted by Desroches [256], who explains that to make Raman spectroscopy commonplace would require a much more expansive patient set to capture the full heterogeneity associated with brain cancer.

Alternatively, an understanding of changes in the cellular morphology and its effect on the overall Raman signal could be done by using Raman Monte-Carlo modeling. Raman MC modeling can suggest the multi-scale relationship between cellular features to the bulk Raman signals by using volume modeling at the microscale level, with signal outputs comparable to macroscale bulk signal collection.

In this paper, we use a Raman Monte-Carlo platform previously constructed and validated by our group, which is accelerated by GPUs, to explore how changes at the cellular level of a medium representative of brain with diffuse glioma, i.e., a brain post-surgery, by its grade, to bulk Raman signal captured by a Raman probe on the surface of the excision cavity. We will present the volume construction of a section of the brain, its refinement into the cellular scale, selection of optical properties and Raman coefficients, and overall results of bulk Raman modeled signal, as well as the individual signal from white, grey and cancer matter, which are inspected in both the spatial and spectral domain. Finally, we will discuss the effect of different cancer grades on the overall modeled signal, and propose a theoretical Raman illumination/detection offset that optimizes signals coming from cancer cells.

Materials and Methods

Grades of gliomas

Gliomas are graded according to a mixture of phenotypic and genotypic parameters, as discussed in [301]. Briefly, all gliomas share similarities in growth patterns and cellular and morphological behaviors, but at different rates. Grade 1 gliomas are the most benign tumor types of the glioma family and are characterized by the lowest

growth rate and penetration into adjacent normal tissue [301], and subsequently, have the highest survival rate. Grade II gliomas, including astrocytic tumor and oligodendrogliomas, are characterized by a faster growth rate than Grade I, with some cells and cellular features beginning to look slightly different than normal surrounding cellular micro-environments. Grade III tumors are associated with highly cancerous tissue, actively reproducing abnormal cells, thus becoming a decidedly infiltrative tumor. The final grade is the most malignant brain cancer, with very abnormal cells reproducing into the adjacent healthy tissue, and sometimes forms new blood vessels to support this aggressive expansion rate. Grade IV tumors are often labeled as glioblastoma multiforme (GBM) and have the worst survival rate of all diffuse gliomas [271].

Raman Monte Carlo Model

The Raman Monte Carlo model employed in this study was previously developed by us and is described in more detail elsewhere, and is accelerated by using available NVIDIA GPUs. Briefly, the steps that the model takes to generate Raman signal are presented. First, the model is allowed to run at the excitation wavelength, according to a launch function specified by the user, which requires some additional user-supplied information (e.g., disk radius for disk type, gaussian waist for gaussian, etc…). The photon is first set to unity and propagates through the medium by scattering and absorbing interactions, according to the optical properties of each layer. Once the photon reaches a particular threshold in terms of its weight, it is then terminated. This process is repeated until the number of launched photons is reached; the number of photons launched is also user-supplied. Once the first simulation is finished, the excitation flux distribution is split by layers and ratioed by the total number of photons launched. The

emission number of photons is then split into layer simulations according to their ratios (e.g., 67% of 1e7 emission photons go to layer 1). A launch volume is created having 0's everywhere except the current layer volume, where the voxel intensity is driven by the flux of photons passing through it, flattened, cumulatively summed and normalized with the sum under the curve so that the sum of the distribution equals 1. A 'left-side' binary search algorithm is then used to find a launch position in the launch volume, by finding a vector index that is just to the left (lower than) of the value of a randomly generated number. Once the index vector is found, it is then converted to a 3D launch position, from which a photon set to unity is then launched isotropically and allowed to follow the usual MC rules with emission optical properties until it is captured by a detector on the surface. The weighed photon is then multiplied by its intrinsic Raman coefficient, and the process is repeated for the number of photons allocated to that layer. After each non-zero flux layer is allowed to complete this process, the emission photons from each layer are accumulated to form the net Raman signal.

Volume Construction

Volume construction was done by using a 400-micron resolution brain atlas (classified into grey, white, and cerebrospinal fluid (CSF)) from the BigBrain database [302]. A 5-mm cube around Broca's area (although any area of the brain can be inspected) was extracted from the overall brain structure and was resampled to 25-micron, which is the approximate size of cellular features in the brain [303].

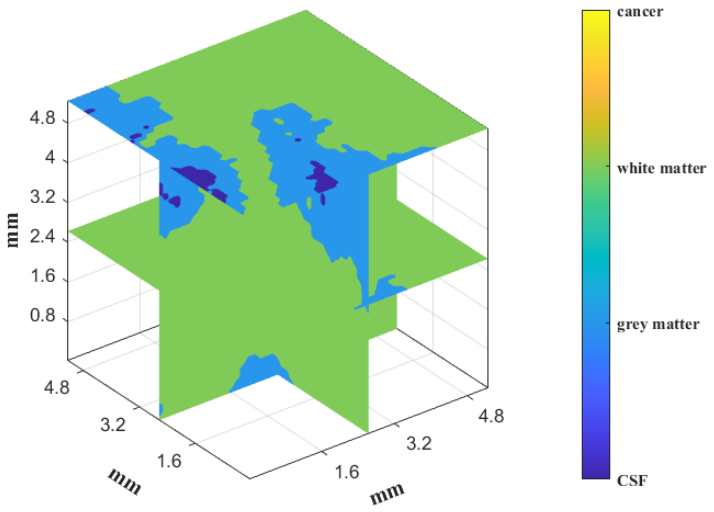

Figure 5-1. Volume render of non-cancerous brain at the Broca's area.

The white matter represents the bulk of the tissue, followed by grey matter and CSF. The virtual fiber probe is querying the structure from the top of the model, with illumination heading straight-down, and placed directly in the center of the tissue model.

Tumor cells were inserted into the volume according to half-Gaussian functions, taken to the left of the center point of the Gaussian, with different intensities and different standard deviation according to the grade of cancer. Figure 2 is a graphical representation of the normal to grade IV tumor dispersion; green volume is white matter, blue corresponds to grey matter, and dark blue represents CSF, and diffuse cancer is yellow. The volume can be reconstructed in a fast manner over any part of the brain, constructed to be any arbitrary dimensions for the volume, and any z-axis function for the inclusion of cancer cells, as well as layer discrimination (i.e., only include cancer in white matter) and lateral probabilities (i.e., x<1mm). The volumes each took less than 30 seconds to

construct and were 400 voxels in height, width, and depth, with units of the voxel being 25 microns.

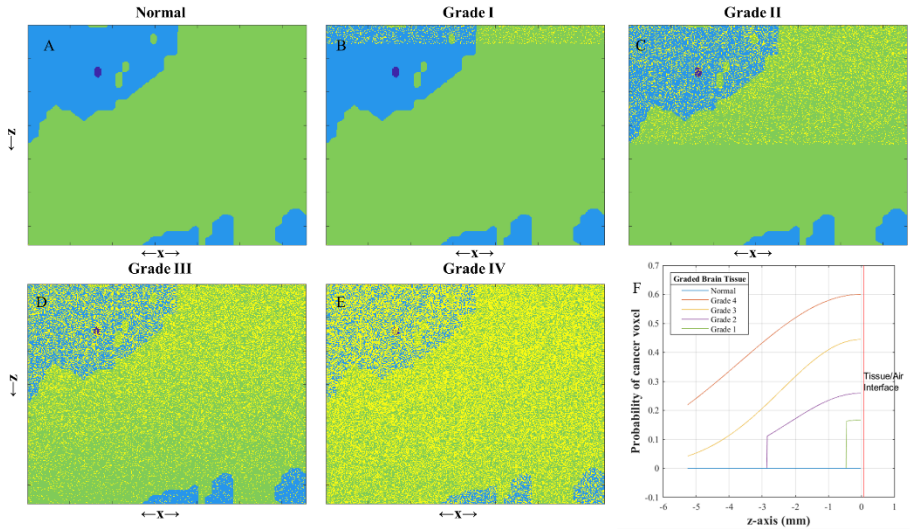

Figure 5-2. The five graded volumes cross-sectioned

The five graded volumes cross-sectioned and viewed from the side so that the direction of the incoming light is from top to bottom (normal (A) to grade IV (E)) with yellow inclusions representing diffuse cancerous cells, and Green=White matter, Light Blue=Grey matter, Dark Blue=CSF. (F) Probability distributions specifying the probability of cancer inclusion based on cancer grade.

Optical Properties

Optical properties for the brain were retrieved from a literature review. The excitation and optical emission properties for grey and white matter and astrocytoma's μ_a, μ_s and g were extracted from a study by Yaroslavsky [60], who reported these properties from *in vitro* human brain tissues. The refractive index of these layers was extracted from a review paper by Jacques [41]. The optical properties of CSF were kept constant in this study and were retrieved from [304]. The Raman coefficients for the

normal brain, as well as grades 1-4, were extracted from [305], who used visible resonance Raman spectroscopy at 532 nm to inspect the Raman spectra of samples extracted from human brains by cancer grades. The normal and grade IV spectra were used as a minimum, and maximum spectra, respectively, and grade I-III cancers were set to be 0.25, 0.5, and 0.75 of the difference between the two tissues. The optical properties and Raman coefficients used in this study are presented in Figure 3. The optical properties of the ambient environment were assumed to be the ones for air and were set to be 0, 0, 1 and 1 respectively for μ_a, μ_s, g, and n.

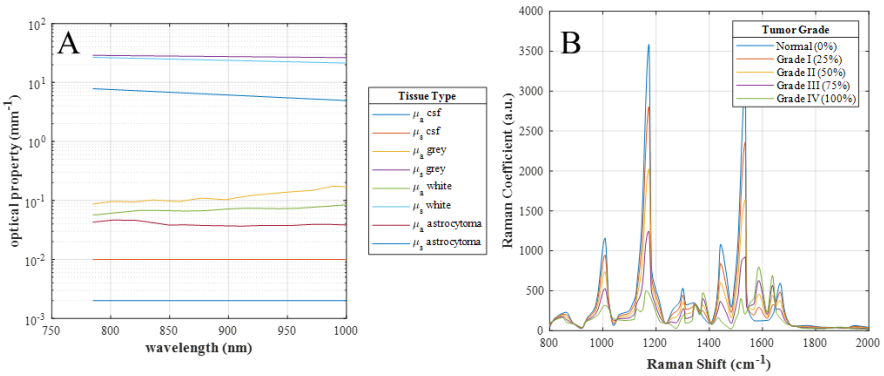

Figure 5-3. (A) Optical properties of four different components of the brain at 785 to 1000 nm. (B) Raman coefficients of normal and cancerous tissues from 800 to 2000 cm^{-1}.

Simulation Details

Simulation parameters were set to simulate a fiber-probe configuration realistically. The light source was set to be at 785 nm and was an angular gaussian beam with a zenith angle set to be 12.71° (corresponding to a 0.22 NA optical fiber), which was

placed just atop of the volume facing down, in a contacted position against the tissue, in the exact center of the cube's surface. The number of photons launched was 5e7 for all subsequent simulations for both the excitation and emission simulations. Three hundred Raman shifts were simulated, varying linearly from 800 to 2000 cm^{-1}, offering a four cm^{-1} resolution. Simulations were run over the five volumes, taking on average 6.83 hours per simulation set.

Analysis

Once the simulations were finished, the layer emission at each wavelength was multiplied by that layer's intrinsic Raman coefficients (Figure 2b), forming that layer's escape function. The escape function from each layer was summed in order to retrieve the net Raman signal at the surface, which is presented in the results section, as well as layer's contribution to the overall signal as a function of cancer grade. In order to further analyze data in the spatial domain, the detected photons captured were placed inside spatial bins based on their outgoing trajectories and positions. One hundred voxels stretching in the x-y plane from the source position were split into 75 bins so that each bin represented ~50 microns and the span of the gridded bins was ~4 mm, which is the approximate size of a commercially available fiber probe (RP24, Thorlabs, New Jersey, USA).

A ratio of layered to total bulk signal is defined as $R_l = 100 * C_l / \sum C_l$ where C_l is an individual layer's contribution to the bulk signal and $\sum C_l$ is the bulk signal. This ratio can help in analyzing a particular layer's importance to the bulk signal.

Results

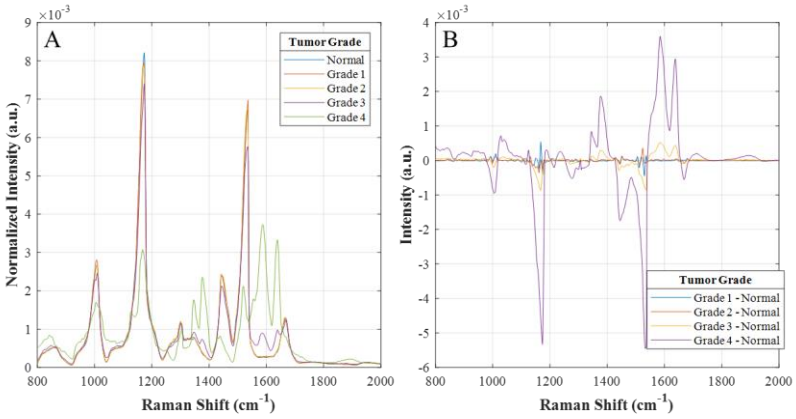

Figure 5-4. (A) Normalized by sum Raman Signal simulated at the surface

Normalized by sum Raman Signal simulated at the surface, incident to the illumination beam for normal tissue, for a 200 micron fiber, and the four incrementally graded cancer tissue volumes. (B) Difference between cancer grade to the normal tissue, indicating peaks with strong deviations as a function of spectral and grade variations. Strong negative peaks are seen at 1157 and 1521 cm^{-1}, and seem to get more intense with increasing grade, whereas strong positive peaks are apparent at 1521 and 1667 cm^(-1)and gets larger with increasing grade.

First, the normalized Raman signal was inspected using a typical illumination-detection configuration (Figure 4a). The source-detector offset was 200-microns, and the detection fiber was assumed to be 200-microns in diameter, meaning that the voxel offset between illumination and detection was four voxels, with the fiber spanning 4-voxels in the lateral positions. The intensity of normal tissue is the most intense at most Raman shifts, and intensity regularly decreases with increasing grade. The major peaks at ~1003 cm^{-1} and ~1668 cm^{-1} represents protein bands, the peaks at ~1150 cm^{-1} and ~1521 cm^{-1} are representative of various lipoproteins, and peaks at ~1455 cm^{-1} are due to rich fatty acids [305]. Past 1800 cm^{-1}, there are no more evident peaks. Figure 4b shows the difference between grades, defined as the current grade minus the normal tissue. The

most intense variation occurs during the Grade IV - normal, and the intensity change decreases gradually as tumor grades decreases. The fact that peaks are either negative or positive is an indication of a strong deviation of that peak when compared to the normal signal, with signal close to the 0 point being minimal changes in spectral intensity between the cancer grade and the normal tissue.

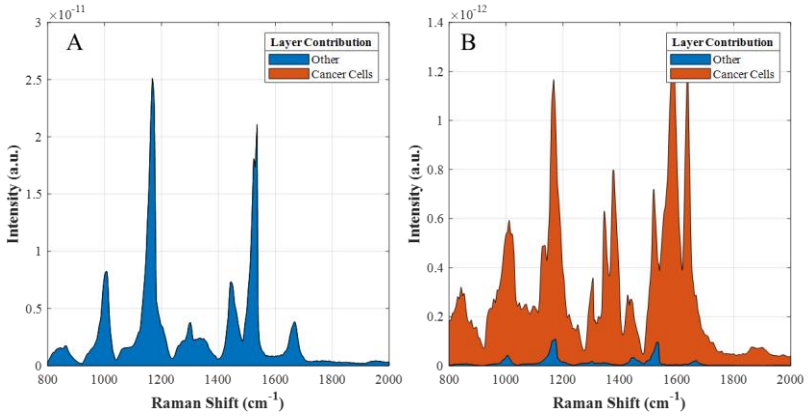

Figure 5-5. Individual layer contributions

Individual layer contributions to the net Raman signal seen in Figure 1 for grade I cancer (A) and grade IV cancer (B). The grade I cancer tissue volume's signal is coming from mostly the other contributors (white, grey and CSF), whereas the signal seen in the grade IV cancer overwhelmingly represents cancer cells.

Layered contributions to bulk Raman signal are shown in Figure 5, for the grade I (5a) and grade IV (5b) cancer tissue models. CSF, white and grey matter are represented as the others categories, with cancer cells being their own category. The percent contribution from cancer cells is largest in the grade IV cancer, but the overall signal for grade IV is one order of magnitude less than that seen for grade I cancer. When looking at the percent fractional volume of cancerous to non-cancerous cells in the tissue models,

the different contribution is explained by the shear factor of increased cancerous to non-cancerous cells in grade IV vs I (1.49 cancer cells/normal cell for grade IV to 0.02 cancer to non-cancer cells for grade I).

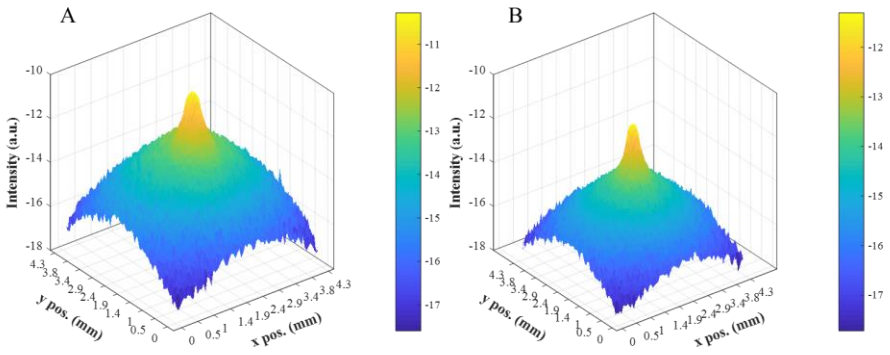

Figure 5-6. Logarithmic bulk Raman signal over the spatial domain at 1157 cm^{-1}, for Normal tissue (A) and Grade IV tissue (B).

Up to this point, only a specific fiber probe has been examined. However, another avenue of exploration through modeling is in the spatial dimension. Figure 6a-b shows the spatial grids over the lateral surface escape dimensions, spanning 4 mm in each dimension. The peaks are most significant at the epi-detection point and drop off in each dimension rapidly. The normal tissue (Fig5a) has the most intense signal, whereas the grade IV volume (Fig. 5b) has a reduced signal.

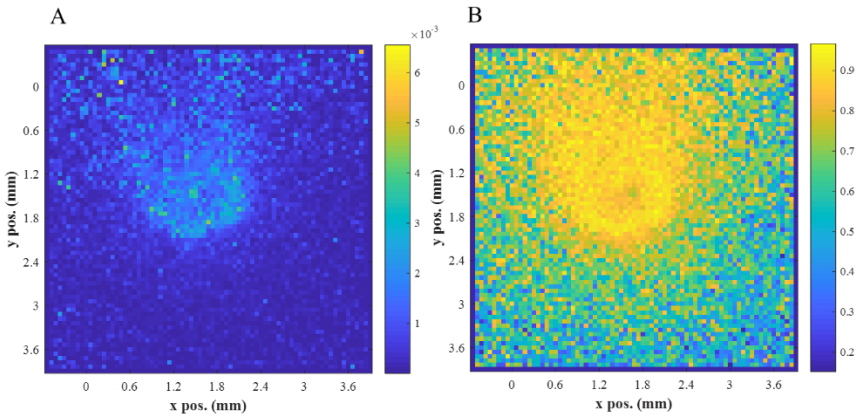

Figure 5-7. Spatial profiles for Cancer/Total

Spatial profiles for Cancer/Total for grade I tumor volume (A), and grade IV tumor volume (B) at 1173 cm^(-1). The grade I ratio is much less than 1, whereas this ratio almost reaches 1 in the grade IV tumor environment.

Figure 7 shows the spatial distribution of the ratioed term R in terms of cancerous layer contributions. The ratio gets more significant with a higher grade, which is supported by the volume construction, as a more dense packing of tumor cells increases the bulk signal from that layer. Also of interest is the spatial profile of the ratio for both situations. There is a ring around the illumination source that is more intense for grade IV, but there is also a bulb in the north of the image, which does not appear in the other lateral positions. This is due to an increase in grey matter in this location, which is shared amongst the two volumes. Lastly, these images show the relative contribution of cancerous tissues to the overall signal. A value closer to 1 for R indicates that a majority of the signal is due to the cancerous cells, which is evidenced in figure 7-b, where the mean ratio of cancerous cells is 69%, whereas the ratio for figure 7-a is much lower at 5.64e-2%.

Discussion

In this manuscript, we demonstrate that using a fast Raman MC model can be useful in understanding the link between microscopic cellular data, and bulk Raman signal. We constructed theoretical tissue volumes that represent grades of diffuse glioma cancer at the microscopic level, which was inset into realistic volumes of the brain. Raman spectroscopy was simulated on a layer basis, and the bulk signal retrieved was separable into layers, frequency, and spatial components.

Fig. 4a shows Raman spectra for the five volumes we simulated. Importantly, these simulations resemble the spectra provided by Zhou [305], which is a validation that the model seems to be working well. As the cancer grade goes up, there is a decrease in the Raman signal, which is explained by the reduced overall intensity of Grade IV cancer versus normal tissue. This signal reduction is appointable to necrotic tissue formation and hypoxia in higher-grade tissue [305], which generally decreases the overall Raman spectra. The results from figure 4a are also complemented by previous in-vitro studies done by [306] and [307], who independently noted that transitions to higher grade cancers lead to a reduction in lipid peaks while maintaining protein bands. Fig. 3 shows the Raman contribution to the overall signal in terms of cancerous cells only. Here, we can see very clearly that the bands at 1438, 1527 and 1157 cm^{-1} attributable to lipids and fatty acids are not much higher for Grade IV cancer than the previous grade, in the 1438 instance, the Grade IV peak is actually ower than the Grade III peak. However, peaks at 1005 and 1667 cm^{-1} are much higher for Grade IV than for Grade III, which supports [306, 307] observations.

Fig. 4b shows the difference plots for each grade transition compared to a non-cancer tissue model. The most intense drop-off is seen for the Grade IV-Normal transition, and in general, the most intense peaks for this plot are seen at 1157 cm^{-1}, indicating a sharper decrease from this peak. The second-most drop in intensity is observed at 1521 cm^{-1}, which makes sense as both these peaks are associated with carotenoids and tryptophan [305] which are associated with healthy tissue's antioxidant defense system [308] and participation in the synthesis of proteins [309] respectively, and which gets deregulated as cancer grades increases.

Fig. 5a-b show the associated brain layer contributions to the overall signal (R_l) for the grade I and IV tissue models. The cancer cells contribute minimally to signal from the grade I tissue model (5a), but the inverse can be said about grade IV cancer, in which the majority of the perceived signal is due to cancerous cells. This is due to the complex micro- and macro-environment, which can change dramatically based on cancer placement in the brain. An accelerated Raman MC model could overcome this problem by simulating bulk signal responses across the entire brain, which is a faculty we have implemented in the volume construction. In this manuscript, we only inspected one site, but many sites can be constructed, along with different cellular cancers, which could present a database of cancer responses. This could potentially be of value for neurosurgery, as the training of a prediction algorithm could be done by modeling as opposed to recruiting a massive cohort of patients, which addresses the issue brought by Desroches [256].

Another benefit of Raman modeling is the spatial dimension offered by the escape function. Fig. 6 shows the spatial distribution of bulk Raman signal over the lateral

spatial dimensions for the normal volume (fig 5a) and the grade IV volume (fig 5b.). The grade IV volume is generally lower than the normal tissue due to a decrease in lipoprotein production, as well as the increase in necrotic tissues [310]. The point where the laser hits the tissue has the highest intensities and intensities monotonically decrease in each dimension as the distance from the illumination increases. From inspecting fig, 5, it seems like the best placement for fiber-optic probes is right next to each other. However, when looking at fig. 6, which displays the A_{cancer}, there is a ring-like feature around the illumination that is strongest at 7-pixel distance from the illumination source, while the 200-micron detection source is only four voxels away from the illumination. Additionally, the ring is incomplete, as to the north, the A_{cancer} does not diffuse as rapidly as the other dimensions, which is likely due to the local grey matter's increased scattering coefficient at the excitation and emission wavelengths, which allows for an enhancement of the cancerous signal coming from deeper in the tissue volume.

There are limitations in this study that curb its potential uses in clinical brain surgery. First, the Raman profiles for normal and diseased brain tissue were obtained from a literature review, and the cancer grades were statistically set to be in between the two tissue types. This does not take into account the features of the spectra that are shifted spectrally due to chemical changes that can occur during brain cancer, which has been noted by [305]. The background autofluorescence was assumed to be null in the simulation, although this may not be the case in real-time Raman imaging [162, 256], and methods for subtracting the autofluorescence may increase the discrepancies between simulated and experimental spaces [169]. Finally, there is the question of massive implementation, which would most likely require clusters of GPUs in order to inspect all

possible variations of micro-volumes of the brain in order to make a look-up table that can guide surgeries. Even though the MC model used in these simulations was a fast GPU accelerated MC, the simulations still took over 6 hours per volume, due to the enlarged resolution of the volumes required for micro- to macro- inspection of the tissues.

Conclusion

Even with these limitations, the potential of modeling microstructures to macro-scale bulk signal offers an avenue for the exploration of bulk behaviors associated with microscale variability, which can improve brain surgery predictions by providing a possible way to use Raman spectroscopy combined with model simulations to resect cellular cancer features in a more informed manner. In this paper, we varied inspected volumes based on cancer grades and discussed how the bulk Raman signal changed according to the increased proliferation of cancerous cells. Additionally, we inspected the spectral and spatial domains of the bulk and individually layered Raman signals, and noted changes in spectra from either the bulk or individual layers. Finally, we discussed the potential of this type of modeling to aid in the guidance of Raman spectroscopy in brain surgeries with the production of a look-up table across multiple dimensions.

CHAPTER 6 PERSPECTIVES & CONCLUSIONS

Since the conception of MC models in the late 1980's these models have become commonplace in the inspection of biological turbid media and has gained traction in clinical applications over the years. MC's demonstrated value in these clinical settings along with a parallel computational boom has made the use of MC models commonplace in most optically related studies.

In our first specific aim, we used an accelerated MC model to study the complex bilirubin melanin interactions through different devices and notice that illumination collection geometry had a very profound effect on the devices' ability to collect information related to bilirubin. However, the MC model applied in this situation was a forward MC model which is a well-posed problem where input optical properties result in only one output reflectance; in the reverse situation where optical properties are sought given a particular signal, the problem becomes ill-posed, that is to say, more than one set of optical properties may result in the same reflectance.

This was evidenced when we tried to use inverse Monte Carlo (iMC) to directly solve for bilirubin concentration using clinically retrieved images from neonates at Vanderbilt University hospital, as well as neonates in LMIC sites. In this situation, we also were furnished with results from serum bilirubin testing, which was done at most 2 hours after the images on a cellphone and offered the ability to compare the results from our iMC model to the values returned from the serum testing. The images from the cellphone were taken with predetermined exposure time, which was calculated to preserve most of the signal from the blue channel, although this had the effect of saturating the images in the red channel. Correction factors for the image detector

response and inter and intra-phone variability were taken against a white piece of HDPE plastic, which was chosen for its cheapness and similarity to more expensive calibration pucks used in labs. A correction factor was also implemented to relate the experimental context to the simulated context, by simulating the same piece of plastic and then dividing the experimental to simulated signal across the simulated pixel values. Upwards of 20,000 different situations were modeled, to represent one of the dimensional space (bilirubin, melanin, hemoglobin, wavelength, phone design) with sufficient resolution in each axis. Normalized experimental images were then compared to the normalized simulated space, which resulted in a poor correlation with the serum bilirubin values ($R^2 < 0.4$). This inaccuracy is due, in part, to the fact that in implementing an MC approach to tissue inspection, approximations have to be made which do not necessarily reflect the actual situation. For example, in our model, assumptions were made on the thickness of each layer of the tissue, as well as assumptions on whether to allow external or internal interface specular reflection, the general shape and distribution of chromophores in the medium (which we assumed was homogenously distributed per layer, referring to Fig 2-13 and Fig. 2-14, this is clearly not the case). When looking for trends in the forward model, as well as validating extremely homogenous phantoms, these model inaccuracies do not matter as much. For example, when inspecting the forward trends, we were more interested in seeing how increased melanin and device configurations could complicate the retrieval of bilirubin related signals. However, these features of the skin matter when using the inverse MC model, as variations in any of these features, such as the size and location of micro and macro-vascularization and melanosome deposit sites in the stratum corneum, could affect the simulated signal

greatly. Alternative methods were then explored with the clinical data, which were numerous and variably successful. The problem was principally how to handle the data coming from an 8-megapixel cellphone camera, which once demosaiced, had 24 million different pixels representing a single bilirubin value. Some of the alternative methods tried on the data was principal component regression (PCR) and multivariate regression, deep and convolutional neural networks (DNN, CNN,) and non-parametric machine learners such as support vector machines (SVM) regressions with different kernels and decision tree learning approaches, but all these methods had generally poor correlation coefficients when using a cross-validation scheme.

Finally, we developed an algorithm that aims at finding the best box positions for n-boxes in each of the three channels on the cellphone. These boxes are further averaged and the log of the meaned values is taken, after which the logged values are linearly regressed to the serum bilirubin values. The algorithm tries a new position and determines if this position is better or worse than the previous position by comparing the value that results from the linear regression to the actual serum bilirubin levels in the neonate. The algorithm is set with trying to minimize the differences between the two values by moving these four boxes in three channels. By using this methodology, much higher correlation coefficient could be achieved on infants from low-income countries.

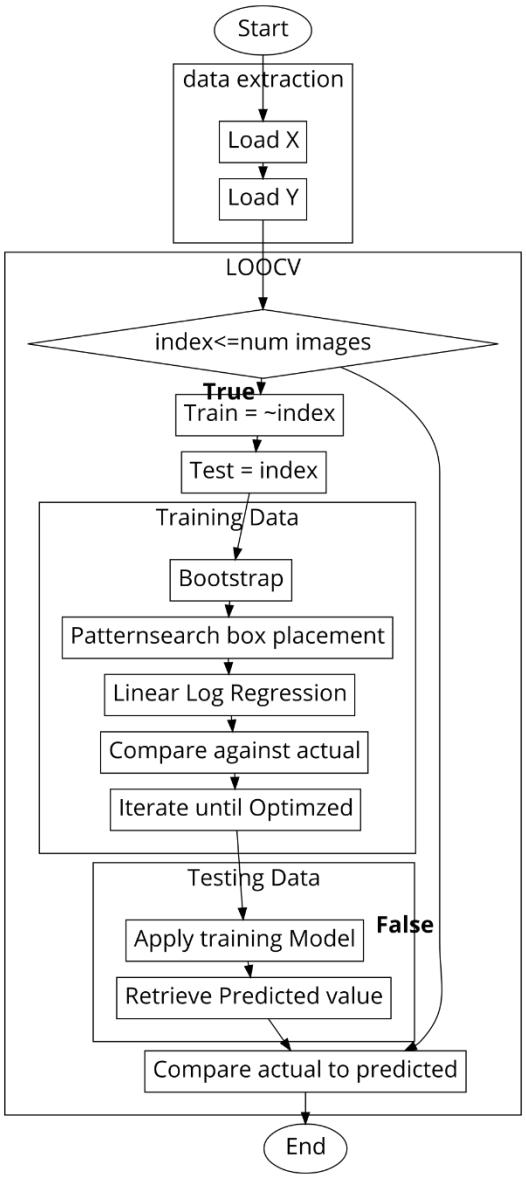

Figure 6-1. Methodology for finding optimized box placements in a cross-validated way.

The flowchart represents the steps taken to retrieve a linear regression model, developed by using training data as determined by the leave-one-out cross-validation (LOOCV), which is then tested on the testing patient. The process is repeated to cover all neonates in the dataset.

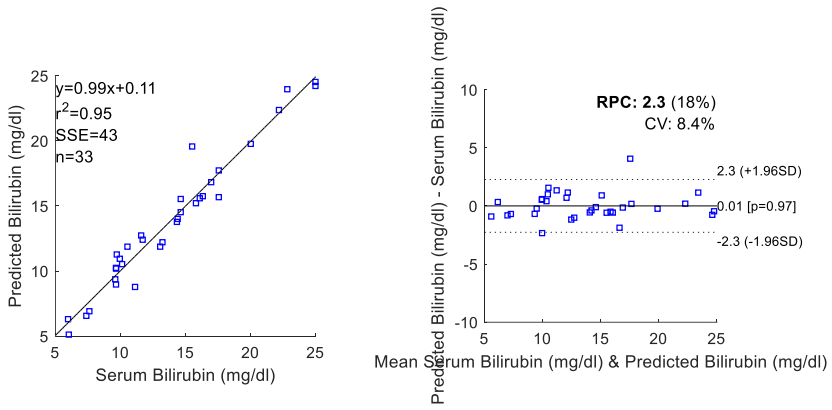

Figure 6-2. Cross-validated correlation plot (A) and Bland-Altmann plot (B) between 4-boxes taken from cellphone images, and serum bilirubin values from the neonates.

The correlation between serum bilirubin values and the predicted values are excellent for this device, and by applying a 4-box smartbox search algorithm, when compared to results from other smartphone based imaging and analysis for bilirubin [223], who reported that their correlation amongst African infants was 0.9. However, looking at the bland-altman plot, we can also see that our smartbox algorithm has 2.3 mg/dL error, whereas a similar Bland-Altman plot from Taylor [223] had a variation of 3.63 mg/dL.

The images used in Fig. 6-2. were taken from a cohort of neonates from Tanzania, Africa and were generally noted as having more pigment than a simultaneous study in the US. Even with the increased pigment, the n-box algorithm performed well in the cross-validation, with an R^2 of 0.95 among these pigmented infants. A future paper with this algorithm more deeply explained and combined data from many sites is in the works.

One of the problems with using methods such as the N-box algorithm is that it only offers a regression, which is a segmentation scheme based on having enough data in the first place. As such, this and other such schemes are limited in their approach by the number of data points, and the fidelity of these data points. Special care was taken in

identifying images in the datasets that were considered outliers, using qualitative assessments and semi-supervised local outlier detection. Allowing for an outlier image into the dataset has the potential of suggesting a regression line that is not representative of the serum bilirubin values. MC methods are relatively immune to the problems faced with using regression methods, but as described above, face their own problems which makes them difficult to implement in realistic biological tissues.

Specific Aim 2 and 3 aimed at using the fast implementation MCX from Specific Aim 1, and applying this platform to produce rich Raman spectra that were complete with effects that a user might experience with an actual spectrometer/camera setup, such as system noise and tissue autofluorescence. Validation of gelatin and HAP phantoms suggested that the model performed well in specific situations on phantoms in the lab. However, just as in Specific Aim 1, the fact that a model behaves well in the forward direction does not necessarily mean it is well-behaved in the inverse direction. The Raman model could be used in inverse calculations of optical properties but faces the same problem as the conventional MC for diffuse reflectance. Just as it is challenging to use iMC for optical diagnosis of neonatal jaundice in Aim 1, using an inverse Raman MC could be just as challenging in a clinical setting. In fact, we argue it may be harder to use inverse MC in Raman settings as the parameter being tracked are two sets of optical properties (excitation and emission) and two intrinsic coefficients (Raman and fluorescence), which all work together to produce a single output signal. This problem may be helped by considering the spatial offset in a SORS system, where different detector positions offer differential information on depth-dependent optical properties, but just as in diffuse MCs, this problem becomes overwhelming in most tissues past well-

characterized phantoms. Even so, the Raman model offered in Chapter IV presents a step forward in the direction of clinically applicable Raman MC models that can be used to determine and diagnose tissues in varied situations, offering speeds comparable to MCX. This acceleration will hopefully help in making the use of modeling in Raman spectroscopy a feasible step in designing Raman experiments and in the explanation of the underlying optical mechanics that lead to observed Raman signal.

Aim 3 used the Raman MC developed in Aim 2 to explore the bulk Raman response on the brain-air interface of a surgical cavity during surgical glioma removal. This was supposed to be fed with results from an CARS system built in the lab, however, delays in implementing said CARS system meant that the optical properties values had to be extracted from a literature review instead. We tried to fully describe the source of each of the optical properties used, however, we had no ability to validate the simulations. Even so, fast Raman MCs are so rare that even implementing theoretical scenarios was deemed appropriate. In the future, though, there is no reason not to use the CARS system to better inform Raman coefficients, which can then be validated, so that the results can be confirmed to be simulating real-life brain cancer.

CHAPTER 7 OUTPUTS AND DELIVERABLES

The work presented in this dissertation has lead to several outputs, namely in the form of published papers, or papers getting ready for publications, as well as numerous conference proceedings and oral presentations; poster presentations are not included in this section, as they are numerous amd do not represent the most impactful outputs. The outputs are listed in the following lists. Papers labeled with the tag "Submitted" have been submitted for peer-review to targeted scientific publications, documents labeled with "In Prep" have been written and have entered a state of internal reviewing between myself and Dr. Chetan Patil.

Papers

A.P. Dumont, and C.A. Patil, "Application Of Gpu Accelerated Mc Modeling Of Raman Scattering To Inform Multi-Scale Spatial Relationship Between Microscopy And Tissue Level Analyses" (In prep, *Journal of Biophotonics* IF=3.763)

A.P. Dumont, and C.A. Patil, "A Computationally Efficient Monte Carlo model for Biomedical Raman Spectroscopy" (Submitted, *Journal of Biophotonics* IF=3.763)

A.P. Dumont, B. Harrison, J. So, and C.A. Patil, "Monte-Carlo modeling of conventional andmobile phone camera based transcutaneousbilirubinometry in pigmented infants" (Submitted, *Biomedical Optics Express* IF=3.910)

Shanas, N. A., Querido, W., Dumont, A., Yonko, E., Carter, E., Ok, J., ... & Raggio, C. (2020). Clinical application of near infrared fiber optic spectroscopy for noninvasive bone assessment. *Journal of Biophotonics*, e201960172.

Dumont, A. P., & Patil, C. (2018, February). Development of accelerated Raman and fluorescent Monte Carlo method. In *Biomedical Vibrational Spectroscopy 2018: Advances in Research and Industry* (Vol. 10490, p. 104900P). International Society for Optics and Photonics.

Dumont, A. P., Harrison, B., McCormick, Z. T., Kumar, N. G., & Patil, C. A. (2017, March). Development of mobile phone based transcutaneous billirubinometry.

In *Optics and Biophotonics in Low-Resource Settings III* (Vol. 10055, p. 100550T). International Society for Optics and Photonics.

Oral Presentations

Dumont, A. P., & Patil, C. (2018, February). Development of accelerated Raman and fluorescent Monte Carlo method. In *Biomedical Vibrational Spectroscopy 2018: Advances in Research and Industry* (Vol. 10490, p. 104900P). International Society for Optics and Photonics.

Dumont, A. P., Harrison, B., McCormick, Z. T., Kumar, N. G., & Patil, C. A. (2017, March). Development of mobile phone based transcutaneous billirubinometry. In *Optics and Biophotonics in Low-Resource Settings III* (Vol. 10055, p. 100550T). International Society for Optics and Photonics.

REFERENCES

1. Tuchin, V.V., *Tissue optics and photonics: biological tissue structures.* Journal of Biomedical Photonics & Engineering, 2015. **1**(1).

2. Ashish, *why does the sun reflect off seas and oceans*. 2016, ScienceABC.

3. Beard, P., *Biomedical photoacoustic imaging.* Interface focus, 2011. **1**(4): p. 602-631.

4. Wang, L.V., *Photoacoustic imaging and spectroscopy*. 2009: CRC press.

5. Xu, M. and L.V. Wang, *Photoacoustic imaging in biomedicine.* Review of scientific instruments, 2006. **77**(4): p. 041101.

6. Hoelen, C., et al., *Three-dimensional photoacoustic imaging of blood vessels in tissue.* Optics letters, 1998. **23**(8): p. 648-650.

7. Tuchin, V.V., *Tissue optics and photonics: light-tissue interaction.* Journal of Biomedical Photonics & Engineering, 2015. **1**(2).

8. Tuchin, V., *Tissue optics and photonics: Light-tissue interaction II.* Journal of Biomedical Photonics and Engineering, 2016. **2**(3): p. 030201.

9. Mie, G., *Beiträge zur Optik trüber Medien, speziell kolloidaler Metallösungen.* Annalen der physik, 1908. **330**(3): p. 377-445.

10. Henyey, L.G. and J.L. Greenstein, *Diffuse radiation in the galaxy.* The Astrophysical Journal, 1941. **93**: p. 70-83.

11. Mahadevan-Jansen, A., C.A. Patil, and I.J. Pence, *Raman spectroscopy: from benchtop to bedside*, in *Biomedical photonics handbook.* 2014, CRC Press. p. 782-825.

12. Mahadevan-Jansen, A., *Raman spectroscopy: from benchtop to bedside.* Biomedical Photonics Handbook, 2003.

13. Ferraro, J.R., *Introductory raman spectroscopy*. 2003: Elsevier.

14. Morris, M.D. and G.S. Mandair, *Raman assessment of bone quality.* Clinical Orthopaedics and Related Research®, 2011. **469**(8): p. 2160-2169.

15. Guilbault, G.G., *Practical fluorescence*. Vol. 3. 1990: CRC Press.

16. Masters, B.R., *Principles of fluorescence spectroscopy.* Journal of Biomedical Optics, 2008. **13**(2): p. 029901.

17. Vo-Dinh, T. and B.M. Cullum, *Fluorescence spectroscopy for biomedical diagnostics*, in *Biomedical photonics handbook*. 2014, CRC Press. p. 508-565.

18. Abramowitz, M. and M. Davidson, *Overview of Fluorescence Excitation and Emission Fundamentals*. olympus lifescience.

19. Proksch, E., J.M. Brandner, and J.M. Jensen, *The skin: an indispensable barrier.* Experimental dermatology, 2008. **17**(12): p. 1063-1072.

20. Tortora, G.J. and B.H. Derrickson, *Principles of anatomy and physiology*. 2018: John Wiley & Sons.

21. Lai-Cheong, J.E. and J.A. McGrath, *Structure and function of skin, hair and nails.* Medicine, 2013. **41**(6): p. 317-320.

22. *Skin*. 2009: www.seer.cancer.gov.

23. Slomianka, L., *INTEGUMENTARY SYSTEM*. 2009: T**he University of Western Australia**.

24. Baroni, A., et al., *Structure and function of the epidermis related to barrier properties.* Clinics in dermatology, 2012. **30**(3): p. 257-262.

25. Werner, Y. and M. Lindberg, *Transepidermal water loss in dry and clinically normal skin in patients with atopic dermatitis.* Acta dermato-venereologica, 1985. **65**(2): p. 102-105.

26. Sandby-Moller, J., T. Poulsen, and H.C. Wulf, *Epidermal thickness at different body sites: relationship to age, gender, pigmentation, blood content, skin type and smoking habits.* Acta Dermato Venereologica, 2003. **83**(6): p. 410-413.

27. Oranges, T., V. Dini, and M. Romanelli, *Skin physiology of the neonate and infant: clinical implications.* Advances in wound care, 2015. **4**(10): p. 587-595.

28. Stamatas, G.N., et al., *Infant skin microstructure assessed in vivo differs from adult skin in organization and at the cellular level.* Pediatric dermatology, 2010. **27**(2): p. 125-131.

29. Gniadecka, M., et al., *Water and protein structure in photoaged and chronically aged skin.* Journal of investigative dermatology, 1998. **111**(6): p. 1129-1133.

30. Hwang, K., H. Kim, and D.J. Kim, *Thickness of skin and subcutaneous tissue of the free flap donor sites: a histologic study.* Microsurgery, 2016. **36**(1): p. 54-58.

31. Kita, N. *The Hypodermis Layer of the Skin Structure and Function*. The Anatomy and Physiology of the Subcutaneous Layer of the Skin 2020.

32. Philips, H., *Introduction: The human brain.* New Scientist, 2006. **4**.

33. Hodos, W., *Evolution of cerebellum.* Encyclopedia of neuroscience, 2009: p. 1240-1243.

34. Haines, D.E. and G.A. Mihailoff, *Fundamental Neuroscience for Basic and Clinical Applications E-Book*. 2017: Elsevier Health Sciences.

35. *Adult Central Nervous System Tumors Treatment (PDQ®)–Patient Version*. 2019.

36. *The Life of a Brain Tumor: How Does Glioblastoma Grow?* 2018.

37. Jacques, S. *Optical Absorption of Melanin*. Available from: https://omlc.org/spectra/melanin/.

38. Bashkatov, A.N., et al. *Optical properties of melanin in the skin and skinlike phantoms*. in *Controlling tissue optical properties: applications in clinical study*. 2000. International Society for Optics and Photonics.

39. Zonios, G., J. Bykowski, and N. Kollias, *Skin melanin, hemoglobin, and light scattering properties can be quantitatively assessed in vivo using diffuse reflectance spectroscopy.* Journal of Investigative Dermatology, 2001. **117**(6): p. 1452-1457.

40. Jacques, S.L., R.D. Glickman, and J.A. Schwartz. *Internal absorption coefficient and threshold for pulsed laser disruption of melanosomes isolated from retinal pigment epithelium*. in *Laser-Tissue Interaction VII*. 1996. International Society for Optics and Photonics.

41. Steven, L.J., *Optical properties of biological tissue: a review.* Phys Med Biol, 2013. **58**(11): p. R37.

42. Cunningham, A., *Physiological jaundice.* Archives of disease in childhood, 1959. **34**(175): p. 262.

43. Tiker, F., et al., *Extreme hyperbilirubinemia in newborn infants.* Clinical pediatrics, 2006. **45**(3): p. 257-261.

44. DAVIDSON, L.T., K.K. MERRITT, and A.A. WEECH, *Hyperbilirubinemia in the newborn.* American Journal of Diseases of Children, 1941. **61**(5): p. 958-980.

45. Porter, M.L. and M.B.L. Dennis, *Hyperbilirubinemia in the term newborn.* American family physician, 2002. **65**(4): p. 599.

46. Dennery, P.A., D.S. Seidman, and D.K. Stevenson, *Neonatal hyperbilirubinemia.* New England Journal of Medicine, 2001. **344**(8): p. 581-590.

47. Huang, M.-J., et al., *Risk factors for severe hyperbilirubinemia in neonates.* Pediatric research, 2004. **56**(5): p. 682-689.

48. Prahl, S. *Optical Absorption of Hemoglobin*. 1999.

49. Michels, R., F. Foschum, and A. Kienle, *Optical properties of fat emulsions.* Optics express, 2008. **16**(8): p. 5907-5925.

50. Van Staveren, H.J., et al., *Light scattering in lntralipid-10% in the wavelength range of 400–1100 nm.* Applied optics, 1991. **30**(31): p. 4507-4514.

51. Bashkatov, A., et al., *Optical properties of human skin, subcutaneous and mucous tissues in the wavelength range from 400 to 2000 nm.* Journal of Physics D: Applied Physics, 2005. **38**(15): p. 2543.

52. Jacques, S.L., C. Alter, and S.A. Prahl, *Angular dependence of HeNe laser light scattering by human dermis.* Lasers Life Sci, 1987. **1**(4): p. 309-333.

53. Hall, G., et al., *Goniometric measurements of thick tissue using Monte Carlo simulations to obtain the single scattering anisotropy coefficient.* Biomedical optics express, 2012. **3**(11): p. 2707-2719.

54. Lister, T., P.A. Wright, and P.H. Chappell, *Optical properties of human skin.* Journal of biomedical optics, 2012. **17**(9): p. 090901.

55. Mourant, J.R., et al., *Mechanisms of light scattering from biological cells relevant to noninvasive optical-tissue diagnostics.* Applied optics, 1998. **37**(16): p. 3586-3593.

56. Graaff, R., et al., *Reduced light-scattering properties for mixtures of spherical particles: a simple approximation derived from Mie calculations.* Applied optics, 1992. **31**(10): p. 1370-1376.

57. Saidi, I.S., S.L. Jacques, and F.K. Tittel, *Mie and Rayleigh modeling of visible-light scattering in neonatal skin.* Applied optics, 1995. **34**(31): p. 7410-7418.

58. Beck, T.J., et al. *Clinical determination of tissue optical properties in vivo by spatially resolved reflectance measurements*. in *European Conference on Biomedical Optics*. 2003. Optical Society of America.

59. Zhao, J., et al., *In vivo determination of the optical properties of infant brain using frequency-domain near-infrared spectroscopy.* Journal of biomedical optics, 2005. **10**(2): p. 024028.

60. Yaroslavsky, A., et al., *Optical properties of selected native and coagulated human brain tissues in vitro in the visible and near infrared spectral range.* Physics in Medicine & Biology, 2002. **47**(12): p. 2059.

61. Cheong, W.-F., S.A. Prahl, and A.J. Welch, *A review of the optical properties of biological tissues.* IEEE journal of quantum electronics, 1990. **26**(12): p. 2166-2185.

62. Bashkatov, A.N., E.A. Genina, and V.V. Tuchin, *Optical properties of skin, subcutaneous, and muscle tissues: a review.* Journal of Innovative Optical Health Sciences, 2011. **4**(01): p. 9-38.

63. Wang, L.V. and H.-i. Wu, *Biomedical optics: principles and imaging*. 2012: John Wiley & Sons.

64. Chandrasekhar, S., *Radiative transfer*. 2013: Courier Corporation.

65. Dullemond, C.P., *What makes radiative transfer hard, and how to solve it - An introduction* in *Radiative transfer in astrophysics (Master/PhD Course)*. 2012.

66. Joseph, J.H., W. Wiscombe, and J. Weinman, *The delta-Eddington approximation for radiative flux transfer.* Journal of the Atmospheric Sciences, 1976. **33**(12): p. 2452-2459.

67. Sloan, P.-P. *Stupid spherical harmonics (sh) tricks*. in *Game developers conference*. 2008. Citeseer.

68. Humi, M., *Factorisation of separable partial differential equations.* Journal of Physics A: Mathematical and General, 1987. **20**(14): p. 4577.

69. Weisstein, E.W., *Spherical harmonic.* 2004.

70. Fick, A., *Ueber diffusion.* Annalen der Physik, 1855. **170**(1): p. 59-86.

71. Patterson, M.S., B. Chance, and B.C. Wilson, *Time resolved reflectance and transmittance for the noninvasive measurement of tissue optical properties.* Applied optics, 1989. **28**(12): p. 2331-2336.

72. Martí-López, L., J. Bouza-Domínguez, and J.C. Hebden, *Interpretation of the failure of the time-independent diffusion equation near a point source.* Optics Communications, 2004. **242**(1-3): p. 23-43.

73. Martelli, F., et al., *Accuracy of the diffusion equation to describe photon migration through an infinite medium: numerical and experimental investigation.* Physics in Medicine & Biology, 2000. **45**(5): p. 1359.

74. Duffy, D.J. and J. Kienitz, *Monte Carlo Frameworks: Building Customisable High-Performance C++ Applications*. Vol. 406. 2009: John Wiley & Sons.

75. Shah, M., D. Vaidya, and A. Sircar, *Using Monte Carlo simulation to estimate geothermal resource in Dholera geothermal field, Gujarat, India.* Multiscale and Multidisciplinary Modeling, Experiments and Design, 2018: p. 1-13.

76. Eckhardt, R., *Stan ulam, john von neumann, and the monte carlo method.* Los Alamos Science, 1987. **15**(131-136): p. 30.

77. Caffarel, M. and P. Claverie, *Development of a pure diffusion quantum Monte Carlo method using a full generalized Feynman–Kac formula. I. Formalism.* The Journal of chemical physics, 1988. **88**(2): p. 1088-1099.

78. de la Fuente Marcos, C. and R. de la Fuente Marcos, *Finding Planet Nine: a Monte Carlo approach.* Monthly Notices of the Royal Astronomical Society: Letters, 2016. **459**(1): p. L66-L70.

79. Harrison, R.L. *Introduction to monte carlo simulation*. in *AIP conference proceedings*. 2010. AIP.

80. Wilson, B. and G. Adam, *A Monte Carlo model for the absorption and flux distributions of light in tissue.* Medical physics, 1983. **10**(6): p. 824-830.

81. Keijzer, M., et al., *Light distributions in artery tissue: Monte Carlo simulations for finite-diameter laser beams.* Lasers in surgery and medicine, 1989. **9**(2): p. 148-154.

82. Wang, L., S.L. Jacques, and L. Zheng, *MCML—Monte Carlo modeling of light transport in multi-layered tissues.* Computer methods and programs in biomedicine, 1995. **47**(2): p. 131-146.

83. Carter, L.L. and E.D. Cashwell, *Particle-transport simulation with the Monte Carlo method*. 1975, Los Alamos Scientific Lab.

84. Atencio, J.D., S. Jacques, and S.V. y Montiel, *Monte Carlo modeling of light propagation in neonatal skin*, in *Applications of Monte Carlo Methods in Biology, Medicine and Other Fields of Science*. 2011, InTech.

85. Wang, L.V., R.E. Nordquist, and W.R. Chen, *Optimal beam size for light delivery to absorption-enhanced tumors buried in biological tissues and effect of multiple-beam delivery: a Monte Carlo study.* Applied optics, 1997. **36**(31): p. 8286-8291.

86. Zhu, C. and Q. Liu, *Validity of the semi-infinite tumor model in diffuse reflectance spectroscopy for epithelial cancer diagnosis: a Monte Carlo study.* Optics Express, 2011. **19**(18): p. 17799-17812.

87. Zhu, C. and Q. Liu, *Hybrid method for fast Monte Carlo simulation of diffuse reflectance from a multilayered tissue model with tumor-like heterogeneities.* Journal of biomedical optics, 2012. **17**(1): p. 010501.

88. Selb, J., et al., *Comparison of a layered slab and an atlas head model for Monte Carlo fitting of time-domain near-infrared spectroscopy data of the adult head.* Journal of biomedical optics, 2014. **19**(1): p. 016010-016010.

89. Fang, Q. and D.A. Boas, *Monte Carlo simulation of photon migration in 3D turbid media accelerated by graphics processing units.* Optics express, 2009. **17**(22): p. 20178-20190.

90. Boas, D.A., et al., *Three dimensional Monte Carlo code for photon migration through complex heterogeneous media including the adult human head.* Optics express, 2002. **10**(3): p. 159-170.

91. Keijzer, M., et al., *Fluorescence spectroscopy of turbid media: autofluorescence of the human aorta.* Applied Optics, 1989. **28**(20): p. 4286-4292.

92. Zeng, H., et al., *Reconstruction of in vivo skin autofluorescence spectrum from microscopic properties by Monte Carlo simulation.* Journal of Photochemistry and Photobiology B: Biology, 1997. **38**(2-3): p. 234-240.

93. Lui, H., et al., *Real-time Raman spectroscopy for in vivo skin cancer diagnosis.* Cancer research, 2012. **72**(10): p. 2491-2500.

94. Wang, S., et al., *Monte Carlo simulation of near infrared autofluorescence measurements of in vivo skin.* Journal of Photochemistry and Photobiology B: Biology, 2011. **105**(3): p. 183-189.

95. Liu, Q., C. Zhu, and N. Ramanujam, *Experimental validation of Monte Carlo modeling of fluorescence in tissues in the UV-visible spectrum.* Journal of biomedical optics, 2003. **8**(2): p. 223-237.

96. Vishwanath, K. and M.-A. Mycek, *Time-resolved photon migration in bi-layered tissue models.* Optics Express, 2005. **13**(19): p. 7466-7482.

97. Pfefer, T.J., et al., *Multiple-fiber probe design for fluorescence spectroscopy in tissue.* Applied Optics, 2002. **41**(22): p. 4712-4721.

98. Matousek, P., et al., *Numerical simulations of subsurface probing in diffusely scattering media using spatially offset Raman spectroscopy.* Applied spectroscopy, 2005. **59**(12): p. 1485-1492.

99. Matousek, P., et al., *Subsurface probing in diffusely scattering media using spatially offset Raman spectroscopy.* Applied spectroscopy, 2005. **59**(4): p. 393-400.

100. Everall, N., et al., *Photon migration in Raman spectroscopy.* Applied spectroscopy, 2004. **58**(5): p. 591-597.

101. Everall, N., et al., *Picosecond time-resolved Raman spectroscopy of solids: capabilities and limitations for fluorescence rejection and the influence of diffuse reflectance.* Applied spectroscopy, 2001. **55**(12): p. 1701-1708.

102. Keller, M.D., et al., *Monte Carlo model of spatially offset Raman spectroscopy for breast tumor margin analysis.* Applied spectroscopy, 2010. **64**(6): p. 607-614.

103. Wang, S., et al., *Monte Carlo simulation of in vivo Raman spectral Measurements of human skin with a multi-layered tissue optical model.* Journal of biophotonics, 2014. **7**(9): p. 703-712.

104. Periyasamy, V., et al., *Experimentally validated Raman Monte Carlo simulation for a cuboid object to obtain Raman spectroscopic signatures for hidden material.* Journal of Raman Spectroscopy, 2015. **46**(7): p. 669-676.

105. Periyasamy, V. and M. Pramanik, *Monte Carlo simulation of light transport in turbid medium with embedded object—spherical, cylindrical, ellipsoidal, or cuboidal objects embedded within multilayered tissues.* Journal of biomedical optics, 2014. **19**(4): p. 045003.

106. Reble, C., et al., *Influence of tissue absorption and scattering on the depth dependent sensitivity of Raman fiber probes investigated by Monte Carlo simulations.* Biomedical optics express, 2011. **2**(3): p. 520-533.

107. Zhu, C. and Q. Liu, *Review of Monte Carlo modeling of light transport in tissues.* Journal of Biomedical Optics, 2013. **18**(5): p. 050902.

108. Periyasamy, V. and M. Pramanik, *Advances in Monte Carlo simulation for light propagation in tissue.* IEEE reviews in biomedical engineering, 2017. **10**: p. 122-135.

109. Khan, S.U., A.Y. Zomaya, and A. Abbas, *Handbook of Large-Scale Distributed Computing in Smart Healthcare*. 2017: Springer.

110. Graaff, R., et al., *Condensed Monte Carlo simulations for the description of light transport.* Applied optics, 1993. **32**(4): p. 426-434.

111. Liu, Q. and N. Ramanujam, *Scaling method for fast Monte Carlo simulation of diffuse reflectance spectra from multilayered turbid media.* JOSA A, 2007. **24**(4): p. 1011-1025.

112. Pifferi, A., et al., *Real-time method for fitting time-resolved reflectance and transmittance measurements with a Monte Carlo model.* Applied optics, 1998. **37**(13): p. 2774-2780.

113. Kato, T., *Perturbation theory for linear operators*. Vol. 132. 2013: Springer Science & Business Media.

114. Sassaroli, A., *Fast perturbation Monte Carlo method for photon migration in heterogeneous turbid media.* Optics letters, 2011. **36**(11): p. 2095-2097.

115. Kumar, Y.P. and R.M. Vasu, *Reconstruction of optical properties of low-scattering tissue using derivative estimated through perturbation Monte-Carlo method.* Journal of biomedical optics, 2004. **9**(5): p. 1002-1013.

116. Yalavarthy, P.K., et al., *Experimental investigation of perturbation Monte-Carlo based derivative estimation for imaging low-scattering tissue.* Optics express, 2005. **13**(3): p. 985-997.

117. Seo, I., et al., *Perturbation and differential Monte Carlo methods for measurement of optical properties in a layered epithelial tissue model.* Journal of biomedical optics, 2007. **12**(1): p. 014030.

118. Hendricks, J. and T. Booth, *MCNP variance reduction overview*, in *Monte-Carlo Methods and Applications in Neutronics, Photonics and Statistical Physics*. 1985, Springer. p. 83-92.

119. Botev, Z. and A. Ridder, *Variance reduction.* Wiley StatsRef: Statistics Reference Online, 2014: p. 1-6.

120. Alerstam, E., T. Svensson, and S. Andersson-Engels, *CUDAMCML-User manual and implementation notes.* Lund University, Lund, 2009.

121. Bernat, A.S., et al. *Assessing changes in oxygen saturation using a low cost multi-spectral imaging system*. in *Optics and Biophotonics in Low-Resource Settings V*. 2019. International Society for Optics and Photonics.

122. Duperron, M., et al., *Diffuse reflectance spectroscopy-enhanced drill for bone boundary detection.* Biomedical optics express, 2019. **10**(2): p. 961-977.

123. Gunther, J., et al. *Modelling light propagation for fetal monitoring in utero*. in *European Conference on Biomedical Optics*. 2019. Optical Society of America.

124. Sowers, T., H. Yoon, and S. Emelianov, *Investigation of light delivery geometries for photoacoustic applications using Monte Carlo simulations with multiple wavelengths, tissue types, and species characteristics.* Journal of Biomedical Optics, 2020. **25**(1): p. 016005.

125. Wojtkiewicz, S., et al., *Self-calibrating time-resolved near infrared spectroscopy.* Biomedical optics express, 2019. **10**(5): p. 2657-2669.

126. Shekhar, S., et al., *Hemodynamic responses to emotional speech in two-month-old infants imaged using diffuse optical tomography.* Scientific reports, 2019. **9**(1): p. 1-15.

127. Huang, D., et al., *Optical coherence tomography.* science, 1991. **254**(5035): p. 1178-1181.

128. Hsieh, Y.-S., et al., *Dental optical coherence tomography.* Sensors, 2013. **13**(7): p. 8928-8949.

129. Chinn, S., E. Swanson, and J. Fujimoto, *Optical coherence tomography using a frequency-tunable optical source.* Optics letters, 1997. **22**(5): p. 340-342.

130. Alamouti, B. and J. Funk, *Retinal thickness decreases with age: an OCT study.* British journal of ophthalmology, 2003. **87**(7): p. 899-901.

131. Zotter, S., et al., *Large-field high-speed polarization sensitive spectral domain OCT and its applications in ophthalmology.* Biomedical optics express, 2012. **3**(11): p. 2720-2732.

132. Fujimoto, J.G., et al., *Optical Coherence Tomography (OCT) in ophthalmology: introduction.* Optics express, 2009. **17**(5): p. 3978-3979.

133. Rebolleda, G., et al., *OCT: new perspectives in neuro-ophthalmology.* Saudi Journal of Ophthalmology, 2015. **29**(1): p. 9-25.

134. Barlis, P., J. Tanigawa, and C. Di Mario, *Coronary bioabsorbable magnesium stent: 15-month intravascular ultrasound and optical coherence tomography findings.* European heart journal, 2007. **28**(19): p. 2319-2319.

135. Schmitt, J., D. Kolstad, and C. Petersen, *Intravascular Optical Coherence Tomography—Opening a Window into Coronary Artery Disease.* LightLab Imaging, Inc. Business Briefing: European Cardiology, 2005.

136. Vignali, L., E. Solinas, and E. Emanuele, *Research and clinical applications of optical coherence tomography in invasive cardiology: a review.* Current cardiology reviews, 2014. **10**(4): p. 369-376.

137. Rosenfeld, P.J., A.E. Fung, and C.A. Puliafito, *Optical coherence tomography findings after an intravitreal injection of bevacizumab (Avastin®) for macular edema from central retinal vein occlusion.* Ophthalmic Surgery, Lasers and Imaging Retina, 2005. **36**(4): p. 336-339.

138. Manyak, M.J., et al., *Evaluation of superficial bladder transitional-cell carcinoma by optical coherence tomography.* Journal of endourology, 2005. **19**(5): p. 570-574.

139. Escobar, P., et al., *Diagnostic efficacy of optical coherence tomography in the management of preinvasive and invasive cancer of uterine cervix and vulva.* International Journal of Gynecological Cancer, 2004. **14**(3): p. 470-474.

140. Chen, Y.-C., et al., *Oct-4 expression maintained cancer stem-like properties in lung cancer-derived CD133-positive cells.* PloS one, 2008. **3**(7).

141. Sergeev, A.M., et al., *In vivo endoscopic OCT imaging of precancer and cancer states of human mucosa.* Optics express, 1997. **1**(13): p. 432-440.

142. Pierce, M.C., et al., *Advances in optical coherence tomography imaging for dermatology.* Journal of investigative dermatology, 2004. **123**(3): p. 458-463.

143. Gambichler, T., et al., *Applications of optical coherence tomography in dermatology.* Journal of dermatological science, 2005. **40**(2): p. 85-94.

144. Welzel, J., *Optical coherence tomography in dermatology: a review.* Skin Research and Technology: Review article, 2001. **7**(1): p. 1-9.

145. Paul, C. *What is Confocal Laser Scanning Microscopy?*

146. Marvin, M., *Microscopy apparatus*. 1961, Google Patents.

147. Rezakhaniha, R., et al., *Experimental investigation of collagen waviness and orientation in the arterial adventitia using confocal laser scanning microscopy.* Biomechanics and modeling in mechanobiology, 2012. **11**(3-4): p. 461-473.

148. Gerger, A., et al., *Diagnostic applicability of in vivo confocal laser scanning microscopy in melanocytic skin tumors.* Journal of Investigative Dermatology, 2005. **124**(3): p. 493-498.

149. Boas, D.A., C. Pitris, and N. Ramanujam, *Handbook of biomedical optics*. 2016: CRC press.

150. Arridge, S.R. and M. Schweiger, *Image reconstruction in optical tomography.* Philosophical Transactions of the Royal Society of London. Series B: Biological Sciences, 1997. **352**(1354): p. 717-726.

151. Hoshi, Y. and Y. Yamada, *Overview of diffuse optical tomography and its clinical applications.* Journal of biomedical optics, 2016. **21**(9): p. 091312.

152. Lee, C.W., R.J. Cooper, and T. Austin, *Diffuse optical tomography to investigate the newborn brain.* Pediatric research, 2017. **82**(3): p. 376.

153. Cuccia, D.J. *Spatial frequency domain imaging (SFDI): a technology overview and validation of an LED-based clinic friendly device*. in *Emerging Digital*

Micromirror Device Based Systems and Applications IV. 2012. International Society for Optics and Photonics.

154. Nguyen, J.Q.M., et al., *Spatial frequency domain imaging of burn wounds in a preclinical model of graded burn severity.* Journal of biomedical optics, 2013. **18**(6): p. 066010.

155. Laughney, A.M., et al., *Spectral discrimination of breast pathologies in situusing spatial frequency domain imaging.* Breast Cancer Research, 2013. **15**(4): p. R61.

156. Fishkin, J.B., et al., *Frequency-domain photon migration measurements of normal and malignant tissue optical properties in a human subject.* Applied optics, 1997. **36**(1): p. 10-20.

157. Tromberg, B.J., et al., *Non–invasive measurements of breast tissue optical properties using frequency–domain photon migration.* Philosophical Transactions of the Royal Society of London. Series B: Biological Sciences, 1997. **352**(1354): p. 661-668.

158. Stone, N. and P. Matousek, *Advanced transmission Raman spectroscopy: a promising tool for breast disease diagnosis.* Cancer Research, 2008. **68**(11): p. 4424-4430.

159. Haka, A.S., et al., *Diagnosing breast cancer by using Raman spectroscopy.* Proceedings of the National Academy of Sciences of the United States of America, 2005. **102**(35): p. 12371-12376.

160. Haka, A.S., et al., *In vivo margin assessment during partial mastectomy breast surgery using Raman spectroscopy.* Cancer research, 2006. **66**(6): p. 3317-3322.

161. Desroches, J., et al., *Characterization of a Raman spectroscopy probe system for intraoperative brain tissue classification.* Biomedical optics express, 2015. **6**(7): p. 2380-2397.

162. Jermyn, M., et al., *Intraoperative brain cancer detection with Raman spectroscopy in humans.* Science translational medicine, 2015. **7**(274): p. 274ra19-274ra19.

163. Kirsch, M., et al., *Raman spectroscopic imaging for in vivo detection of cerebral brain metastases.* Analytical and bioanalytical chemistry, 2010. **398**(4): p. 1707-1713.

164. Jermyn, M., et al., *Raman spectroscopy detects distant invasive brain cancer cells centimeters beyond MRI capability in humans.* Biomedical optics express, 2016. **7**(12): p. 5129-5137.

165. Huang, Z., et al., *Near-infrared Raman spectroscopy for optical diagnosis of lung cancer.* International journal of cancer, 2003. **107**(6): p. 1047-1052.

166. Caspers, P.J., G.W. Lucassen, and G.J. Puppels, *Combined in vivo confocal Raman spectroscopy and confocal microscopy of human skin.* Biophysical journal, 2003. **85**(1): p. 572-580.

167. Caspers, P., et al., *In vitro and in vivo Raman spectroscopy of human skin.* Biospectroscopy, 1998. **4**(S5): p. S31-S39.

168. Mahadevan-Jansen, A., et al., *Near-Infrared Raman Spectroscopy for In Vitro Detection of Cervical Precancers.* Photochemistry and photobiology, 1998. **68**(1): p. 123-132.

169. Lieber, C.A. and A. Mahadevan-Jansen, *Automated method for subtraction of fluorescence from biological Raman spectra.* Applied spectroscopy, 2003. **57**(11): p. 1363-1367.

170. Zhang, D. and D. Ben-Amotz, *Enhanced chemical classification of Raman images in the presence of strong fluorescence interference.* Applied Spectroscopy, 2000. **54**(9): p. 1379-1383.

171. Mosier-Boss, P., S. Lieberman, and R. Newbery, *Fluorescence rejection in Raman spectroscopy by shifted-spectra, edge detection, and FFT filtering techniques.* Applied Spectroscopy, 1995. **49**(5): p. 630-638.

172. Wang, T. and L. Dai, *Background Subtraction of Raman Spectra Based on Iterative Polynomial Smoothing.* Applied spectroscopy, 2017. **71**(6): p. 1169-1179.

173. Zhao, J., et al., *Automated autofluorescence background subtraction algorithm for biomedical Raman spectroscopy.* Applied spectroscopy, 2007. **61**(11): p. 1225-1232.

174. Zhao, J., M.M. Carrabba, and F.S. Allen, *Automated fluorescence rejection using shifted excitation Raman difference spectroscopy.* Applied Spectroscopy, 2002. **56**(7): p. 834-845.

175. Van Duyne, R.P., D.L. Jeanmaire, and D. Shriver, *Mode-locked laser Raman spectroscopy. New technique for the rejection of interfering background luminescence signals.* Analytical Chemistry, 1974. **46**(2): p. 213-222.

176. Patil, C.A., et al., *1064 nm dispersive Raman spectroscopy of tissues with strong near-infrared autofluorescence.* Optics letters, 2014. **39**(2): p. 303-306.

177. Pence, I.J., et al., *Discrimination of liver malignancies with 1064 nm dispersive Raman spectroscopy.* Biomedical optics express, 2015. **6**(8): p. 2724-2737.

178. Haifler, M., et al., *Discrimination of malignant and normal kidney tissue with short wave infrared dispersive Raman spectroscopy.* Journal of biophotonics, 2018. **11**(6): p. e201700188.

179. Evans, C.L. and X.S. Xie, *Coherent anti-Stokes Raman scattering microscopy: chemical imaging for biology and medicine.* Annu. Rev. Anal. Chem., 2008. **1**: p. 883-909.

180. Camp Jr, C.H., et al., *High-speed coherent Raman fingerprint imaging of biological tissues.* Nature photonics, 2014. **8**(8): p. 627.

181. Eliasson, C. and P. Matousek, *Noninvasive authentication of pharmaceutical products through packaging using spatially offset Raman spectroscopy.* Analytical Chemistry, 2007. **79**(4): p. 1696-1701.

182. Yuen, J.M., et al., *Transcutaneous glucose sensing by surface-enhanced spatially offset Raman spectroscopy in a rat model.* Analytical chemistry, 2010. **82**(20): p. 8382-8385.

183. Keller, M.D., et al., *Development of a spatially offset Raman spectroscopy probe for breast tumor surgical margin evaluation.* Journal of biomedical optics, 2011. **16**(7): p. 077006.

184. Camp, C.H., Y.J. Lee, and M.T. Cicerone, *Quantitative, comparable coherent anti-Stokes Raman scattering (CARS) spectroscopy: correcting errors in phase retrieval.* Journal of Raman Spectroscopy, 2016. **47**(4): p. 408-415.

185. Cheng, J.-X. and X.S. Xie, *Coherent anti-Stokes Raman scattering microscopy: instrumentation, theory, and applications*. 2004, ACS Publications.

186. Freudiger, C.W., et al., *Label-free biomedical imaging with high sensitivity by stimulated Raman scattering microscopy.* Science, 2008. **322**(5909): p. 1857-1861.

187. Benabid, F., et al., *Stimulated Raman scattering in hydrogen-filled hollow-core photonic crystal fiber.* Science, 2002. **298**(5592): p. 399-402.

188. Saar, B.G., et al., *Video-rate molecular imaging in vivo with stimulated Raman scattering.* science, 2010. **330**(6009): p. 1368-1370.

189. Matsumura, K., et al., *Deletion of chromosome 17p loci in breast cancer cells detected by fluorescence in situ hybridization.* Cancer research, 1992. **52**(12): p. 3474-3477.

190. He, H., C. Xie, and J. Ren, *Nonbleaching fluorescence of gold nanoparticles and its applications in cancer cell imaging.* Analytical chemistry, 2008. **80**(15): p. 5951-5957.

191. Urano, Y., et al., *Selective molecular imaging of viable cancer cells with pH-activatable fluorescence probes.* Nature medicine, 2009. **15**(1): p. 104.

192. Stummer, W., et al., *Fluorescence-guided surgery with 5-aminolevulinic acid for resection of malignant glioma: a randomised controlled multicentre phase III trial.* The lancet oncology, 2006. **7**(5): p. 392-401.

193. Volynskaya, Z., et al., *Diagnosing breast cancer using diffuse reflectance spectroscopy and intrinsic fluorescence spectroscopy.* Journal of biomedical optics, 2008. **13**(2): p. 024012-024012-9.

194. De Beule, P., et al., *A hyperspectral fluorescence lifetime probe for skin cancer diagnosis.* Review of scientific instruments, 2007. **78**(12): p. 123101.

195. Haifler, M., et al. *SWIR dispersive Raman spectroscopy for discrimination of normal and malignant kidney tissue (Conference Presentation)*. in *Therapeutics and Diagnostics in Urology: Lasers, Robotics, Minimally Invasive, and Advanced Biomedical Devices*. 2017. International Society for Optics and Photonics.

196. Ramanujam, N., et al., *In vivo diagnosis of cervical intraepithelial neoplasia using 337-nm-excited laser-induced fluorescence.* Proceedings of the National Academy of Sciences, 1994. **91**(21): p. 10193-10197.

197. Vo-Dinh, T., et al., *Laser-induced differential fluorescence for cancer diagnosis without biopsy.* Applied Spectroscopy, 1997. **51**(1): p. 58-63.

198. Vo-Dinh, T., M. Panjehpour, and B.F. Overholt, *Laser-induced fluorescence for esophageal cancer and dysplasia diagnosis.* Annals of the New York Academy of Sciences, 1998. **838**: p. 116-122.

199. Koenig, F., et al., *Laser induced autofluorescence diagnosis of bladder cancer.* The Journal of urology, 1996. **156**(5): p. 1597-1601.

200. Cothren, R.M., et al., *Detection of dysplasia at colonoscopy using laser-induced fluorescence: a blinded study.* Gastrointestinal Endoscopy, 1996. **44**(2): p. 168-176.

201. Schomacker, K.T., et al., *Ultraviolet laser-induced fluorescence of colonic tissue: basic biology and diagnostic potential.* Lasers in surgery and medicine, 1992. **12**(1): p. 63-78.

202. Bhutani, V.K., et al., *Noninvasive measurement of total serum bilirubin in a multiracial predischarge newborn population to assess the risk of severe hyperbilirubinemia.* Pediatrics, 2000. **106**(2): p. e17-e17.

203. Dai, J., D.M. Parry, and J. Krahn, *Transcutaneous bilirubinometry: its role in the assessment of neonatal jaundice.* Clinical biochemistry, 1997. **30**(1): p. 1-9.

204. Yamanouchi, I., Y. Yamauchi, and I. Igarashi, *Transcutaneous bilirubinometry: preliminary studies of noninvasive transcutaneous bilirubin meter in the Okayama National Hospital.* Pediatrics, 1980. **65**(2): p. 195-202.

205. Ebbesen, F., L. Rasmussen, and P. Wimberley, *A new transcutaneous bilirubinometer, BiliCheck, used in the neonatal intensive care unit and the maternity ward.* Acta Paediatrica, 2002. **91**(2): p. 203-211.

206. Yasuda, S., et al., *New transcutaneous jaundice device with two optical paths.* Journal of perinatal medicine, 2003. **31**(1): p. 81-88.

207. Hyperbilirubinemia, A.A.o.P.S.o., *Management of hyperbilirubinemia in the newborn infant 35 or more weeks of gestation.* Pediatrics, 2004. **114**(1): p. 297.

208. Johnson, L.H., V.K. Bhutani, and A.K. Brown, *System-based approach to management of neonatal jaundice and prevention of kernicterus.* The Journal of pediatrics, 2002. **140**(4): p. 396.

209. Engle, W.D., et al., *Evaluation of a transcutaneous jaundice meter following hospital discharge in term and near-term neonates.* Journal of perinatology, 2005. **25**(7): p. 486-490.

210. Maisels, M.J.a.K.E., *Transcutaneous bilirubin levels in the first 96 hours in a normal newborn population of > 35 weeks' gestation.* Pediatrics, 2006. **117**(4): p. 1169-1173.

211. Christensen, R., et al., *Causes of hemolysis in neonates with extreme hyperbilirubinemia.* Journal of Perinatology, 2014. **34**(8): p. 616.

212. Maisels, M.J., et al., *Hyperbilirubinemia in the newborn infant≥ 35 weeks' gestation: an update with clarifications.* Pediatrics, 2009. **124**(4): p. 1193-1198.

213. Bhutani, V.K., et al., *Neonatal hyperbilirubinemia and Rhesus disease of the newborn: incidence and impairment estimates for 2010 at regional and global levels.* Pediatric research, 2013. **74**(S1): p. 86-100.

214. Slusher, T.M., A. Zipursky, and V.K. Bhutani. *A global need for affordable neonatal jaundice technologies*. in *Seminars in perinatology*. 2011. Elsevier.

215. Morgan, M.C., et al., *Implementation of a neonatal transcutaneous bilirubin screening programme in rural India.* Paediatrics and international child health, 2016. **36**(2): p. 122-126.

216. Olusanya, B.O. and A.A. Emokpae, *Use of transcutaneous bilirubin to determine the need for phototherapy in resource-limited settings.* Neonatology, 2017. **111**(4): p. 324-330.

217. Maisels, M.J. and E. Kring, *Transcutaneous bilirubinometry decreases the need for serum bilirubin measurements and saves money.* Pediatrics, 1997. **99**(4): p. 599-600.

218. De Greef, L., et al. *Bilicam: using mobile phones to monitor newborn jaundice*. in *Proceedings of the 2014 ACM International Joint Conference on Pervasive and Ubiquitous Computing*. 2014. ACM.

219. Leung, T.S., et al., *Screening neonatal jaundice based on the sclera color of the eye using digital photography.* Biomedical optics express, 2015. **6**(11): p. 4529-4538.

220. Munkholm, S.B., et al., *The smartphone camera as a potential method for transcutaneous bilirubin measurement.* PloS one, 2018. **13**(6).

221. Swarna, S., et al., *The smart phone study: assessing the reliability and accuracy of neonatal jaundice measurement using smart phone application.* International Journal of Contemporary Pediatrics, 2018. **5**(2): p. 285-289.

222. Dumont, A.P., et al. *Development of mobile phone based transcutaneous billirubinometry*. 2017.

223. Taylor, J.A., et al., *Use of a smartphone app to assess neonatal jaundice.* Pediatrics, 2017: p. e20170312.

224. Olusanya, B.O., D.O. Imosemi, and A.A. Emokpae, *Differences between transcutaneous and serum bilirubin measurements in black African neonates.* Pediatrics, 2016: p. e20160907.

225. Chimhini, G.L.T., S. Chimhuya, and V. Chikwasha, *Evaluation of transcutaneous bilirubinometer (DRAEGER JM 103) use in Zimbabwean newborn babies.* Maternal health, neonatology and perinatology, 2018. **4**(1): p. 1.

226. Watchko, J.F. *Hyperbilirubinemia in African American neonates: clinical issues and current challenges*. in *Seminars in Fetal and Neonatal Medicine*. 2010. Elsevier.

227. Hemmati, F. and N.A.K. Rad, *The value of Bilicheck® as a screening tool for neonatal jaundice in the South of Iran.* Iranian journal of medical sciences, 2013. **38**(2): p. 122.

228. Jacques, S.L., D.G. Oelberg, and I. Saidi, *Method and apparatus for optical measurement of bilirubin in tissue*. 1994, Google Patents.

229. Sudha, G., et al., *Optical monitoring of bilirubin-simulation and experimental results.* Journal of Optics, 2007. **36**(2): p. 87-97.

230. van Erk, M.D., et al., *How skin anatomy influences transcutaneous bilirubin determinations: an in vitro evaluation.* Pediatric research, 2019. **86**(4): p. 471-477.

231. Alerstam, E., T. Svensson, and S. Andersson-Engels, *Parallel computing with graphics processing units for high-speed Monte Carlo simulation of photon migration.* Journal of biomedical optics, 2008. **13**(6): p. 060504.

232. Zhu, C., Q. Liu, and N. Ramanujam, *Effect of fiber optic probe geometry on depth-resolved fluorescence measurements from epithelial tissues: a Monte Carlo simulation.* Journal of Biomedical Optics, 2003. **8**(2): p. 237-248.

233. Zhu, C. and Q. Liu, *Numerical investigation of lens based setup for depth sensitive diffuse reflectance measurements in an epithelial cancer model.* Optics express, 2012. **20**(28): p. 29807-29822.

234. Bosschaart, N., et al., *Optical properties of neonatal skin measured in vivo as a function of age and skin pigmentation.* Journal of biomedical optics, 2011. **16**(9): p. 097003-097003-10.

235. Jacques, S. *Skin Optics*. 1998; Available from: http://omlc.org/news/jan98/skinoptics.html.

236. Mustafa, F.H., P.W. Jones, and A.L. McEwan, *Near infrared spectroscopy for body fat sensing in neonates: quantitative analysis by GAMOS simulations.* Biomedical engineering online, 2017. **16**(1): p. 14.

237. Randeberg, L.L., *Diagnostic applications of diffuse reflectance spectroscopy.* 2005.

238. Van Gemert, M., et al., *Skin optics.* IEEE Transactions on biomedical engineering, 1989. **36**(12): p. 1146-1154.

239. Toth, B., A. Becker, and B. Seelbach-Göbel, *Oxygen saturation in healthy newborn infants immediately after birth measured by pulse oximetry.* Archives of gynecology and obstetrics, 2002. **266**(2): p. 105-107.

240. Buonocore, G., R. Bracci, and M. Weindling, *Neonatology: a practical approach to neonatal diseases*. 2012: Springer Science & Business Media.

241. Salomatina, E.V., et al., *Optical properties of normal and cancerous human skin in the visible and near-infrared spectral range.* Journal of biomedical optics, 2006. **11**(6): p. 064026.

242. Sandell, J.L. and T.C. Zhu, *A review of in-vivo optical properties of human tissues and its impact on PDT.* Journal of biophotonics, 2011. **4**(11-12): p. 773-787.

243. Bhutani, V.K., L. Johnson, and E.M. Sivieri, *Predictive ability of a predischarge hour-specific serum bilirubin for subsequent significant hyperbilirubinemia in healthy term and near-term newborns.* Pediatrics, 1999. **103**(1): p. 6-14.

244. Maisels, M.J., et al., *Evaluation of a new transcutaneous bilirubinometer.* Pediatrics, 2004. **113**(6): p. 1628-1635.

245. de Bruin, D.M.M., et al., *Optical phantoms of varying geometry based on thin building blocks with controlled optical properties.* Journal of biomedical optics, 2010. **15**(2): p. 025001.

246. *Food Dyes and Beer's Law - What makes you drink blue?* 2019.

247. Saager, R.B., et al. *Multilayer silicone phantoms for the evaluation of quantitative optical techniques in skin imaging*. in *Design and Performance Validation of Phantoms Used in Conjunction with Optical Measurement of Tissue II*. 2010. International Society for Optics and Photonics.

248. Ayers, F., et al. *Fabrication and characterization of silicone-based tissue phantoms with tunable optical properties in the visible and near infrared domain*. in *Design and Performance Validation of Phantoms Used in Conjunction with Optical Measurements of Tissue*. 2008. International Society for Optics and Photonics.

249. Moffitt, T.P., Y.-C. Chen, and S.A. Prahl, *Preparation and characterization of polyurethane optical phantoms.* Journal of Biomedical Optics, 2006. **11**(4): p. 041103.

250. Prahl, S.A., M.J. van Gemert, and A.J. Welch, *Determining the optical properties of turbid media by using the adding–doubling method.* Applied optics, 1993. **32**(4): p. 559-568.

251. Prahl, S.A., *THE ADDING-DOUBLING METHOD.* Optical-Response of Laser-Irradiated Tissue, 1995: p. 101.

252. Prahl, S., *Everything I think you should know about Inverse Adding-Doubling.* Oregon Medical Laser Center, St. Vincent Hospital, 2011: p. 1-74.

253. Sumner, R., *Processing raw images in matlab.* Department of Electrical Engineering, University of California Sata Cruz, 2014.

254. Jacques, S.L., et al. *Developing an optical fiber reflectance spectrometer to monitor bilirubinemia in neonates*. in *Laser-Tissue Interaction VIII*. 1997. International Society for Optics and Photonics.

255. Mahajan, G., et al., *Transcutaneous bilirubinometer in assessment of neonatal jaundice in northern India.* Indian pediatr, 2005. **42**(1): p. 41-5.

256. Desroches, J., et al., *A new method using Raman spectroscopy for in vivo targeted brain cancer tissue biopsy.* Scientific reports, 2018. **8**(1): p. 1-10.

257. Mandair, G.S. and M.D. Morris, *Contributions of Raman spectroscopy to the understanding of bone strength.* BoneKEy reports, 2015. **4**.

258. Krasnikov, I., et al., *Two efficient approaches for modeling of Raman scattering in homogeneous turbid media.* JOSA A, 2016. **33**(3): p. 426-433.

259. Krasnikov, I., et al., *Monte Carlo simulation of the influence of internal optical absorption on the external Raman signal for biological samples.* JOSA A, 2019. **36**(5): p. 877-882.

260. Haifler, M., et al., *Discrimination of Malignant and Normal Kidney Tissue with Short Wave Infra-Red Dispersive Raman Spectroscopy.* Journal of biophotonics, 2018.

261. Pence, I. and A. Mahadevan-Jansen, *Clinical instrumentation and applications of Raman spectroscopy.* Chemical Society Reviews, 2016. **45**(7): p. 1958-1979.

262. Hibbard, T.N., *Some combinatorial properties of certain trees with applications to searching and sorting.* Journal of the ACM (JACM), 1962. **9**(1): p. 13-28.

263. Verleker, A.P., et al., *Optical dosimetry probes to validate Monte Carlo and empirical-method-based NIR dose planning in the brain.* Applied optics, 2016. **55**(34): p. 9875-9888.

264. Draghici, A.E., et al., *Near infrared spectroscopy for measuring changes in bone hemoglobin content after exercise in individuals with spinal cord injury.* Journal of Orthopaedic Research®, 2018. **36**(1): p. 183-191.

265. Cassano, P., et al., *Selective photobiomodulation for emotion regulation: model-based dosimetry study.* Neurophotonics, 2019. **6**(1): p. 015004.

266. Yuan, Y., et al., *Transcranial photobiomodulation with near-infrared light from childhood to elderliness: simulation of dosimetry.* Neurophotonics, 2020. **7**(1): p. 015009.

267. Bleeker, F.E., R.J. Molenaar, and S. Leenstra, *Recent advances in the molecular understanding of glioblastoma.* Journal of neuro-oncology, 2012. **108**(1): p. 11-27.

268. Walker, C., et al., *Biology, genetics and imaging of glial cell tumours.* The British journal of radiology, 2011. **84**(special_issue_2): p. S90-S106.

269. Davis, M.E., *Glioblastoma: overview of disease and treatment.* Clinical journal of oncology nursing, 2016. **20**(5): p. S2.

270. *World Cancer Report 2014*. World Health Organization.

271. Stupp, R., et al., *Radiotherapy plus concomitant and adjuvant temozolomide for glioblastoma.* New England journal of medicine, 2005. **352**(10): p. 987-996.

272. Young, R.M., et al., *Current trends in the surgical management and treatment of adult glioblastoma.* Annals of translational medicine, 2015. **3**(9).

273. Walker, M.D., T.A. Strike, and G.E. Sheline, *An analysis of dose-effect relationship in the radiotherapy of malignant gliomas.* International Journal of Radiation Oncology* Biology* Physics, 1979. **5**(10): p. 1725-1731.

274. Mirimanoff, R.-O., et al., *Radiotherapy and temozolomide for newly diagnosed glioblastoma: recursive partitioning analysis of the EORTC 26981/22981-NCIC CE3 phase III randomized trial.* Journal of Clinical Oncology, 2006. **24**(16): p. 2563-2569.

275. Carson, K.A., et al., *Prognostic factors for survival in adult patients with recurrent glioma enrolled onto the new approaches to brain tumor therapy CNS consortium phase I and II clinical trials.* Journal of Clinical Oncology, 2007. **25**(18): p. 2601-2606.

276. Sizoo, E.M., et al., *Symptoms and problems in the end-of-life phase of high-grade glioma patients.* Neuro-oncology, 2010. **12**(11): p. 1162-1166.

277. Lawson, H.C., et al., *Interstitial chemotherapy for malignant gliomas: the Johns Hopkins experience.* Journal of neuro-oncology, 2007. **83**(1): p. 61-70.

278. Torper, O. and M. Götz, *Brain repair from intrinsic cell sources: Turning reactive glia into neurons.* Progress in Brain Research, 2017.

279. Bianco, J., et al., *On glioblastoma and the search for a cure: where do we stand?* Cellular and Molecular Life Sciences, 2017: p. 1-16.

280. Gardeck, A.M., J. Sheehan, and W.C. Low, *Immune and Viral Therapies for Malignant Primary Brain Tumors.* Expert Opinion on Biological Therapy, 2017(just-accepted).

281. Mittal, S., et al., *Alternating electric tumor treating fields for treatment of glioblastoma: rationale, preclinical, and clinical studies.* Journal of Neurosurgery, 2017: p. 1-8.

282. Anson, D.M., et al., *The Effect of Luteolin on Human Glioblastoma.* 2016.

283. Sulman, E.P., M. Guerrero, and K. Aldape, *Transcription profiling of brain tumors: tumor biology and treatment stratification*, in *CNS Cancer*. 2009, Springer. p. 529-551.

284. Wang, L., et al., *What is the advance of extent of resection in glioblastoma surgical treatment—a systematic review.* Chinese Neurosurgical Journal, 2019. **5**(1): p. 2.

285. Sampson, J.H., et al., *Brain immunology and immunotherapy in brain tumours.* Nature Reviews Cancer, 2019: p. 1-14.

286. Zhan, T., et al. *CRISPR/Cas9 for cancer research and therapy*. in *Seminars in cancer biology*. 2019. Elsevier.

287. Kim, S.-S., et al., *Encapsulation of temozolomide in a tumor-targeting nanocomplex enhances anti-cancer efficacy and reduces toxicity in a mouse model of glioblastoma.* Cancer letters, 2015. **369**(1): p. 250-258.

288. Jhaveri, N., et al., *Noscapine inhibits tumor growth in TMZ-resistant gliomas.* Cancer letters, 2011. **312**(2): p. 245-252.

289. Caragher, S., A.J. Chalmers, and N. Gomez-Roman, *Glioblastoma's Next Top Model: novel culture systems for brain cancer radiotherapy research.* Cancers, 2019. **11**(1): p. 44.

290. Sanai, N. and M.S. Berger, *Glioma extent of resection and its impact on patient outcome.* Neurosurgery, 2008. **62**(4): p. 753-766.

291. Ferraro, N., et al., *The role of 5-aminolevulinic acid in brain tumor surgery: a systematic review.* Neurosurgical review, 2016. **39**(4): p. 545-555.

292. Schwake, M., et al., *Simultaneous fluorescein sodium and 5-ALA in fluorescence-guided glioma surgery.* Acta neurochirurgica, 2015. **157**(5): p. 877-879.

293. Barbagallo, G.M., et al., *5-ALA fluorescence-assisted surgery in pediatric brain tumors: report of three cases and review of the literature.* British journal of neurosurgery, 2014. **28**(6): p. 750-754.

294. Roessler, K., et al., *Intraoperative tissue fluorescence using 5-aminolevolinic acid (5-ALA) is more sensitive than contrast MRI or amino acid positron emission tomography (18F-FET PET) in glioblastoma surgery.* Neurological research, 2012. **34**(3): p. 314-317.

295. Potapov, A.A., et al., *First experience in 5-ALA fluorescence-guided and endoscopically assisted microsurgery of brain tumors.* Medical Laser application, 2008. **23**(4): p. 202-208.

296. Schebesch, K.-M., et al., *Sodium fluorescein–guided resection under the YELLOW 560 nm surgical microscope filter in malignant brain tumor surgery—a feasibility study.* Acta neurochirurgica, 2013. **155**(4): p. 693-699.

297. Okuda, T., H. Yoshioka, and A. Kato, *Fluorescence-guided surgery for glioblastoma multiforme using high-dose fluorescein sodium with excitation and barrier filters.* Journal of Clinical Neuroscience, 2012. **19**(12): p. 1719-1722.

298. Kuroiwa, T., Y. Kajimoto, and T. Ohta, *Development of a fluorescein operative microscope for use during malignant glioma surgery: a technical note and preliminary report.* Surgical neurology, 1998. **50**(1): p. 41-49.

299. Zhang, D.Y., S. Singhal, and J.Y. Lee, *Optical principles of fluorescence-guided brain tumor surgery: a practical primer for the neurosurgeon.* Neurosurgery, 2019. **85**(3): p. 312-324.

300. Stummer, W., et al., *Predicting the "usefulness" of 5-ALA-derived tumor fluorescence for fluorescence-guided resections in pediatric brain tumors: a European survey.* Acta neurochirurgica, 2014. **156**(12): p. 2315-2324.

301. Louis, D.N., et al., *The 2016 World Health Organization classification of tumors of the central nervous system: a summary.* Acta neuropathologica, 2016. **131**(6): p. 803-820.

302. Amunts, K., et al., *BigBrain: an ultrahigh-resolution 3D human brain model.* Science, 2013. **340**(6139): p. 1472-1475.

303. Rajkowska, G., L.D. Selemon, and P.S. Goldman-Rakic, *Neuronal and glial somal size in the prefrontal cortex: a postmortem morphometric study of schizophrenia and Huntington disease.* Archives of general psychiatry, 1998. **55**(3): p. 215-224.

304. Custo, A., et al., *Effective scattering coefficient of the cerebral spinal fluid in adult head models for diffuse optical imaging.* Applied optics, 2006. **45**(19): p. 4747-4755.

305. Zhou, Y., et al., *Optical biopsy identification and grading of gliomas using label-free visible resonance Raman spectroscopy.* Journal of biomedical optics, 2019. **24**(9): p. 095001.

306. Beljebbar, A., et al., *Ex vivo and in vivo diagnosis of C6 glioblastoma development by Raman spectroscopy coupled to a microprobe.* Analytical and bioanalytical chemistry, 2010. **398**(1): p. 477-487.

307. Kalkanis, S.N., et al., *Raman spectroscopy to distinguish grey matter, necrosis, and glioblastoma multiforme in frozen tissue sections.* Journal of neuro-oncology, 2014. **116**(3): p. 477-485.

308. Tanaka, T., M. Shnimizu, and H. Moriwaki, *Cancer chemoprevention by carotenoids.* Molecules, 2012. **17**(3): p. 3202-3242.

309. Moroni, F., *Tryptophan metabolism and brain function: focus on kynurenine and other indole metabolites.* European journal of pharmacology, 1999. **375**(1-3): p. 87-100.

310. Koljenović, S., et al., *Discriminating vital tumor from necrotic tissue in human glioblastoma tissue samples by Raman spectroscopy.* Laboratory Investigation, 2002. **82**(10): p. 1265-1277.

APPENDIX

INVERSE TRANSFORM SAMPLING FROM EXCITATION VOLUME TO DETERMINE EMISSION LAUNCH POSITION

The MC methodology requires that variables be randomly sampled from a well-defined probability distribution. This probability distribution is related to how MC accomplishes the task of photon simulations, for example, the distribution could be how far a photon propagates. In reality, the photon can propagate from 0 mm to ∞ mm, but the random variable is bound from 0 to 1 inclusive and uniformly chosen. The function for propagation distance might look like the following:

$$d_p = \mu_t e^{-\mu_t \Delta s} \quad (1)$$

Where $\mu_t = \mu_s + \mu_a$. A photon can propagate any positive distance, but the chances of a photon propagating a far distance are almost non-existent and the chance that the photon travels a much shorter distance is much more likely. Choosing a propagation length is one of the metrics that rely on sampling from a random uniform in the MC method. The first step is to integrate the propagation distribution so that the resultant function is monotonically increasing with increasing distance.

$$d_p(s) = \mu_t e^{-\mu_t \Delta s} \rightarrow \int_0^{\infty} \mu_t e^{-\mu_t \Delta s}\, ds \quad (2)$$

The propagation function is analytically integrable, and the result is:

$$\int_0^{\infty} \mu_t e^{-\mu_t \Delta s}\, ds = 1 - e^{-\mu_t \Delta s} \quad (3)$$

The second step is to set the right-hand side of this integrand to be ϵ, the uniform random integer, so that:

$$\epsilon = 1 - e^{-\mu_t \Delta s} \quad (4)$$

The final step is to solve for Δs, the propagation length:

$$\Delta s = -\frac{\ln(1-\epsilon)}{\mu_t} \quad (5)$$

So that the final result is a function that returns a propagation distance over its entire bound based on the entry of a random variable that is bound from 0 to 1.

In the case that a distribution is not continuous but rather discrete, the same treatment can still be applied. For example, say that a discrete distribution looks like the following:

$$P = [\,0.25\ 0.50\ 0.1\ 0.1\ 0.05]$$

Following the same steps as in the analytical method of inversely sampling distributions, the distribution is first cumulatively summed:

$$P_k = \sum_{i=1}^{k} x_i = [0.25\ 0.75\ 0.85\ 0.95\ 1] \quad (6)$$

This cumulative sum is then set to on the right-hand side to the value ϵ, so that:

$$\epsilon = [0.25\ 0.75\ 0.85\ 0.95\ 1]$$

The last step is to consider that the value of ϵ generated must then be equal to or lower than a particular term of this distribution. So, for example, if ϵ is 0.5, only the first term of the cumulative distribution is less than or equal to ϵ, so that the 1st index of the array is chosen. If ϵ is 0.97, then the fourth term of the distribution is the closest while being less than in the distribution, and is subsequently chosen. This inverse sampling of discrete distribution was used in conjunction with a rapid ‘left-side’ binary search

algorithm on the GPU side of MCX to perform fast calculations of photon launch positions using a 1-dimensional flattened excitation flux distribution.